

hp-Adaptive Simulation and Inversion of Magnetotelluric Measurements

Julen Alvarez-Aramberri

Supervised by
David Pardo and H el ene Barucq

Submitted to
University of Basque Country (UPV/EHU)
and
University of Pau (UPPA)

December 2015



A mis padres. Por todo.

A partir d'une ignoble souffrance, à nouveau, l'insolence qui, malgré tout, persiste de façon sournoise, grandit, d'abord lentement, puis, tout à coup, dans un éclat, elle m'aveugle et m'exalte dans un bonheur affirmé contre toute raison.

*Le bonheur à l'instant m'enivre, il me saoule.
Je le crie, je le chante à pleine gorge.
En mon cœur idiot, l'idiotie chante à gorge déployée.*

JE TRIOMPHE !

Henri Troppmann - Le bleu du ciel, George Bataille.

ACKNOWLEDGEMENTS

Si algo está claro es que el camino que me ha llevado a terminar este doctorado en matemáticas ha sido poco ortodoxo. Me licencié en físicas, estudié un máster en finanzas y he terminado dentro del mundo de las matemáticas. Tan extraña travesía me ha permitido conocer a mucha que gente no sólo ha enriquecido mi vida, sino que además me ha ayudado en muchos momentos para que este doctorado salga adelante. El proceso de doctorarse es en ocasiones duro, y en ciertos momentos resulta más gratificante una simple charla que solucionar un error en el código. En esta sección dedicada a ello, me gustaría agradecer su compañía, apoyo y ayuda de diferentes tipos a toda la gente que considero se lo merece. No obstante, como dicta la tan manida frase cuyo original significado me hace gracia aplicar aquí, ni son todos los que están, ni están todos los que son.

En primer lugar, quiero dar las gracias a mis dos directores. As exaggerated as it may sound, I am convinced that this PhD dissertation would have never been completed if not for David. At the personal level, I have greatly enjoyed the conversations we maintained throughout these years, which, I would say, have substantially enriched both of us. At a professional level, I could go on and enumerate all your virtues as a supervisor, but I would summarize them by saying that I cannot conceive the possibility of a better supervisor. I only hope you do not change over time, so that future students can be as fortunate as I have been.

Ce travail n'aurait jamais été possible sans Hélène. C'est grâce à elle que j'ai pu accéder à une bourse en cotutelle entre l'Université de Pau et l'Universidad del País Vasco et, par conséquent, à mon doctorat. Je veux aussi la remercier pour la patience qu'elle a eue avec moi malgré mes nombreuses erreurs administratives, seulement comparable à la patience dont elle a fait preuve en m'aidant et en faisant toutes les corrections pertinentes du document ici présenté. Je ne veux pas oublier de la remercier aussi pour son excellente attention et ses impeccables manières. Quand on est toujours reçus par un grand sourire sincère, tout le reste devient beaucoup plus simple.

Academically, I would like to thank to my coautors, from whom I mainly learnt the skills to develop professional research; in particular to Professor Maciej Paszynski for different reasons. Also to my research group mates for their support. En particular a Vincent, por su inestimable ayuda con las correcciones del francés.

Son varias las instituciones que con su dinero han hecho posible el desarrollo de esta tesis doctoral, y a las que por lo tanto me gustaría reconocer aquí. A la Universidad del País Vasco (UPV/EHU) por la beca PIFG05/2011, al extinto Ministerio de Ciencia e Innovación bajo el proyecto MTM2010-16511, al Ministerio de Economía y Competitividad por el proyecto con referencia MTM2013-40824-P, al Gobierno Vasco bajo el Consolidated Research Group on "Mathematical Modeling, Simulation, and Industrial Applications

(M^2SI)” con referencia IT649-13 y a través del programa BERC 2014-2017, al Basque Center for Applied Mathematics bajo la acreditación “Severo Ochoa” de excelencia SEV-2013-0323, y al proyecto 712RT0449 de CYTED 2011.

Mi iniciación en el mundo de la investigación comienza con el máster en finanzas. Allí coincidí con varios compañeros que empezábamos como estudiantes de postgrado. Algunos se convirtieron en grandes amigos que me han acompañado durante estos años del doctorado compartiendo mil y una aventuras, momentos y conversaciones. Gracias por todas las historias vividas juntos. Estoy seguro que seguiremos *legendarieando* en el futuro.

Físicamente he realizado estancias de trabajo en tres sitios diferentes durante estos años. Así, quiero acordarme de mis compañeros de BCAM y de los buenos y malos momentos que vivimos juntos; de mis compañeros de Leioa, con los que a pesar de sus iniciales reticencias a aceptarme (quizás por no ser en origen matemático) terminé compartiendo decenas de comidas y cafés (todavía confío en que algún día veáis la luz, os entreguéis a los brazos de Hostelería y empecéis a ir a la cafetería correcta); et de mes collègues de Magique3D à Pau. Je dois reconnaître que j’ai eu du mal à apprécier la ville mais aussi que, grâce à vous, ce fut presque difficile de partir lors de mon dernier séjour.

Además quiero agradecer a mis amigos de Haro. Sospecho que la mayoría de ellos sigue sin tener muy claro qué es lo que hago en Bilbao. Sin embargo, siempre me han animado y mostrado su apoyo. Puede que debido a la errónea concepción que la sociedad tiene de un doctorado, también me han instado durante estos años a que *me pusiera a trabajar de una vez*. No desesperéis.

Cuando no vives en tu ciudad natal tus compañeros de piso terminan convirtiéndose en el sustituto de la familia. Con la que discutir, pero además pasar buenos ratos. He tenido la suerte de compartir piso con muchos de mis mejores amigos, los cuales han sido un gran apoyo durante los momentos más duros del doctorado. Mis compañeros de piso de la carrera a los que adeudo buena parte de mis notas, mis amigos del Erasmus con los que compartí un año inimaginable de vida; *La Squadra*. En particular, he tenido la grandísima suerte de vivir todos mis años de doctorado en la *Jamel House*. Le doy las gracias a *ella* por todos los inolvidables momentos vividos. Gracias eternas a todos mis compañeros de piso, pasados y actuales. Buena parte de mi felicidad es culpa vuestra. Sabéis que siempre podréis contar conmigo y mi albornoz.

No me gustaría olvidarme de las personas que no entran en ninguno de los párrafos anteriores y que también habéis estado de alguna manera, temporal o continuamente a mi lado estos años; sabéis quiénes sois.

Y mejor lo sabéis aquéllos amigos más cercanos que estando o no estando en alguno de los párrafos anteriores sois los pilares sobre los que se asienta mi vida. Que así siga.

Por último, dar las gracias a toda mi familia, de la que siempre he recibido mucho más cariño del que yo he dado. Es especial a mi hermana, quién siempre ha merecido un hermano mucho mejor del que yo soy, a mi abuela, quién hace los mejores pimientos rellenos de merluza del mundo, y a mi prima Sara, por lo fuerte que es y por lo todavía más fuerte que va a ser. Esta tesis también quiero dedicársela a ellas.

Y sobre todos los demás, mi padre y mi madre, las dos personas más importantes de mi vida. Entre otras muchas cosas, siempre me ha sorprendido vuestra capacidad de apoyarme en todo lo que he hecho. Lo entenderais o no, tuviera razón o no la tuviera. Recuerdo siendo muy pequeño preguntar qué es lo que queráis que fuera de mayor, y recuerdo que la respuesta siempre era la misma: buena persona. Si acaso he conseguido serlo, ha sido mérito vuestro. Mérito que del mismo modo os corresponde en este doctorado. Sabed también que no hay forma de que hubieseis sido mejores padres. Ninguna.

En definitiva, GRACIAS A TODOS.



ABSTRACT

The magnetotelluric (MT) method is a passive exploration technique that aims at estimating the resistivity distribution of the Earth's subsurface, and therefore at providing an *image* of it. This process is divided into two different steps. The first one consists in recording the data. In a second step, recorded measurements are analyzed by employing numerical methods. This dissertation focuses in this second task. We provide a rigorous mathematical setting in the context of the Finite Element Method (FEM) that helps to understand the MT problem and its inversion process. In order to recover a map of the subsurface based on 2D MT measurements, we employ for the first time in MTs a multi-goal oriented self adaptive *hp*-Finite Element Method (FEM). We accurately solve both the full formulation as well as a secondary field formulation where the primary field is given by the solution of a 1D layered media. To truncate the computational domain, we design a Perfectly Matched Layer (PML) that automatically adapts to high-contrast material properties that appear within the subsurface and on the air-ground interface. For the inversion process, we develop a first step of a Dimensionally Adaptive Method (DAM) by considering the dimension of the problem as a variable in the inversion. Additionally, this dissertation supplies a rigorous numerical analysis for the forward and inverse problems. Regarding the forward modelization, we perform a frequency sensitivity analysis, we study the effect of the source, the convergence of the *hp*-adaptivity, or the effect of the PML in the computation of the electromagnetic fields and impedance. As far as the inversion is concerned, we study the impact of the selected variable for the inversion process, the different information that each mode provides, and the gains of the DAM approach.

ACCOMPLISHMENTS OF THE DISSERTATION

The main research accomplishments of the dissertation are:

- To develop a software that fully solves the 2D MT problem employing the self-adaptive *hp*-FEM for the first time.
- To implement and employ the multi-goal oriented adaptivity to obtain accurate results at different receivers at the same time.
- To design a PML that automatically adjusts its parameters, which is specially useful for inversion.
- To accurately solve the forward MT problem.
- To implement both the forward full formulation and a secondary field formulation where the primary field is given by the solution of a 1D layered media.
- To provide a first step towards considering the dimension of the problem as a variable in the inversion.
- To bring a rigorous mathematical setting in the context of FEM that helps to understand the MT problem and its inversion.
- To supply a rigorous numerical analysis. In particular, the following aspects have been considered:
 - The effect of the source.
 - A frequency sensitivity analysis.
 - The convergence of the *hp*-adaptive algorithm.
 - The impact of the selected variable for the inversion process.
 - The different information that each mode provides.
 - The effect of the PML in the computation of the EM fields and impedance.

Additionally, the following articles and presentations have been given by Mr. Julen Alvarez-Aramberri during the development of his Ph.D. Dissertation.

JOURNALS (PEER-REVIEWED):

1. 2015: **J. Alvarez-Aramberri**, D. Pardo and H. Barucq. *A Secondary Field Based hp-Finite Element Method for the Simulation of Magnetotelluric Measurements*. In press in Journal of Computational Science (2015). <http://dx.doi.org/10.1016/j.jocs.2015.02.005>.
2. 2015: M. Smolka, R. Schaeffer, M. Paszynski, D. Pardo, **J. Alvarez-Aramberri**. *Agent-Oriented Hierarchic Strategy for Solving Inverse Problems* Accepted in International Journal of Applied Mathematics and Computer Science.
3. 2015: D. Pardo, **J. Alvarez-Aramberri**, M. Paszynski, L. Dalcin and V.M. Calo. *Impact of Element-Level Static Condensation on Iterative-Solver Performance*. Computers & Mathematics with Applications, Vol. 70, 2331–2341. International Journal of Applied Mathematics and Computer Science, 2015, Vol. 25, No. 3, 483–498.
4. 2012: D.Pardo, M.Paszynski, N. Collier, **J. Alvarez** and V.M. Calo. *A survey on direct solvers for Galerkin methods*. SEMA Journal n57, 107-134.

PROCEEDINGS:

5. 2015: **J. Alvarez-Aramberri**, S.A. Bakr, D. Pardo and H. Barucq. *Quantities of Interest for Surface based Resistivity Geophysical Measurements*. Procedia Computer Science, Vol. 51, 964-973.
6. 2015: E. Gajda-Zagorska, M. Smolka, R. Schaefer, D. Pardo, and **J. Alvarez-Aramberri**. *Multi-objective Hierarchic Memetic Solver for Inverse Parametric Problems*. Procedia Computer Science, Vol. 51, 974-983
7. 2014: **J. Alvarez-Aramberri**, D. Pardo and H. Barucq. *Automatically Adapted Perfectly Matched Layers for Problems with High Contrast Materials Properties*. Procedia Computer Science, Vol. 29, 970-979.
8. 2013: **J. Alvarez-Aramberri**, D. Pardo and H. Barucq. *Inversion of Magnetotelluric Measurements using Multigoal Oriented hp-Adaptivity*. Procedia Computer Science, Vol. 18, 1565-1573.
9. 2012: **J. Alvarez-Aramberri**, D. Pardo, M. Paszynski, N. Collier, L. Dalcin and V. M. Calo. *On round-off Error for Adaptive Finite Element Methods*. Procedia Computer Science Vol. 9, 1474-1483.

CONFERENCE TALKS:

1. 2015: **J. Alvarez-Aramberri**, S.A. Bakr, D. Pardo, H. Barucq and E. Alberdi. *Quantities of Interest for Surface based Resistivity Geophysical Measurements*. Int. Conference on Computational Science (ICCS 2015), Reykjavík, Iceland.

2. 2015: **J. Alvarez-Aramberri**, D. Pardo and H. Barucq. *Dimensionally Adaptive Simulation and Inversion of Magnetotelluric Measurements*. PANACM 2015, Buenos Aires, Argentina.
3. 2014: **J. Alvarez-Aramberri**, D. Pardo and H. Barucq and E. Alberdi. *Automatically Adapted Perfectly Matched Layers for Problems with High Contrast Materials Properties* Int. Conference on Computational Science (ICCS 2014), Cairns, Australia.
4. 2014: **J. Alvarez-Aramberri**, D. Pardo H. Barucq. *Multidimensional Algorithm for the Inversion of Magnetotelluric Measurements*. 5th European Conference on Computational Mechanics (ECCM V), Barcelona, Spain.
5. 2013: **J. Alvarez-Aramberri**, D. Pardo and H. Barucq. *Inversion of Magnetotelluric Measurements using Multigoal Oriented hp-Adaptivity*. Int. Conference on Computational Science (ICCS 2013), Barcelona, Spain.
6. 2012: **J. Alvarez-Aramberri**, D. Pardo, M. Paszynski, N. Collier, L. Dalcin and V. M. Calo. *On round-off Error for Adaptive Finite Element Methods*. Int. Conference on Computational Science (ICCS 2012), Omaha, USA.

SEMINARS & INVITED TALKS:

7. 2015: **J. Alvarez-Aramberri**, D. Pardo and H. Barucq. *Secondary Field Formulation for the Inversion of the Magnetotelluric Problem* Workshop on Advanced Subsurface Visualization Methods: "Exploring the Earth" 2015, Pau, France.
8. 2014: **J. Alvarez-Aramberri**, D. Pardo and H. Barucq. *Dimensionally Adaptive Inversion of the Magnetotelluric Problem* BCAM Workshop on Computational Mathematics, BCAM, Bilbao, Jul 2014.
9. 2014: D. Pardo, **J. Alvarez-Aramberri**, V. Darrigrand, S. Bakr, and C. Torres-Verdin. *Fast Inversion of Alternate Current (AC) Geophysical Measurements* Third International Workshop On Multiphysics, Multiscale, and Optimization Problems, BCAM, Bilbao, May 2014.
10. 2014: **J. Alvarez-Aramberri**, D. Pardo and H. Barucq. *Automatically Adapted PML for Problems with High Contrast Materials Properties*. Third International Workshop On Multiphysics, Multiscale, and Optimization Problems, BCAM, Bilbao, May 2014.
11. 2014: **J. Alvarez-Aramberri**, D. Pardo and H. Barucq. *Adaptive FEMs with Electromagnetic Applications*. University of Basque Country, Bilbao, Feb 2014.
12. 2014: **J. Alvarez-Aramberri**, D. Pardo and H. Barucq. *Description of a Forward Magnetotelluric Problem*. AGH University of Science and Technology, Krakow, Jan 2014.

CONTENTS

List of Figures	xxvii
List of Tables	xxix
List of Acronyms	xxxix
List of Frequently Used Symbols	xxxiii
Resumen	xxxvii
Résumé	xliii
INTRODUCTION	1
1 DESCRIPTION OF THE MAGNETOTELLURIC METHOD	5
1.1 EM Properties of Earth Materials	7
1.2 Governing Equations: Maxwell's Equations	8
1.3 Magnetotelluric Characterization	11
1.3.1 The MT Transfer Functions	11
1.3.2 Homogeneous Half Space: Skin Depth	11
1.3.3 1D Survey as a Layered Media: Apparent Resistivity	13
1.3.4 2D Survey-Along Strike Approach	15
1.3.5 3D Survey	17
1.4 Summary of MT Assumptions	17
2 VARIATIONAL FORMULATION OF THE FORWARD PROBLEM	19
2.1 3D Formulation	20
2.2 2D Formulation	21
2.3 1D Formulation	21
2.4 Truncation of the domain	22
2.4.1 Perfectly Matched Layers	22
2.4.2 PML Definition	23
2.4.3 Variational Formulation in an Arbitrary System of Coordinates	24
2.4.4 Automatic Adjustment of PML Parameters	29
2.5 Secondary Field Formulation	30
2.5.1 3D Model	30
2.5.2 2D Model	31
2.6 Abstract Formulation	32
3 SOLUTION OF THE FORWARD PROBLEM	35
3.1 Solution for a 1D Layered Media	36
3.2 Solution to the 2D Problem: <i>hp</i> -FEM	38
3.2.1 Discretization of the Variational Problem	39
3.2.2 Master Element and Basis Functions	40
3.3 Mesh Construction	42
3.3.1 Goal-Oriented Adaptivity	43

3.3.2	Extension to the Multigoal-Oriented Adaptivity	47
3.3.3	Automatic <i>hp</i> -Adaptivity in 2D	48
4	FORMULATION AND NUMERICAL METHOD FOR THE SOLUTION OF THE INVERSE PROBLEM	51
4.1	Formulation of the Inverse Problem	51
4.2	Selecting the Quantity of Interest	54
4.3	Numerical Method in MT	55
4.3.1	Fundamentals of Gradient Based Methods	55
4.3.2	Computation of the Jacobian and Hessian	56
4.3.3	Solution Methods	61
4.4	New Approach: Dimensionally Adaptive Inversion	63
5	IMPLEMENTATION DETAILS	65
5.1	Structure and Main Features	65
5.2	Implementation of the Forward Direct and Adjoint Problems:	69
5.3	Implementation of the Inverse Solver	71
5.3.1	Computation of the Jacobian	71
5.3.2	Inversion Algorithms	74
5.3.3	Implementation of the L-BFGS-U	74
6	NUMERICAL RESULTS	79
6.1	General Considerations of our Model Problems	79
6.2	Verification	80
6.2.1	Forward Problem	82
6.2.2	Inverse Problem	84
6.3	Numerical Analysis	85
6.3.1	Forward Problem	85
6.3.2	Inverse Problem	91
6.4	Geophysical Results	96
6.4.1	Frequency Analysis	97
6.4.2	Study of the Quantity of Interest	97
6.4.3	TE vs TM Modes.	99
6.4.4	Separation of 1D and 2D Effects	99
7	CONCLUSIONS AND FUTURE WORK	103
8	APPENDIX	105
8.1	Appendix: Uncoupling Maxwell's Equations in Anysotropic Media	105
8.2	Variational Formulation in the Complex Plane	107

LIST OF FIGURES

1.1	Homogeneous half-space model for the Earth's formation.	12
1.2	1D layered Earth's formation.	13
1.3	Illustration of the apparent resistivity.	14
1.4	Simple 2D conductivity model in which the conductivity is constant along the y direction. Redrawn from Simpson and Bahr [130].	15
2.1	Illustration of the computational subdomains Ω_P and Ω_S and the material properties inside each subdomain. Left: x - z section. Right: y - z section.	31
2.2	Illustration of the computational subdomains Ω_P and Ω_S and the material properties inside each subdomain. σ only depends on z in Ω_P , and on x and z in Ω_S	31
3.1	Incident plane wave impinging perpendicularly to a three horizontal layered domain.	37
3.2	Incident plane wave impinging perpendicularly to a N horizontal layered medium.	38
3.3	Construction of a vertex node basis function (from [35]).	41
3.4	Nodes in a quadrilateral master element (from [35]).	41
5.1	Structure of the implemented software.	66
5.2	Illustration of different h -refinements.	68
6.1	Considered Model problems.	81
6.2	Relative error between the numerical and analytical solutions for impedance for different horizontal sizes of the source.	82
6.3	FEM mesh in an arbitrary direction within the PML region.	83
6.4	Relative error between the apparent resistivity obtained with the exact and numerical solutions for different subsurface formations against frequency for the TE and TM modes.	83
6.5	Relative errors between the results obtained with the full field formulation vs. those obtained with the secondary field formulation.	84
6.6	Relative error in E_y (TE mode) and H_y (TM mode) vs. the number of dof for three type of refinements: uniform h -refinements, uniform p -refinements and multi-goal oriented self-adaptive hp -refinements.	86
6.7	Relative error in the impedance vs. the number of dof. for three type of refinements: uniform h -refinements, uniform p -refinements and multi-goal oriented self-adaptive hp -refinements.	86
6.8	Different hp -grids after performing the adaptive algorithm for the TE and TM formulations with a frequency equal to 0.1 Hz.	88
6.9	Different hp -grids during execution of the multi-goal oriented adaptive algorithm for the TE mode when the secondary field formulation is employed at 0.1Hz.	89
6.10	Relative error for the apparent resistivity computed with the full and secondary field formulations.	90

List of Figures

6.11	$\log(E_y)$ for the TE and $\log(H_y)$ for the TM mode when the secondary field formulation is employed.	90
6.12	Logarithm of the module of the solution of the adjoint problem corresponding to the receiver located at $x = -20$ km for the TE and TM modes, when the secondary field formulation is employed.	91
6.13	$\log(E_y)$ corresponding to a 5 km thick PML and $\alpha = 10^{-5}$. The black line indicates the region where the PML starts.	92
6.14	Cost functional against the iteration number for Model 1 in Table 6.1.	93
6.15	Cost functional against the iteration number for Model 2 in Table 6.1.	93
6.16	Cost functional against the iteration number when different modes are employed in the inversion.	95
6.17	Cost functional against the iteration number for the traditional and DAM inverse problems for Model 2 in Table 6.1.	97
6.18	Relative difference in the simulated measurements at the center of the domain produced by the presence of a 2D inhomogeneity for different frequencies for the models in Table 6.1.	98
6.19	Relative error for different QoI: $Q_E^E(\rho)$ and $Q_Z^E(\rho)$ correspond to the total electric field and the impedance computed with the full field formulation, respectively, while $Q_E^S(\rho)$ and $Q_Z^S(\rho)$ are the equivalent quantities computed with the secondary field formulation.	100
6.20	Relative difference between the impedance at the center of the domain and at $x = 100$ km at different frequencies for the Model 1 in Table 6.1.	101
6.21	Relative difference between the impedance at the center of the domain and at $x = 100$ km at different frequencies for the Model 1 in Table 6.1.	101
6.22	Apparent resistivity at different distances for the different subsurface formations. . .	102

LIST OF TABLES

5.1 Resource consumption of different solvers in 3D. N is the problem size, b is the (average) bandwidth of the matrix, M is the number of right-hand sides, s is a constant that depends upon the structure of the matrix, and can be as large as N , n is the size of the preconditioner, and c is a constant that depends upon the condition number of the matrix and the choice of preconditioner.	78
6.1 Different models for the formation of the subsurface given by Figure 6.1.	81
6.2 Different models for the formation of the subsurface given by Figure 6.1b.	88
6.3 Values of the resistivities during the inversion process.	88
6.4 Initial point and solution for the considered inverse problems.	93
6.5 Values of the resistivities for the solution of the inversion problem.	95
6.6 Information of the two scenarios considered to compare the traditional and the DAM approaches for the inversion.	100

ACRONYMS

AS	Active Set
1D	One-Dimensional
2D	Two-Dimensional
3D	Three-Dimensional
BC	Boundary Conditions
BFGS	Broyden, Fletcher, Goldfarb, and Shanno
CG	Conjugate Gradient
COP	Constrained Optimization Problem
DAM	Dimensionally Adaptive Method
dof	Degrees of Freedom
DPG	Discontinuous Petrov-Galerkin
EM	Electromagnetic
FD	Finite Differences
FEM	Finite Element Methods
GN	Gauss-Newton
GP	Gradient Projection
IE	Integral Equations
IGA	IsoGeometric Analysis
IP	Inverse Problem
KKT	Karush-Kuhn-Tucker
MT	Magnetotelluric
NLCCG	Nonlinear Conjugate Gradient
PML	Perfectly Matched Layers
QoI	Quantity of Interest
RRI	Rapid Relaxation Inversion
TE	Transverse Electric
TM	Transverse Magnetic

LIST OF FREQUENTLY USED SYMBOLS

α	Decay factor in the PML
\mathcal{B}	Magnetic induction
b	Sesquilinear form
C	Schmucker and Weidelt transfer function
$C(m)$	Cost functional
$\hat{\chi}$	Shape function
d	Data or measurements
\mathcal{D}	Electric displacement
δ	Skin depth
$e(x)$	Basis function
\mathcal{E}	Electric field in time domain
$E = (E_x, E_y, E_z)$	Electric field in frequency domain
ϵ	Electrical permittivity
ϵ_0	Electrical permittivity of the vacuum
ϵ_r	Relative electrical permittivity
F	Scalar test functions
\mathbf{F}	Vectorial test functions
g	Forward (nonlinear) operator
G	Forcing term
Γ	Boundary of the computational domain
j	Electric current density
j	Imaginary unit
\mathcal{J}	Jacobian
\mathcal{J}	Total current
\mathcal{J}^{imp}	Impressed current source in time domain

List of Frequently Used Symbols

$\mathbf{J}^{imp} = (J_x^{imp}, J_y^{imp}, J_z^{imp})$	Impressed current source in frequency domain
J_s	Surface impressed current source
h	Element size
\mathcal{H}	Magnetic field in time domain
$\mathbf{H} = (H_x, H_y, H_z)$	Magnetic field in frequency domain
\mathcal{H}	Hessian
L	Linear quantity of interest
λ	Regularization parameter
K	Physical element
\hat{K}	Master element
m	Model parameters
\mathcal{M}^{imp}	Magnetic current source in time domain
$\mathbf{M}^{imp} = (M_x^{imp}, M_y^{imp}, M_z^{imp})$	Magnetic current source in frequency domain
M_s	Surface magnetic current source
μ	Magnetic permeability
μ_0	Magnetic permeability of the vacuum
μ_r	Relative magnetic permeability
$\hat{\mathbf{n}}$	Unit (outward) vector normal to the surface
N_ω	Total number of frequencies in the inverse problem
N_{rec}	Total number of receivers
ω	Angular frequency
Ω	Computational domain
Ω_P	Comp. domain for the primary field problem
Ω_R	Comp. domain occupied by the receiver
Ω_S	Comp. domain occupied by the secondary field problem

p	Polynomial order of the element
ϕ	Phase tensor of the impedance
$\hat{\phi}$	Shape function
$R(m)$	Regularization term
R, T	Fresnel reflection and transmission coefficients
ρ	Resistivity
ρ^{app}	Apparent resistivity
ρ_f	Electric charge density
ρ_s	Surface-charge density
σ	Conductivity
t	Time
$\mathcal{T} = (\mathcal{T}_x, \mathcal{T}_y)$	Induction arrow
θ	Associated weight to each measurement
Y	Function to be determined in the PML
$\mathbf{x} = (x, y, z)$	Cartesian coordinates
$\boldsymbol{\zeta} = (\zeta_1, \zeta_2, \zeta_3)$	Coordinates in an arbitrary system of reference
\mathcal{Z}	Impedance tensor

RESUMEN

El método magnetotelúrico (MT) es una técnica de exploración de la corteza terrestre basada en mediciones electromagnéticas (EM). Existe en la ionosfera una fuente natural (no artificial) armónica en el tiempo [164] responsable de la generación de un campo EM que viaja en forma de onda plana hacia la superficie de la Tierra. Este proceso físico está gobernado por las ecuaciones de Maxwell y dependiendo de la frecuencia de la fuente y la conductividad del subsuelo, la onda plana incidente penetra en la corteza terrestre una distancia que oscila entre decenas de metros y cientos de kilómetros. Una serie de receptores colocados en la superficie de la Tierra se encargan de registrar las mediciones de los campos EM. Estas mediciones son ulteriormente posprocesadas (invertidas) utilizando métodos numéricos con el fin de obtener una *imagen* del subsuelo de la Tierra.

La base teórica del método fue establecida en la década de los años 50 por Tikhonov [150] y Cagniard [25]. Al tratarse de un método relativamente barato en lo económico, al no ser invasivo y debido a su nulo impacto ambiental, la industria lo ha considerado particularmente interesante. Desde su concepción, a lo largo de los años el método MT avanzó rápidamente dentro del campo de la Geofísica, en la exploración con fines industriales, y en el propio desarrollo de la instrumentación, factor también determinante a la hora de conseguir un buen funcionamiento del mismo. Además de centrarse en mejorar el método MT en sí, la investigación se ha concentrado en diversos ámbitos, tales como la investigación de la corteza profunda por medio de utilización de bajas frecuencias, la predicción de terremotos [60, 72] o el almacenamiento geológico de CO₂ [101]. Este procedimiento se ha aplicado a nivel industrial en la exploración de territorios para la búsqueda de hidrocarburos (petróleo y gas), en la exploración minera, en la explotación geotérmica, además de en el monitoreo de hidrocarburos y de aguas subterráneas [72]. Podemos encontrar los fundamentos y detalles físicos más concretos por ejemplo en los libros de Simpson y Bahr [130] y Chave y Jones [27].

Los códigos de modelización e inversión de medidas MT han evolucionado desde sus inicios donde se asumían modelos terrestres unidimensionales (1D), hasta los tridimensionales (3D), si bien estos últimos se encuentran actualmente dando sus primeros pasos. Entre todos los posibles métodos numéricos susceptibles de simular correctamente mediciones MT, en esta tesis nos centramos en los métodos de alto orden. Estos métodos, que han probado ser enormemente precisos, han sido vastamente empleados en los últimos

años en la comunidad de matemáticas aplicadas en una gran variedad de escenarios. Por ejemplo, su uso ha aumentado recientemente de manera drástica tanto en el ámbito de la mecánica computacional como en diversas aplicaciones de la ingeniería. En particular, el análisis isogeométrico (IGA) [58, 127] ha experimentado de unos años a esta parte una gran explosión, tanto académicamente como en su amplia aplicación en la industria de la ingeniería. Algo más reciente es el método discontinuo Petrov-Galerkin (DPG), inicialmente propuesto por Demkowicz y Gopalakrishnan [40, 171], y algo anterior el método auto-adaptativo de **Elementos Finitos hp** (hp -MEF) [37, 50, 146] (donde h representa el tamaño del elemento y p el orden de aproximación polinomial asociado a cada elemento).

Nosotros empleamos el hp -MEF basándonos en una extensión del trabajo de Demkowicz et al. [37]. De este modo, hemos desarrollado un software que resuelve por primera vez el problema MT empleando el método auto-adaptativo hp -MEF. Este método admite tanto refinamientos locales h como p en todo los elementos, lo cual representa una significativa ventaja, ya que la combinación de ambos tipos de refinamientos permite capturar mejor la presencia de singularidades, proporcionando así errores de discretización bajos. Es, por lo tanto, un método de alta precisión que proporciona convergencia exponencial incluso cuando estas singularidades están presentes [52, 7], una situación típica que se repite en MT. Debido a algunos desafíos en la implementación aún no resueltos [42] y a la elevada complejidad técnica que la implementación 3D del MEF- hp conlleva, en esta tesis nos limitamos exclusivamente al desarrollo de un software para los problemas MT 1D y 2D.

En MT es necesario obtener resultados precisos sólo en los receptores. Por lo tanto, la adaptatividad orientada a un objetivo (propuesta por primera vez por Becker y Rannacher a mediados de los 90 [12]) deviene en una elección natural a la hora de construir la malla de elementos finitos. Así, definimos una tolerancia para el error en una magnitud física preseleccionada con interés ingenieril. En nuestro caso, esta cantidad es una componente de los campos EM. Sin embargo, dado que la impedancia se define como una constante multiplicada por el cociente entre el campo eléctrico y su derivada, garantizando una buena solución para los campos EM también lo estaremos haciendo para la impedancia, y por ende, para la resistividad aparente. El objetivo de las estrategias adaptativas orientadas a objetivos tradicionales es construir una malla óptima en el sentido de minimizar el tamaño del problema necesario para lograr un error dado. Puesto que es necesario obtener resultados precisos en múltiples receptores, aquí implementamos, por primera vez en el contexto de MT, un algoritmo auto-adaptativo y multi-objetivo originalmente propuesto por Pardo en [105]. Una de las principales ventajas de este enfoque es que somos capaces de medir el error en una norma geofísicamente significativa.

En esta tesis discernimos entre la solución del campo primario y la del campo secundario. Las variaciones en el campo secundario fluctúan menos (gradientes más pequeños) que en el campo total, y por lo tanto el problema puede ser discretizado con mallas

más gruesas. En consecuencia, los campos secundarios son, en general, no sólo más fáciles de determinar, sino que además resultan también computacionalmente más baratos. Además, reemplazamos el habitualmente empleado campo primario 0D [161, 73, 123] por un campo primario 1D que se corresponde con una formación de la Tierra de capas horizontales. Este escenario es más realista en general, lo que produce resultados más precisos.

Para ambas formulaciones, la del campo total y la del campo secundario, el dominio computacional se trunca mediante un material absorbente (**Perfectly Matched Layer, (PML)**) [17], el cual diseñamos de forma eficiente para que se **adapte automáticamente a las propiedades físicas de los materiales**. En particular, se ajusta eficazmente en la interfaz aire-tierra, donde el contraste entre la conductividad de los materiales es de hasta dieciséis órdenes de magnitud.

El problema inverso MT se define como un problema de optimización no lineal. Los métodos para resolver este tipo problemas de optimización se pueden clasificar en deterministas y no deterministas. La convergencia dentro de estos últimos, es decir, dentro de los métodos de optimización globales (por ejemplo, los algoritmos genéticos, evolutivos o búsqueda de Monte-Carlo) por lo general requiere de un número elevado de iteraciones, siendo además necesario resolver uno o varios problemas directos en cada una de estas iteraciones. Resolver un problema MT directo de forma eficiente precisa de dominios computacionales grandes para una correcta modelización de la fuente, y es además habitualmente costoso en términos de tiempo de máquina. Debido a este elevado coste, los métodos deterministas han sido históricamente preferidos dentro de la comunidad MT, en concreto los métodos basados en el gradiente, los cuales suelen necesitar un menor número de iteraciones (y por ende soluciones del problema directo) para converger. Como contrapartida, estos métodos emplean derivadas de primer orden para el cálculo de la matriz Jacobiana (e incluso de segundo orden para la Hessiana de ser necesaria). La obtención de estas derivadas puede ser lenta y complicada, por lo que resulta imprescindible una implementación eficiente. El otro inconveniente principal de los métodos basados en el gradiente consiste en que convergen a mínimos que pueden resultar locales.

En nuestro trabajo empleamos el método L-BFGS-U (Broyden, Fletcher, Goldfarb y Shanno) [170]. Se trata de un método basado en el gradiente especialmente indicado para problemas con acotaciones simples, por lo que se adecúa a nuestro caso, donde solamente delimitamos los valores de la resistividad por una constante para asegurarnos de que tenga significado físico. Al tratarse de un método cuasi-Newton, no es necesario calcular la matriz Hessiana explícitamente, ya que la aproximamos por medio de la fórmula de actualización de memoria-limitada BFGS [94, 24]. En cualquier caso, en esta tesis proponemos un enfoque eficiente que mantiene bajo control el coste computacional del cálculo de las matrices Jacobiana y Hessiana. Con el fin de hacer frente a la no unicidad

de los problemas de optimización no lineal, se puede emplear también emplear un término de regularización en el funcional de coste. Adicionalmente, hemos implementado la posibilidad de elegir el modo a utilizar a la hora de llevar a cabo la inversión. Así, podemos elegir entre emplear el modo TE, el TM, o los dos modos al mismo tiempo (TE+TM) para definir y resolver el problema inverso.

Además, también damos el primer paso hacia un método adaptativo basado en la dimensión del problema (*Dimensionally Adaptive Method, DAM*). Cuando la resistividad de los materiales que conforman el subsuelo terrestre depende de varias dimensiones espaciales, un preciso análisis de la dimensionalidad del problema [165, 85, 75] hace que en ocasiones sea posible considerar diferentes dimensiones para diferentes regiones del subsuelo. Por ejemplo, es común la situación en la que la formación consiste en un modelo 1D por capas con una inhomogeneidad 2D dentro de una de ellas. Basándose en esta interpretación del problema, el método DAM trata de sacar ventaja. De este modo, la idea principal del método consiste en llevar a cabo una adaptatividad en la variable espacial del problema. Se comienza resolviendo un problema de baja dimensionalidad y se utilizan los resultados del mismo con la finalidad de minimizar el costo de los problemas de mayor dimensionalidad. Así, resolvemos nuestro problema inverso 1D para a continuación utilizar como información a priori su solución en el problema inverso 2D. Dado que la solución 1D para una formación del subsuelo en capas admite una solución analítica, este proceso es rápido y computacionalmente barato. Para el problema 2D, tanto la solución de la formulación completa como la del campo secundario son válidas, resultando la segunda más rápida por requerir un menor número de incógnitas. Una ventaja fundamental de este enfoque es que al emplear como información a priori la solución de un problema de dimensión inferior que está estrechamente relacionado con la física del problema, aumentamos la robustez del algoritmo.

Esta tesis proporciona asimismo un **análisis numérico riguroso de diversas propiedades de los problemas MT**. En particular, hemos: (a) estudiado el efecto de la fuente, (b) completado un análisis de sensibilidad de frecuencia, (c) ilustrado el aumento de la convergencia cuando se emplea la adaptatividad-*hp*, (d) separado los efectos 1D y 2D de la solución numérica, (e) explorado el impacto de considerar diferentes variables para llevar a cabo la inversión, y (f) comparar el rendimiento que cada modo (TE, TM y el conjunto TE+TM) dan a la hora de la inversión.

Al lidiar con una fuente natural de la cual desconocemos la intensidad, lo lógico es emplear una magnitud física independiente de la intensidad de la fuente. Dado que los campos EM dependen de ella, las magnitudes relevantes en MT resultan ser el **tensor de impedancia** (una cantidad no lineal cuyas entradas se definen como el cociente entre las componentes de los campos eléctrico y magnético) y la resistividad aparente (una cantidad posprocesada de la impedancia). Las simulaciones numéricas realizadas en esta tesis muestran la diferente naturaleza de las soluciones numéricas obtenidas para la

impedancia y para los campos EM. El ejemplo más destacado de este fenómeno surge al analizar el comportamiento de la PML. En este trabajo mostramos que es necesario llevar a cabo esta truncación de forma correcta para obtener soluciones precisas de los campos EM; resultado esperado físicamente. Sin embargo, sorprendentemente las impedancias (y también las resistividades aparentes) son muy precisas incluso cuando truncamos el dominio con condiciones de Dirichlet homogéneas, escenario en el que se producen una gran cantidad de ondas EM reflejadas en el dominio.

En definitiva, los principales logros de investigación alcanzados con la tesis son:

- Desarrollar un software que resuelve completamente el problema MT 2D empleando por primera vez el método auto-adaptativo MEF-*hp*.
- Implementar y utilizar la adaptatividad orientada a varios objetivos para obtener resultados precisos en diferentes receptores al mismo tiempo.
- Diseñar una PML que ajusta automáticamente sus parámetros, lo cual resulta especialmente útil para la inversión.
- Resolver con precisión el problema MT directo.
- Implementar una formulación del campo secundario donde el campo primario viene dado por la solución a una formación 1D de la Tierra de capas horizontales.
- Proporcionar un primer paso para considerar la dimensión física del problema como una variable del problema inverso.
- Suministrar un marco matemático preciso en el contexto del MEF que ayude a comprender el problema MT y su inversión.
- Llevar a cabo un análisis numérico riguroso. En particular, hemos considerado los siguientes aspectos:
 - El efecto del tamaño de la fuente.
 - La sensibilidad de la solución con respecto a variaciones en la frecuencia.
 - La convergencia del algoritmo de *hp*-adaptativo.
 - El impacto de la variable seleccionada para la inversión.
 - La distinta información que cada modo proporciona.
 - El efecto de la PML en el cálculo de los campos EM y la impedancia.

La tesis se organiza como sigue. El capítulo 1 introduce la base del método MT: los principales conceptos, ecuaciones y magnitudes físicas. En el capítulo 2 derivamos una formulación variacional adecuada para el contexto del MEF, definimos un PML conveniente para los problemas directos e inversos, derivamos la formulación del campo secundario y desarrollamos el marco matemático para implementar estas formulaciones

en el contexto del FEM. El Capítulo 3 describe el MEF- hp y la adaptatividad orientada a multi-objetivo que hemos implementado para construir nuestra discretización hp . En el capítulo 4 formulamos el problema inverso, describimos el método utilizado para resolver el problema de optimización no lineal derivado de la inversión, y también ofrecemos un procedimiento eficiente basado en el método adjunto para calcular las matrices Jacobianas y Hessianas. Además, también introducimos el concepto del DAM para la inversión. El capítulo 5 proporciona detalles de implementación interesantes, mientras que en el capítulo 6 ilustramos mediante los resultados numéricos las principales características y limitaciones de los métodos desarrollados, así como algunas características físicas interesantes observadas en las simulaciones MT. Finalizamos con el capítulo 7 donde se presentan las conclusiones y perspectivas para la investigación futura.

RÉSUMÉ

La magnéto-tellurique (MT) est une technique d'exploration de la Terre basée sur des mesures de champs électromagnétiques (EM). Une source naturelle (non artificielle) harmonique en temps et située dans l'ionosphère [164] produit un champ EM régi par les équations de Maxwell qui, en fonction de la fréquence de la source et de la conductivité du sous-sol, pénètre dans la Terre pour atteindre des profondeurs comprises entre plusieurs dizaines de mètres et des centaines de kilomètres. Les champs électromagnétiques sont enregistrés par plusieurs récepteurs placés sur la surface de la Terre. Ces mesures sont utilisées pour produire une *image* du sous-sol à partir d'un procédé d'inversion utilisant des méthodes numériques.

Dès sa conception, la méthode MT s'est très vite avérée utile en Géophysique, applicable pour l'exploration à des fins industrielles et l'expérimentation. Elle intervient par exemple pour explorer la croûte terrestre profonde, pour la prévision des séismes [60, 72] ou encore le stockage géologique du CO₂ [101]. Elle a aussi un impact sur l'expérimentation nécessaire pour développer davantage la technique de MT. Parmi les utilisations commerciales possible de la MT, il y a la prospection des hydrocarbures (pétrole et gaz), la géothermie, l'exploration minière, ainsi que la surveillance des hydrocarbures et des eaux souterraines [72]. Du fait que la méthode MT soit à relativement faible coût et que son impact sur l'environnement soit négligeable, l'industrie la considère comme particulièrement intéressante. De plus amples détails sur les principales caractéristiques de la méthode MT peuvent être trouvés, par exemple, dans les livres de Simpson et Bahr [130] et de Chave et Jones [27].

Les fondements théoriques de la méthode MT ont été établis dans les années 1950 par Tikhonov [150] et Cagniard [25]. La modélisation et les codes d'inversion des mesures MT ont évolués du mono-dimensionnel (1D) à des modèles tri-dimensionnels (3D) de la Terre, bien que ces derniers en soient toujours à leurs premiers pas.

Parmi toutes les méthodes numériques adaptées pour la simulation des mesures de MT, nous nous concentrons, dans cette thèse, sur les méthodes d'ordre élevé. Les méthodes d'ordre élevé ont été largement utilisées ces dernières années par les mathématiciens appliqués, dans une large gamme d'applications. Par exemple, leur utilisation a considérablement augmenté récemment dans le domaine de la mécanique numérique et dans

diverses applications d'ingénierie. En particulier, l'analyse isogéométrique (IGA) [58, 127] a connu, ces dernières années, une colossale expansion et a été appliquée à l'industrie mécanique, de même que la plus récente méthode de Petrov-Galerkine discontinue (DPG), initialement proposée par Demkowicz et Gopalakrishnan [40, 171], ou encore la méthode des éléments finis auto-adaptatifs en hp (hp -FEM) [37, 50, 146] (où h correspond à la taille des éléments et p à l'ordre d'approximation associé à chaque élément).

Ici, nous utilisons la méthode hp -FEM résultant d'une extension du travail de Demkowicz et al. [37]. Nous avons développé un logiciel qui résout, pour la première fois, le problème MT avec des éléments finis auto-adaptatifs. La méthode hp -FEM permet des raffinements locaux, à la fois en taille h et en ordre p sur les éléments, ce qui est un avantage notoire puisque la combinaison de ces deux types de critères permet de mieux capter la présence de singularités, fournissant ainsi des erreurs de discrétisation faible. C'est donc une méthode très précise dont la convergence est exponentielle [52, 7] même en présence de singularités, ce qui est une situation typique en MT. En raison des défis d'implémentation encore non résolus [42] et de la complexité technique des calculs hp -FEM en 3D, nous nous limitons, dans ce travail, à des calculs en 1D et 2D.

Pour le problème direct MT, il est seulement nécessaire d'obtenir des résultats précis au niveau des récepteurs. Par conséquent, l'adaptativité ciblée (proposé par Becker et Rannacher dans les années 90 [12]) devient un choix naturel pour construire le maillage d'éléments finis. Compte tenu d'une erreur de tolérance sur une grandeur physique présélectionnée ayant un intérêt en ingénierie (dans notre cas, les champs EM sont leurs grandeurs physiques considérées), l'objectif des stratégies d'adaptativité ciblée traditionnelles est de construire un maillage optimal dans le sens où l'on minimise la taille du problème nécessaire pour atteindre cette erreur de tolérance. Étant donné qu'il est nécessaire d'obtenir des résultats précis à de multiples positions, nous développons ici, et pour la première fois dans le cadre MT, un algorithme auto-adaptatif ciblé à objectifs multiples initialement proposé par Pardo dans [105]. Un des principaux avantages de cette approche est que nous sommes capables de mesurer l'erreur dans une norme ayant un sens géophysique.

Dans cette thèse, en employant une formulation de champ secondaire, nous faisons la distinction entre le champ primaire et le champ secondaire. Ce dernier présente moins de fluctuation (de plus petits gradients) que le champ total, et il peut être discrétisé avec des grilles plus grossières. Ainsi, les champs secondaires sont, en général, non seulement plus faciles à déterminer, mais aussi moins coûteux en calculs. En outre, nous remplaçons le champ primaire 0D couramment utilisé [161, 73, 123] par un champ primaire 1D correspondant à un ensemble unidimensionnel de couches géologiques. Ce scénario, plus réaliste en général, produit des résultats plus précis.

Pour les deux formulations, le champ total et le champ secondaire, le domaine de calcul est tronqué par un matériau absorbant (*Perfectly Matched Layer* PML) [17], qui est

conçu pour s'adapter automatiquement aux propriétés physiques des matériaux. En particulier, il s'ajuste efficacement à l'interface air-sol, où le contraste entre la conductivité des matériaux atteint jusqu'à seize ordres de grandeur.

Le problème inverse de MT s'exprime comme un problème d'optimisation non linéaire. Pour résoudre des problèmes d'optimisations non linéaires, on peut utiliser des méthodes déterministes ou non déterministes. Dans ce dernier cas, la convergence des méthodes d'optimisation globales (par exemple, les algorithmes génétiques, la méthode de Monte-Carlo ou le *grid search*) nécessite généralement un grand nombre d'itérations. Pour chaque itération, un (ou parfois plusieurs) problème MT direct doit être résolu. Obtenir la solution d'un seul problème MT direct nécessite de grandes ressources de calcul et, en raison de ce coût élevé, les méthodes déterministes ont été historiquement préférées au sein de la communauté MT, en particulier les méthodes à base de gradient qui exigent moins d'évaluations du problème direct pour atteindre la convergence. Cependant, ces méthodes nécessitent de calculer des dérivées premières (matrice jacobienne) voire secondes (matrice hessienne), ce qui peut être chronophage. L'implémentation des calculs doit donc être réalisée efficacement. L'autre grand inconvénient des méthodes à base de gradient est qu'elles peuvent converger vers des minima locaux.

Dans notre travail, nous employons la méthode L-BFGS-U (Broyden, Fletcher, Goldfarb et Shanno) [170], qui est une méthode à base de gradient particulièrement adaptée pour la MT car elle utilise moins de mémoire que la méthode BFGS. C'est une méthode de quasi-Newton dans laquelle on approche la Hessienne [94, 24]. Néanmoins, nous fournissons une approche efficace pour calculer les matrices jacobiennes et hessiennes (si nécessaire) sans trop augmenter le coût de calcul. Afin de faire face à la non unicité des problèmes d'optimisation non linéaires, nous employons un terme de régularisation.

Dans cette thèse, nous présentons également des résultats préliminaires pour la mise en place d'une technique dimensionnelle adaptative plus connue sous le nom de DAM (**Dimensionally Adaptive Method (DAM)**). Lorsque la distribution de la résistivité du sous-sol dépend de multiples variables spatiales, une analyse correcte de la dimensionnalité [165, 85, 75] rend parfois possible de considérer les différentes régions avec des dimensions spatiales différentes. Par exemple, il est parfois possible d'interpréter la distribution comme une formation unidimensionnelle plus quelques hétérogénéités en 2D (ou 3D). Basée sur cette interprétation, la DAM tire profit d'une telle situation. Ainsi, l'idée principale de cette méthode est d'effectuer l'adaptativité sur la dimension spatiale en commençant par un problème de faible dimension et en utilisant les résultats obtenus pour minimiser le coût des problèmes de dimension supérieure. Nous commençons l'inversion avec un modèle 1D. Les résultats de ce problème d'inversion 1D sont utilisés comme information *a priori* sur les modèles de dimension supérieure. Puisque la solution 1D pour un milieu stratifié peut être déterminée analytiquement, ce processus est rapide et peu coûteux. Pour le problème 2D, la solution de la formulation de champ secondaire

est valide, ce qui est plus rapide à calculer que la solution de la formulation complète. Un avantage fondamental de cette approche est que nous pouvons utiliser les solutions des problèmes de dimension inférieure précédemment calculées comme composantes du terme de régularisation associé à un problème de dimension supérieure afin d'augmenter la robustesse de l'inversion.

Cette thèse propose également une **analyse numérique rigoureuse de divers aspects des problèmes MT**. En particulier, nous avons : (a) étudié l'effet de la source, (b) effectué une analyse fréquentielle de sensibilité, (c) illustré l'augmentation du taux de convergence lorsque l'adaptativité *hp* est employée, (d) séparé les effets 1D et 2D dans la solution numérique et (e) exploré l'intérêt de considérer différentes variables pour effectuer l'inversion.

Les champs EM dépendent de l'intensité de la source. Par conséquent, il est naturel d'utiliser une grandeur physique indépendante de l'intensité de la source plutôt que les champs EM. Plus précisément, les grandeurs pertinentes en magnéto-tellurique sont les **tenseurs d'impédance** (une quantité non linéaire dont les coefficients sont définis comme les rapports entre les composantes des champs électriques et magnétiques) et de la résistivité apparente. Les simulations numériques effectuées dans cette thèse montrent les différentes natures des solutions numériques obtenues pour l'impédance et pour les champs électromagnétiques. L'exemple le plus frappant apparaît lors de l'analyse du comportement de la PML automatiquement adaptée. Nous montrons la nécessité de tronquer correctement le domaine pour obtenir des champs EM précis, comme attendu physiquement. Étonnamment, les impédances (et aussi les résistivités apparentes) sont très précises même quand on tronque le domaine avec des conditions de Dirichlet homogènes, produisant une grande quantité d'ondes électromagnétiques réfléchies dans le domaine.

En résumé, les principaux résultats de recherche de la thèse sont:

- Développement d'un logiciel qui permet de résoudre le problème MT en 2D en employant, pour la première fois, une discrétisation *hp*-FEM.
- Mise en oeuvre et utilisation de l'adaptativité ciblée à objectifs multiples pour obtenir des résultats précis au niveau de différents récepteurs en même temps.
- Conception d'une PML qui ajuste automatiquement ses paramètres, ce qui est particulièrement utile pour l'inversion.
- Résolution du problème MT direct avec précision.
- Mise en oeuvre, à la fois, de la formulation directe complète et d'une formulation de champ secondaire où le champ primaire est donné par la solution dans un milieu stratifié mono-dimensionnel.

- Étude préliminaire en vue de traiter la dimension du problème comme une variable dans l'inversion.
- Définition d'un cadre mathématique rigoureux dans le contexte de la FEM qui aide à comprendre le problème de MT et son inversion.
- Analyse numérique rigoureuse de la MT. En particulier, les aspects suivants ont été examinés :
 - L'effet de la source.
 - Une analyse de sensibilité en fréquence.
 - La convergence de l'algorithme *hp*-adaptatif.
 - L'impact de la variable choisie pour le processus d'inversion.
 - Les différentes informations que fournit chaque mode.
 - L'effet de la PML dans le calcul des champs EM et de l'impédance.

La thèse est organisée comme suit. Le chapitre 1 présente la méthode MT c'est-à-dire les principaux concepts, les équations et grandeurs physiques correspondantes. Dans le chapitre 2, nous obtenons une formulation variationnelle appropriée dans le contexte de la FEM, nous définissons une PML pour les problèmes direct et inverse, nous déduisons la formulation de champ secondaire et nous définissons un cadre mathématique pour mettre en oeuvre ces formulations dans le contexte de la FEM. Le chapitre 3 décrit la *hp*-FEM et l'adaptativité ciblée à objectifs multiples développée pour construire nos discrétisations *hp*. Dans le chapitre 4, nous formulons le problème inverse, nous décrivons la méthode à base de gradient utilisée pour résoudre le problème d'optimisation venant de l'inversion, et nous fournissons également une procédure efficace basée sur l'adjoint pour calculer les matrices jacobienne et hessienne. De plus, nous décrivons également le concept de DAM pour l'inversion. Le chapitre 5 fournit les détails de mise en oeuvre les plus pertinents, tandis que dans le chapitre 6, des résultats numériques illustrent les principales caractéristiques et les limites des méthodes développées ainsi que certaines caractéristiques physiques intéressantes observées dans les mesures MT. Enfin, au chapitre 7, nous présentons les conclusions et des perspectives de recherche futures.

INTRODUCTION

The magnetotelluric (MT) method is an Earth exploration technique based on electromagnetic (EM) measurements. A natural (non-artificial) time-harmonic source located at the ionosphere [164] produces an EM field governed by Maxwell's equations that, depending upon the source frequency and subsurface conductivity, penetrates into the Earth subsurface a distance that ranges between tens of meters and hundreds of kilometers. EM fields are recorded at several receivers placed on the Earth's surface. These measurements are postprocessed (inverted using numerical methods) in order to obtain an *image* of the Earth's subsurface.

The theoretical foundations of the MT method were established in the 50's by Tikhonov [150] and Cagniard [25]. As it is a relatively low cost method and its environmental impact is negligible, the industry considers it particularly interesting. Since its conception the interest in the method rapidly increased, within the area of Geophysics, exploration with industrial purposes, and instrumentation. Research applications include experimentation to further develop the MT technique, long-period deep crustal exploration, earthquake precursor prediction research [60, 72], or CO₂ geological storage [101]. Commercial uses include hydrocarbon (oil and gas) exploration, geothermal, and mining exploration, as well as hydrocarbon and groundwater monitoring [72]. Extended physical details of the main features of the MT method can be found, for instance, in the books of Simpson and Bahr [130] and Chave and Jones [27].

Modeling and inversion codes of MT measurements have evolved from one-dimensional (1D) to three-dimensional (3D) Earth models, although the latter is still on its first steps. Among all the possible numerical methods suitable for simulating MT measurements, in this dissertation we focus on higher order methods. Higher order methods have been extensively used in the last years in applied mathematics in a variety of applications. For example, its use has dramatically increased recently in the area of computational mechanics and in various engineering applications. In particular, the isogeometric analysis (IGA) [58, 127] has recently experimented a huge explosion and it has been applied to the engineering industry, as well as the more recent Discontinuous Petrov-Galerkin (DPG) method initially proposed by Demkowicz and Gopalakrishnan [40, 171], or the self-adaptive **hp-Finite Element Method (FEM)** [37, 50, 146] (where h stands for the element size and p for the order of approximation associated to each element).

In here, we employ the *hp*-FEM, and based on an extension of the work of Demkowicz et al. [37], we have developed a software to solve for the first time the MT problem employing the self-adaptive *hp*-FEM. The *hp*-FEM allows both h and p local refinements across elements, which is a notorious advantage since the combination of both types of refinements allows to better capture the presence of singularities, thereby providing low discretization errors. It is thus a highly accurate method that provides exponential con-

vergence [52, 7] even when these singularities are present, a typical situation that occurs in MT. Due to the still unsolved implementation challenges [42] and technical complexity of 3D *hp*-FEM computations, in this work we restrict to 1D and 2D MT computations only.

In the MT forward problem, it is necessary to obtain accurate results only at the receivers. Hence, the goal-oriented adaptivity (first proposed by Becker and Rannacher in the mid 90's [12]) becomes a natural choice to build the finite element mesh. Given a tolerance error of a preselected physical magnitude of engineering interest (in our case the EM fields), the objective of traditional goal-oriented strategies is to construct an optimal grid in the sense that it minimizes the problem size needed to achieve this tolerance error. Since it is necessary to obtain accurate results at multiple receiver positions, in here we develop, for the first time in the MT context, a multi-goal oriented self-adaptive algorithm originally proposed by Pardo in [105]. One of the main advantages of this approach is that we are able to measure the error in a geophysically meaningful norm.

By employing a secondary field formulation, in this dissertation, we discern between the primary field and secondary field variations. The latter exhibits less fluctuations (smaller gradients) than the total field, and it can be discretized with coarser grids. Thus, secondary fields are in general not only easier to determine, but also computationally cheaper. Besides, we replace the commonly used 0D primary field [161, 73, 123] by a 1D primary field corresponding to a 1D layered Earth's formation, which corresponds to a more realistic scenario in general.

To truncate the computational domain of the forward direct problem (for both, the full field and secondary field formulations), we design an **automatically adapted Perfectly Matched Layer (PML)**, that adjusts the parameters, even if the material properties change abruptly, without further user interaction. Hence, it automatically adapts to high-contrast material properties that appear within the subsurface and on the air-ground interface.

To truncate the computational domain of the forward direct problem (for both the full field and secondary field formulations), we design an **automatically adapted Perfectly Matched Layer (PML)** that adjusts the parameters even in case material properties change abruptly, without further user interaction. Hence, the procedure adapts automatically to high-contrast material properties that appear within the subsurface and on the air-ground interface.

The MT inverse problem is defined as a nonlinear optimization problem. The methods to solve these type of optimization problems can be classified into deterministic and non-deterministic. Within the latter, the convergence of global optimization methods (e.g., genetic algorithms, Monte-Carlo search or grid search) typically requires a large number of iterations. In each of these iterations, one (or several) MT forward problems have to be solved. To obtain a solution for a single forward problem in MT requires implies large computational resources, and because of the elevated cost involved on solving a MT forward problem, deterministic methods have been historically preferred within the MT community. Especially, gradient based methods, which demands fewer evaluations of the forward problem to achieve convergence. However, these methods employ first (and even

second) order derivatives in the form of the Jacobian (or the Hessian if needed), which may be highly time consuming. Therefore, an efficient implementation for computing them is necessary. The other main drawback of gradient based methods is that they only find a local minima.

In our work, we employ the L-BFGS-U (Broyden, Fletcher, Goldfarb, and Shanno) method [170], which is a gradient based method especially suitable for simple bounded problems. Being a quasi-Newton method, it is unnecessary to explicitly compute the Hessian, which is approximated with the limited-memory BFGS approximation updating formula [94, 24]. Nonetheless, we provide an efficient approach to compute the Jacobian and Hessian (if needed) matrices without increasing excessively the computational cost. Additionally, we also implement the inversion for the TE mode, the TM mode, and the joint TE+TM modes.

In this dissertation, we also develop the first step towards a **Dimensionally Adaptive Method (DAM)**. When the subsurface distribution of the resistivity depends upon multiple spatial variables, a proper dimensionality analysis [165, 85, 75] often enables to consider different regions with different spatial dimension. For instance, in many scenarios it is possible to interpret a given 3D problem as a 1D formation plus some 2D (or 3D) inhomogeneities. In these scenarios, the DAM takes advantage by locally reducing the dimensionality of the problem. The main idea of the method consists of performing adaptivity in the spatial dimension by starting with a low-dimensionality problem and use the corresponding results to minimize the computational cost of high-dimensionality problems. In this work, we start our inversion with a 1D model. Results of this 1D inversion problem are used as a priori information on the subsequently enriched higher-dimensional models. Since the 1D solution for a layered media admits an analytical solution, this process is fast and computationally inexpensive. For the 2D problem, the solution for the secondary field formulation is valid, which is faster than the full formulation solution. A fundamental benefit of this approach is that we can employ the information of previously computed lower dimensional solutions as part of the regularization term of a higher dimensional problem to increase the robustness of the inversion.

This dissertation also provides a **rigorous numerical analysis of various aspects of MT problems**. In particular, we have: (a) studied the effect of the source, (b) completed a frequency sensitivity analysis, (c) illustrated the increase in the convergence rate when the *hp* adaptivity is employed, (d) separated 1D and 2D effects in the numerical solution, (e) explored the impact of considering different variables to perform the inversion, and (f) compared the performance of the inversion when the TE mode, the TM mode, or the joint TE+TM modes are employed.

The EM fields depend on the intensity of the source. Therefore, it is natural to employ a physical magnitude independent of the source intensity rather than the EM fields. More precisely, the relevant magnitudes in MT are the **impedance tensor** (a nonlinear quantity whose entries are defined as ratios between the electric and magnetic field components) and the apparent resistivity (a postprocessed quantity from the impedance). The numerical simulations performed in this dissertation show the different nature of the numerical

solutions obtained for the impedance and for the EM fields. The most prominent example of this fact appears when analyzing the behavior of the PML. We show the necessity of properly truncating the domain in order to obtain accurate EM fields, as physically expected. Surprisingly, impedances (and also the apparent resistivities) are highly accurate even when we truncate the domain with homogeneous Dirichlet conditions, producing a great amount of reflected EM waves into the domain.

The dissertation is organized as follows. Chapter 1 introduces the basis of the MT method: the main concepts, equations and physical magnitudes. In Chapter 2 we derive a suitable variational formulation in the context of the FEM, we define a convenient PML for the forward and inverse problems, we derive the secondary field formulation and we provide the mathematical setting to implement these formulations in the context of the FEM. Chapter 3 describes the *hp*-FEM and the multi-goal oriented adaptivity developed to build our *hp*-discretizations. In Chapter 4 we formulate the inverse problem, we describe the gradient based method employed to solve the optimization problem arisen from the inversion, and we also provide an efficient adjoint-based procedure to compute the Jacobian and Hessian matrices. In addition, we also describe the concept of the DAM for inversion. Chapter 5 provides insightful implementation details, while in Chapter 6 the numerical results illustrate the main features and limitations of the developed methods as well as some interesting physical characteristics observed in MT measurements. Finally, in Chapter 7 we present the conclusions and perspectives for the future research.

DESCRIPTION OF THE MAGNETOTELLURIC METHOD

The magnetotelluric (MT) method is a passive electromagnetic (EM) exploration technique aiming at estimating the resistivity distribution of the subsurface on scales varying from few meters to hundreds of kilometers [125]. Natural EM sources induce electric currents in the Earth, and these currents generate secondary fields. By measuring simultaneously the horizontal components of these fields on the Earth's surface, it is possible to obtain information about the electrical properties of the subsurface.

The depth of penetration of the EM fields depends on the frequency. Geomagnetic fluctuations typically range between $10^{-5} - 10^3$ Hz [155]. The Earth's time-varying magnetic field is generated mainly by two different sources, which strongly differ in amplitude and frequency. The MT method works with the external small-amplitude (long period) geomagnetic variations, which induce eddy currents and secondary magnetic fields in the Earth. The other source comes from the so called magneto-hydrodynamic process that takes place in the Earth's outer core. However, to our purposes, we can assume that these fields are negligible.

The ionosphere is the region where the source for the MT problem is located. It is in between the neutral atmosphere and the magnetosphere, which contains gases (oxygen and nitrogen) that are ionized by the solar radiation. The solar wind, which is a stream of charged particles ejected from the Sun, produces a radiation pressure that causes a compression on the day-side and a tail on the dark-side onto the magnetosphere. Due to this interaction, hydromagnetic waves are generated. When those waves reach the ionosphere, they induce an EM field that works as power source in MTs. It is then realistic to treat this field as plane waves that propagate in the vertical direction towards the Earth's surface due to the remote origin of the source [154]. Once the plane wave arrives to the Earth's surface, scattered waves are generated by subsurface heterogeneities.

In the frequency range $0.5 - 5$ Hz, the MT measurements are of poor quality and the signal amplitude is very low. This frequency range is called *dead-band* and it corresponds to the transition region between the short and long periods. In fact, at these frequencies, due to the interaction with the meteorological activity, local lightning discharges may appear as peaks in the data. Throughout this work, we consider locations situated in mid-latitudes, and a frequency range of $10^{-5} - 10^2$ Hz, although in most simulations we restrict ourselves to the most sensitive range ($10^{-4} - 1$) Hz. These frequencies will allow us to make measurements with a resolution varying from a few meters to hundreds of kilometers [156].

There are several benefits of using natural sources as in MT's. It is an inexpensive technique because no artificial power is required. Moreover, it covers a vast area and it is innocuous for the environment since high intensity EM fields are not used. However, as natural sources, they are uncontrollable and this may pollute the results. Therefore, pre and post processing of the data are usually necessary. In general, the results have low resolution, which makes small features in the formation difficult to identify and/or characterize.

The theoretical foundations of MT method were established in the 50's by Tikhonov [150] and Cagniard [25]. The scientific literature acknowledges that Tikhonov's work was pioneer, and it also accepts that Cagniard built his theory independently. They considered a multilayered Earth and idealized the natural geomagnetic sources as plane waves hitting the plane surface of the Earth.

In 1954, Wait [158] questioned the assumption on plane wave geomagnetic source after he showed that finite ionosphere sources were unable to generate normally incident plane waves. It is in 1962 that Price [117] elaborated a general theory for MT methods based on finite dimensions of the source field. Later on, in 1964 [82] and 1965 [143], computer modeling studies showed that the plane wave assumption was valid for realistic Earth conductivity profiles for periods up to 10^3 seconds (even up to 10^5 in mid-latitudes [143, 144]).

The Cagniard's scalar representation of the impedance was substituted by a tensorial relationship between electric and magnetic fields. Thus, the admittance [93, 20] and impedance tensors [15, 151] were introduced. These quantities are able to provide valuable information regarding zones with lateral conductivity variations.

Regarding numerical simulation for geomagnetic applications, classical approaches such as finite differences (FD), integral equations (IE) or finite element methods (FEM) have been applied. The first FD algorithm for two-dimensional (2D) modeling of geomagnetic fields (applied to a formation with vertical discontinuities in conductivity) dates back to 1970 [70]. Taylor and Weaver [22] provided a revision of the theory for 2D FD approximations in order to generalize the method to 3D models, which was introduced by Mackie et al [80] afterwards, and applied to the MT problem in [81]. Integral equation methods have been used to derive the EM response of a 3D heterogeneity in a three-layered medium [121], to model 3D bodies in layered formations [160], or to simplify the treatment of the EM induction in 3D models [102]. They have also been applied for modeling 3D MT problems by Ting and Hohmann [152] and Wannamaker [159], but these methods can not be applied to general geometries, since they are based on the analytical representation of the corresponding Green functions. The FEM for geoelectromagnetic modeling was first used by Coggon [30] using triangular elements, while quadrilateral elements were employed for instance by Wannamaker et al [161]. More recently, adaptive FEMs over unstructured grids have been applied by Key and Weiss [73] and [45]. It is also usual to employ discretization grids where a constant value of the conductivity is assigned for each cell/element (see [134, 169]).

1.1 EM PROPERTIES OF EARTH MATERIALS

The penetration of an incident wave in a given formation depends both on, its frequency and the EM properties of the medium.

- The *electrical conductivity* σ , or the *resistivity* $\rho = \sigma^{-1}$, measures the ability of a material to conduct an electrical current. It relates the electric current density \mathbf{j} to the electric field \mathcal{E} *via* the first constitutive equation, known as Ohm's Law:

$$\mathbf{j} = \sigma \mathcal{E}, \quad (1.1)$$

where σ (in Sm^{-1} , where S stands for Siemens) is a second rank tensor in the case of an anisotropic substratum (anisotropy effects indeed exist in near or upper crystal [63] and at greater depths [68]), defined as

$$\sigma(x, y, z) = \begin{pmatrix} \sigma_{xx} & \sigma_{xy} & \sigma_{xz} \\ \sigma_{yx} & \sigma_{yy} & \sigma_{yz} \\ \sigma_{zx} & \sigma_{zy} & \sigma_{zz} \end{pmatrix}. \quad (1.2)$$

The conductivity is assumed to be expressed as a diagonal matrix with positive entries. Moreover, it is common to assume [141] that $\sigma_{xx} = \sigma_{yy}$ to end up with a tensor of the form:

$$\sigma(x, y, z) = \begin{pmatrix} \sigma_h & 0 & 0 \\ 0 & \sigma_h & 0 \\ 0 & 0 & \sigma_v \end{pmatrix}, \quad (1.3)$$

where σ_h stands for the horizontal variation of the conductivity and σ_v for the vertical variation. For simplicity, in this dissertation we consider isotropic scenarios where the conductivity is a diagonal tensor of the form:

$$\sigma(x, y, z) = \begin{pmatrix} \sigma & 0 & 0 \\ 0 & \sigma & 0 \\ 0 & 0 & \sigma \end{pmatrix}. \quad (1.4)$$

The extension of the presented results to anisotropic scenarios of the form of equation (1.3) is straightforward (see Appendix 8.1).

- The *electrical permittivity* ϵ is the physical magnitude that relates the electric field \mathcal{E} to the electric displacement \mathcal{D} (in Cm^{-2} where C stands for Coulombs) *via* the second constitutive equation

$$\mathcal{D} = \epsilon \mathcal{E}, \quad (1.5)$$

and measures the material ability to be polarized by an external electric field. ϵ is a second rank tensor with ϵ in its main diagonal, which is given by the electrical permittivity

$\epsilon_0 = 8.854 \cdot 10^{-12}$ of the vacuum (in Fm^{-1} , where F denotes Faradays) and the unit-less relative electrical permittivity ϵ_r , which is specific to the material

$$\epsilon = \epsilon_r \cdot \epsilon_0. \quad (1.6)$$

The relative electrical permittivity in the Earth's subsurface varies from $\epsilon_r = 1$ in the vacuum to $\epsilon_r = 80.36$ in water at 20°C .

- The *magnetic permeability* μ measures the degree of magnetization of a material that linearly responds to an applied magnetic field. It links the magnetic induction \mathcal{B} (in Teslas (T)) to the magnetic intensity \mathcal{H} (in Am^{-1} , where A denotes Amperes) *via* the third constitutive equation

$$\mathcal{B} = \mu \mathcal{H}, \quad (1.7)$$

where μ is a second rank tensor with μ in its main diagonal. μ is a combination of the vacuum permeability $\mu_0 = 4\pi 10^{-7}$ (in Hm^{-1} , where H stands for Henry) and the unit-less permeability μ_r , which is specific to the material according to

$$\mu = \mu_r \cdot \mu_0. \quad (1.8)$$

We assume that material data are time-independent and bounded, that is

$$\begin{aligned} 0 < \epsilon^{min} < \epsilon < \epsilon^{max} < \infty, \\ 0 < \mu^{min} < \mu < \mu^{max} < \infty, \\ 0 \leq \sigma_i \leq \sigma^{max} < \infty. \end{aligned} \quad (1.9)$$

Since we do not consider formations with highly magnetized minerals, the common assumption $\mu = \mu_0$ is valid.

1.2 GOVERNING EQUATIONS: MAXWELL'S EQUATIONS

The fundamental partial differential equations governing the behavior of EM fields are given by Maxwell's equations: ¹

- Faraday's Law (1831):

$$\nabla \times \mathcal{E} = -\frac{\partial}{\partial t}(\mu \mathcal{H}) - \mathcal{M}^{imp}. \quad (1.10)$$

- Ampère's Law (1820) with Maxwell's correction (1856):

$$\nabla \times \mathcal{H} = \mathcal{J}^{imp} + \sigma \mathcal{E} + \frac{\partial}{\partial t}(\epsilon \mathcal{D}). \quad (1.11)$$

¹ International System of Units (SI) has been used here and throughout the entire work.

- Gauss Law for Electricity:

$$\nabla \cdot (\varepsilon \mathcal{E}) = \rho_f. \quad (1.12)$$

- Gauss Law for Magnetism:

$$\nabla \cdot (\mu \mathcal{H}) = 0, \quad (1.13)$$

arising from the constitutive relations (1.1), (1.5), and (1.7). In the above equations, ρ_f (in Cm^{-3}) stands for electric charge density, \mathcal{J}^{imp} and \mathcal{M}^{imp} denote the impressed and magnetic current sources, respectively. $\mathcal{J} := \mathcal{J}^{imp} + \sigma \mathcal{E}$ (in Am^{-3}) is the total current and $\frac{\partial \mathcal{D}}{\partial t}$ is the electric displacement current.

The free charge density is obtained using the continuity (conservation of free charge) equation:

$$\nabla \cdot \mathcal{J} + \frac{\partial \rho_f}{\partial t} = 0. \quad (1.14)$$

Applying the divergence operator to both sides of Faraday's Law, we have that

$$\frac{\partial}{\partial t} \left(\nabla \cdot (\mu \mathcal{H}) \right) = 0. \quad (1.15)$$

Assuming that $\mathcal{H}(0)$ satisfies the Gauss Law for the magnetic flux, (1.12) is satisfied at any time. Applying the divergence to both sides of Ampère's Law, we have that

$$\frac{\partial}{\partial t} \left(\nabla \cdot (\varepsilon \mathcal{E}) - \rho_f \right) = 0, \quad (1.16)$$

and assuming that the electric flux satisfies the Gauss law at $t = 0$, (1.13) is satisfied at any time.

FREQUENCY DOMAIN:

In order to obtain Maxwell's equations in frequency domain, we assume the ansatz

$$\mathbf{E}(\mathbf{x}, t) = \text{Re}(\mathcal{E}(\mathbf{x})e^{j\omega t}), \quad (1.17)$$

and we inject it into the above equations. Thus, they can be written in frequency domain as:

$$\left\{ \begin{array}{ll} \nabla \times \mathbf{E} & = -j\omega \mu \mathbf{H} - \mathcal{M}^{imp} & \text{Faraday's Law.} \\ \nabla \times \mathbf{H} & = (\sigma + j\omega \varepsilon) \mathbf{E} + \mathcal{J}^{imp} & \text{Ampère's Law.} \\ \nabla \cdot (\varepsilon \mathbf{E}) & = \rho_f & \text{Gauss' Law of Electricity.} \\ \nabla \cdot (\mu \mathbf{H}) & = 0 & \text{Gauss' Law of Magnetism,} \end{array} \right. \quad (1.18)$$

where \mathbf{E} and \mathbf{H} are the electric and magnetic fields in the frequency domain, respectively. These fields are driven by an impressed prescribed electric and magnetic density current sources, denoted and defined by $\mathcal{J}^{imp} = (0, J_y, 0)$ and $\mathcal{M}^{imp} = (0, M_y, 0)$, respectively. We emphasize that, as explained in [53], magnetic impressed currents are only mathematical

symbols utilized to represent sources. Additionally, we only consider volumetric sources and therefore, surface currents are equal to zero, i.e., $\mathbf{J}_s = \mathbf{M}_s = 0$.

The time-domain solution can be recovered by applying the inverse Fourier transform, that is,

$$\mathbf{E}(\mathbf{x}, t) = \frac{1}{2\pi} \int_{-\infty}^{\infty} \mathbf{E}(\mathbf{x}, \omega) e^{j\omega t} d\omega. \quad (1.19)$$

Notice that the sign in the exponential in the inverse Fourier transform has to be consistent with the selected ansatz.

Pre-multiplying both sides of Faraday's Law by $\boldsymbol{\mu}^{-1}$, applying the curl, and using Ampère's Law, we obtain the *reduced wave equation*,

$$\nabla \times (\boldsymbol{\mu}^{-1} \nabla \times \mathbf{E}) - k^2 \mathbf{E} = -j\omega \mathbf{J}^{imp} - \nabla \times (\boldsymbol{\mu}^{-1} \mathbf{M}^{imp}), \quad (1.20)$$

where $k^2 = \omega^2 \boldsymbol{\varepsilon} - j\omega \boldsymbol{\sigma}$. A similar equation is obtained in terms of the magnetic field by pre-multiplying both sides of Ampère's Law by $\hat{\boldsymbol{\sigma}}^{-1} = (\boldsymbol{\sigma} + j\omega \boldsymbol{\varepsilon})^{-1}$ and applying the curl to Faraday's Law

$$\nabla \times (\hat{\boldsymbol{\sigma}}^{-1} \nabla \times \mathbf{H}) + j\omega \boldsymbol{\mu} \mathbf{H} = -\mathbf{M}^{imp} + \nabla \times (\hat{\boldsymbol{\sigma}}^{-1} \mathbf{J}^{imp}). \quad (1.21)$$

Given two media (1 and 2) with different material properties, the following interface conditions (which can be derived from the integral formulation of Maxwell's equations [163]) have to be satisfied across the interface that separates them. If $\hat{\mathbf{n}}$ denotes the unit (outward) vector normal to the interface, we have:

- The tangential components of the electric and magnetic (absence of surface currents) are continuous:

$$\hat{\mathbf{n}} \times (\mathbf{E}_1 - \mathbf{E}_2) = 0, \quad \hat{\mathbf{n}} \times (\mathbf{H}_1 - \mathbf{H}_2) = 0. \quad (1.22)$$

- The normal component of the displacement current is discontinuous because of the accumulation of the surface-charge density:

$$\hat{\mathbf{n}} \cdot (\boldsymbol{\varepsilon}_1 \mathbf{E}_1 - \boldsymbol{\varepsilon}_2 \mathbf{E}_2) = \rho_s, \quad (1.23)$$

where ρ_s (in Cm^{-2}) is the surface charge density.

- The normal component of the magnetic induction is continuous.

$$\hat{\mathbf{n}} \cdot (\boldsymbol{\mu}_1 \mathbf{H}_1 - \boldsymbol{\mu}_2 \mathbf{H}_2) = 0. \quad (1.24)$$

- The displacement currents are negligible in comparison with \mathbf{j} regarding the frequency range employed in MT [164]. Thus, the continuity of current density $\mathbf{j}_1 = \mathbf{j}_2$ implies that:

$$\hat{\mathbf{n}} \cdot (\boldsymbol{\sigma}_1 \mathbf{E}_1 - \boldsymbol{\sigma}_2 \mathbf{E}_2) = 0. \quad (1.25)$$

1.3 MAGNETOTELLURIC CHARACTERIZATION

1.3.1 The MT Transfer Functions

A transfer function is defined as a function that relates different fields depending on the electrical properties of the materials (electric and/or magnetic field) at a given frequency. The MT method works with natural sources of variable unknown intensity. Then, it is necessary to define the transfer functions to be independent of the intensity of the source.

The *Impedance* tensor \mathcal{Z} is a complex second rank frequency dependent tensor. It defines the relation between the horizontal components of the electric (E_x, E_y) and magnetic (H_x, H_y) fields (\mathbf{B} can also be used, and then the resulting tensor is known as the *Magnetotelluric* tensor),

$$\mathcal{Z} = \frac{\mathbf{E}}{\mathbf{H}} \quad \text{or} \quad \begin{pmatrix} E_x \\ E_y \end{pmatrix} = \begin{pmatrix} \mathcal{Z}_{xx} & \mathcal{Z}_{xy} \\ \mathcal{Z}_{yx} & \mathcal{Z}_{yy} \end{pmatrix} \begin{pmatrix} H_x \\ H_y \end{pmatrix}. \quad (1.26)$$

It is similar to the complex *Schmucker and Weidelt* transfer function $\mathcal{C} = \frac{\mathcal{Z}}{j\omega}$ [128].

The *Geomagnetic* transfer function \mathcal{T} , is a complex vector that relates the horizontal and the vertical magnetic components as follows

$$H_z = \begin{pmatrix} \mathcal{T}_x & \mathcal{T}_y \end{pmatrix} \begin{pmatrix} H_x \\ H_y \end{pmatrix}, \quad (1.27)$$

where vector \mathcal{T} consists of two real dimensionless vectors introduced in [114, 115] and [166], known as induction arrows and defined by the following dimensionless vectors:

$$\mathcal{T}_{Re} = \left(\text{Re}(\mathcal{T}_x), \text{Re}(\mathcal{T}_y) \right), \quad \mathcal{T}_{Im} = \left(\text{Im}(\mathcal{T}_x), \text{Im}(\mathcal{T}_y) \right). \quad (1.28)$$

Induction arrows are used to indicate the presence or absence of lateral variation in the conductivity, since the vertical magnetic fields are generated by lateral conductivity gradients [70, 67, 130].

1.3.2 Homogeneous Half Space: Skin Depth

The simplest model to be considered is a uniform half-space, with zero conductivity for the air and a planar surface with constant conductivity σ_1 for the subsurface. We employ this naive model illustrated in Figure 1.1, and the reduced wave equation satisfied by the electric field to define the *skin depth*.

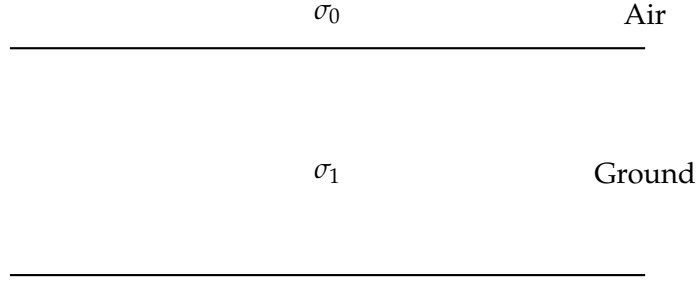


Figure 1.1: Homogeneous half-space model for the Earth's formation.

With this model for the Earth subsurface and assuming a normal incident plane wave (in the z direction), $\partial^2/\partial x^2 = \partial^2/\partial y^2 = 0$. The electric field is then solution to the following equation

$$\frac{\partial^2 \mathbf{E}}{\partial z^2} + \gamma^2 \mathbf{E} = 0, \quad (1.29)$$

where $\gamma^2 = \omega^2 \mu \epsilon - j \omega \mu \sigma$. Due to the range of frequencies involved in MTs, usually the *quasi-static* approximation is taken. We then have $\sigma \gg \epsilon \omega$, which justifies the following approximate value of γ^2 :

$$\gamma^2 = \omega^2 \mu \epsilon - j \omega \mu \sigma \simeq -j \omega \mu \sigma = \kappa^2. \quad (1.30)$$

Herein, for the sake of simplicity, we also employ this approximation to explain certain theoretical concepts such as skin depth and apparent resistivity. In actual FE computations, we refrain from using this approximation, since it provides no additional computational savings.

The solution to equation (1.29) is given by:

$$\mathbf{E} = A e^{j\kappa z} + B e^{-j\kappa z}, \quad (1.31)$$

where

$$\kappa = \sqrt{-j \omega \mu \sigma} = (1 - j) \sqrt{\frac{\omega \mu \sigma}{2}}. \quad (1.32)$$

The Earth only dissipates or absorbs EM energy, it does not generate it. Therefore, assuming that the value of z increases when entering into the subsurface, the electric field decreases as z increases. Consequently, $A = 0$, and we have that:

$$\mathbf{E} = B e^{-j\kappa z} = B e^{-j(1-j)\sqrt{\frac{\omega \mu \sigma}{2}}z} = B e^{-j\sqrt{\frac{\omega \mu \sigma}{2}}z} e^{-\sqrt{\frac{\omega \mu \sigma}{2}}z}. \quad (1.33)$$

The solution varies sinusoidally due to the complex term, and it is depth dependent because of the real term. The *skin depth* δ is the distance in which the EM waves amplitude decays by $1/e$ of its value when it penetrates a conductor, that is:

$$\delta = \sqrt{\frac{2}{\omega \mu \sigma}} \approx 503 \sqrt{\frac{2\pi}{\sigma \omega}}. \quad (1.34)$$

It decreases as the conductivity and the oscillation frequency increase, and therefore, the signal penetrates further in low conductivity media and at low frequencies.

1.3.3 1D Survey as a Layered Media: Apparent Resistivity

To study the relation between the transfer functions and the subsurface resistivity distribution, we consider a simple one-dimensional case given by a stratified model, as the one illustrated in Figure 1.2.

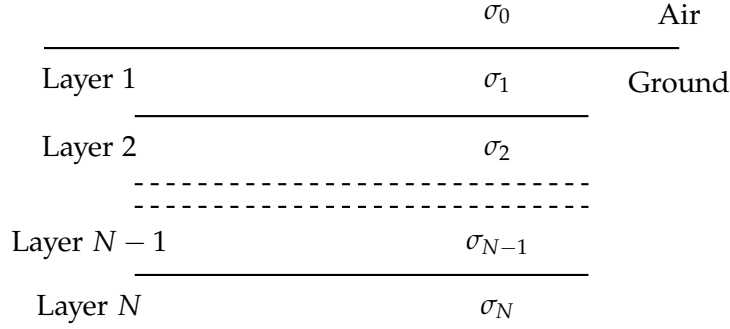


Figure 1.2: 1D layered Earth's formation.

The conductivity changes only with depth ($\sigma = \sigma(z)$), and $\partial/\partial x = \partial/\partial y = 0$. For this scenario, there exists an analytical solution (for example [158, 116, 28]). The solutions for the electric and magnetic fields are given in the i -th layer of height h_i by:

$$E_k^i(z, \omega) = A_i e^{j\gamma_i z} + B_i e^{-j\gamma_i z}, \quad H_l^i(z, \omega) = \frac{\gamma_i}{\omega \mu} (A_i e^{j\gamma_i z} - B_i e^{-j\gamma_i z}), \quad (1.35)$$

where k and l can be either x or y , the coefficients A_i and B_i depend on interface conditions, and $\gamma_i = \sqrt{\omega^2 \mu \epsilon - j\omega \mu \sigma_i}$ and σ_i are the wavenumber and conductivity associated to the i -th layer. The impedance at the surface is then given by:

$$\mathcal{Z}_{kl} = \frac{E_k^1(z=0)}{H_l^1(z=0)} = \frac{A_1 + B_1}{A_1 - B_1} \frac{\omega \mu}{\gamma_1} = C(n, \sigma_1, \dots, \sigma_n, h_1, \dots, h_n, \omega) \frac{\omega \mu}{\gamma_1}. \quad (1.36)$$

We compute the value of C for the particular case of the half space, which corresponds to a one-layer medium. From Faraday's Law, we have that

$$\frac{\partial E_y}{\partial z} = j\omega \mu H_x, \quad \text{and} \quad \frac{\partial E_x}{\partial z} = -j\omega \mu H_y. \quad (1.37)$$

Equation (1.33) implies that,

$$\frac{\partial E_y}{\partial z} = -j\gamma_1 E_y = j\omega \mu H_x, \quad \text{and} \quad \frac{\partial E_x}{\partial z} = -j\gamma_1 E_x = -j\omega \mu H_y. \quad (1.38)$$

The impedance measured at the surface is then given by

$$\mathcal{Z}_{yx}(\omega) = \frac{E_y(z=0)}{H_x(z=0)} = -\frac{\omega\mu}{\gamma_1} = -\frac{\omega\mu}{\sqrt{\omega^2\mu\varepsilon - j\omega\mu\sigma_1}} \simeq -\sqrt{\frac{j\omega\mu}{\sigma}} = (j-1)\sqrt{\frac{\omega\mu}{2\sigma}}. \quad (1.39)$$

Similarly, from the second equation in (1.38), we obtain

$$\mathcal{Z}_{xy}(\omega) = \frac{E_x(z=0)}{H_y(z=0)} = \frac{\omega\mu}{\gamma_1} \simeq \sqrt{\frac{j\omega\mu}{\sigma}} = (1-j)\sqrt{\frac{\omega\mu}{2\sigma}}. \quad (1.40)$$

Hence, in the particular case of the half-space case, we have $C = \pm 1$ (depending upon the involved fields) in equation (1.36). Additionally, from (1.39) and (1.40) we know that the real and imaginary parts of the impedance have the same magnitude, and therefore, the phase of the impedance tensor is equal to $\phi = 45^\circ$. Thus, any phase that is greater than 45° indicates a substratum where the resistivity decreases with depth (and the contrary for phases below 45°).

We define the *apparent resistivity* of the media from the impedance as

$$\rho_{kl}^{app} = \frac{1}{\sigma_{kl}^{app}} = \frac{1}{\omega\mu} |\mathcal{Z}_{kl}|^2, \quad (1.41)$$

and its phase as

$$\phi_{kl} = \tan^{-1} \left(\frac{\text{Im}(\mathcal{Z}_{kl})}{\text{Re}(\mathcal{Z}_{kl})} \right), \quad (1.42)$$

where k and l can be either x or y . The apparent resistivity is directly related to the actual subsurface resistivity distribution, and for the half-space, it corresponds to the actual one. For more complex scenarios, an approximation holds, and it corresponds to an average of the subsurface resistivities, as illustrated in Figure 1.3.

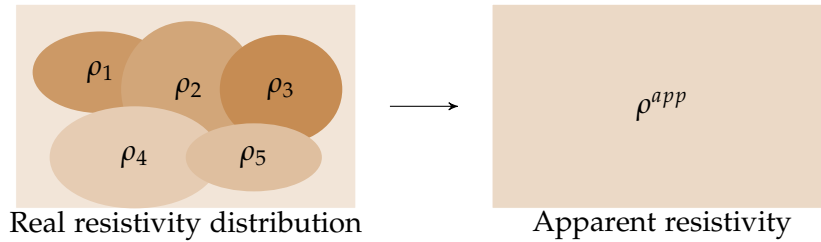


Figure 1.3: Illustration of the apparent resistivity.

The diagonal entries (\mathcal{Z}_{xx} and \mathcal{Z}_{yy}) of the impedance tensor, which are related to the parallel electric and magnetic fields, vanish in 1D media, and the off-diagonal entries are equal to each other but with opposite sign.

$$\mathcal{Z}_{1D} = \begin{pmatrix} 0 & \mathcal{Z}_{xy} \\ \mathcal{Z}_{yx} & 0 \end{pmatrix}, \quad \text{where} \quad \mathcal{Z}_{xy} = \frac{E_x}{H_y} = -\frac{E_y}{H_x} = -\mathcal{Z}_{yx}. \quad (1.43)$$

1.3.4 2D Survey-Along Strike Approach

We consider a 2D scenario where the conductivity only vary along x and z , that is $\sigma = \sigma(x, z)$. Thus, assuming an infinite extension along the strike direction y as in the simple model shown in Figure 1.4, we have $\partial/\partial y = 0$. The current density has to be kept across

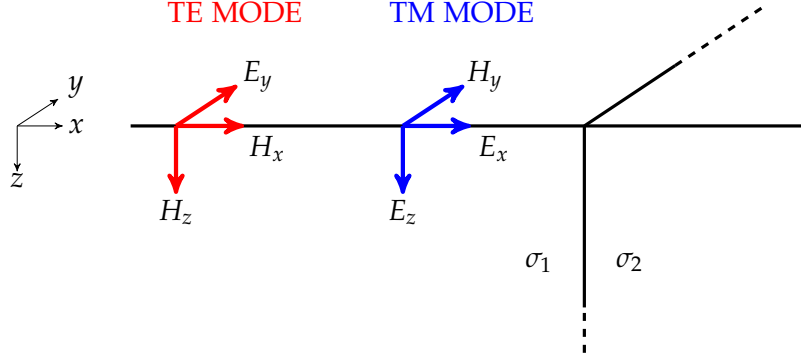


Figure 1.4: Simple 2D conductivity model in which the conductivity is constant along the y direction. Redrawn from Simpson and Bahr [130].

the boundary that separates two materials with different conductivities (equation (1.25)). In Figure 1.4 we have lateral (in x) variation of the conductivity from one material to the next. Thus, from equation (1.25) we know that E_x must be discontinuous across the boundary. In the same way, E_z has to be discontinuous across the air-ground interface. In fact, since the conductivity of the air is close to zero, in order to fulfill the current conservation E_z must be zero at the surface. In the scenario depicted above, the electric and magnetic fields are mutually orthogonal and the EM fields can be decoupled into two modes: the Transverse Electric (TE) mode (or E -Polarization), which corresponds to the polarization that incorporates the electric field parallel to the strike and the induced magnetic fields (E_y, H_x, H_z), and the Transverse Magnetic (TM) mode (or B -Polarization). The latter incorporates the magnetic field parallel to the strike and the induced electric fields, that is, (H_y, E_x, E_z). Both modes are illustrated in Figure 1.4.

The equations for the TE mode are:

$$\left\{ \begin{array}{l} -\nabla \cdot (\mu^{-1} \nabla E_y) - k^2 E_y = -j\omega J_y^{imp}, \\ \frac{\partial}{\partial z} \left(\hat{\sigma}^{-1} \left(\frac{\partial H_z}{\partial x} - \frac{\partial H_x}{\partial z} \right) \right) + j\omega\mu H_x = -\frac{\partial}{\partial z} \left(\hat{\sigma}^{-1} J_y^{imp} \right), \\ \frac{\partial}{\partial x} \left(\hat{\sigma}^{-1} \left(\frac{\partial H_x}{\partial z} - \frac{\partial H_z}{\partial x} \right) \right) + j\omega\mu H_z = \frac{\partial}{\partial x} \left(\hat{\sigma}^{-1} J_y^{imp} \right). \end{array} \right. \quad (1.44)$$

In particular, the scalar equation for E_y characterizes the TE mode. Solving this equation makes possible to recover H_x and H_z from Faraday's Law as:

$$H_x = -\frac{j}{\omega\mu} \left(\frac{\partial E_y}{\partial z} \right), \quad H_z = \frac{j}{\omega\mu} \left(\frac{\partial E_y}{\partial x} \right). \quad (1.45)$$

For the TM mode we have that:

$$\begin{cases} -\nabla \cdot (\hat{\sigma}^{-1} \nabla H_y) + j\omega\mu H_y = -M_y^{imp}, \\ \frac{\partial}{\partial z} \left(\mu^{-1} \left(\frac{\partial E_z}{\partial x} - \frac{\partial E_x}{\partial z} \right) \right) - k^2 E_x = \mu^{-1} \frac{\partial M_y^{imp}}{\partial z}, \\ \frac{\partial}{\partial x} \left(\mu^{-1} \left(\frac{\partial E_x}{\partial z} - \frac{\partial E_z}{\partial x} \right) \right) - k^2 E_z = -\mu^{-1} \frac{\partial M_y^{imp}}{\partial x}. \end{cases} \quad (1.46)$$

Again, the solution for E_x and E_z can be computed from H_y using Ampère's Law:

$$E_x = -\frac{1}{\sigma + j\omega\varepsilon} \left(\frac{\partial H_y}{\partial z} \right), \quad E_z = \frac{1}{\sigma + j\omega\varepsilon} \left(\frac{\partial H_y}{\partial x} \right). \quad (1.47)$$

Even if we focus on isotropic media, it is easy to extend all the results contained in this dissertation to anisotropic media described in equation (1.3). In Appendix 8.1 we show how to uncouple the equations for the TE and TM modes corresponding to this anisotropic media. For such case the fields computed from Maxwell's equations are the same except for E_z , which is computed according to

$$E_z = \frac{1}{\sigma_v + j\omega\varepsilon} \left(\frac{\partial H_y}{\partial x} \right). \quad (1.48)$$

The MT method is typically employed in regions with prior geological knowledge of the media. This enables in practice to align the coordinate system with the medium strike direction. Thus, since the electric and magnetic fields are related only through their orthogonal fields (the diagonal components are zero because they are related to the parallel electric and magnetic fields), the impedance tensor is given by:

$$\mathcal{Z}_{2D} = \begin{pmatrix} 0 & \mathcal{Z}_{xy} \\ \mathcal{Z}_{yx} & 0 \end{pmatrix} = \begin{pmatrix} 0 & \mathcal{Z}_{TM} \\ \mathcal{Z}_{TE} & 0 \end{pmatrix}, \quad (1.49)$$

where \mathcal{Z}_{TE} and \mathcal{Z}_{TM} usually have different magnitudes and opposite sign.

In some cases though, the impedance tensor is not in the electrical strike coordinates. Then, TE and TM modes are mixed in the tensor as in equation (1.26). However, it is possible to recover a 2D impedance tensor where the diagonal components are zero. For this purpose, the measured impedance tensor \mathcal{Z}_{obs} is turned by an angle θ around a vertical axis using Cartesian rotation matrix R_θ (assuming noise-free measurements), so that

$$\mathcal{Z}_{2D} = \mathbf{R} \begin{pmatrix} 0 & \mathcal{Z}_{TM} \\ \mathcal{Z}_{TE} & 0 \end{pmatrix} \mathbf{R}^T = \mathbf{R} \mathcal{Z}_{obs} \mathbf{R}^T, \quad (1.50)$$

where \mathcal{Z}_{obs} is the recorded impedance tensor in the observational reference frame, and

$$\mathbf{R} = \begin{pmatrix} \cos \theta & \sin \theta \\ -\sin \theta & \cos \theta \end{pmatrix}. \quad (1.51)$$

The electric field E_x is discontinuous across the boundary of two different materials, so are the impedances associated to E_x , namely \mathcal{Z}_{xy} and \mathcal{Z}_{xx} (zero in the ideal 2D case), and the apparent resistivity perpendicular to the strike direction. Because of the discontinuity of ρ_{xy} across a vertical boundary, the TM mode tends to resolve lateral resistivity variations better than the TE mode resistivity ρ_{yx} . Nonetheless, since the geomagnetic transfer function is sensitive to lateral conductivity variations, and the involved fields are those associated to the TE mode, it is possible to identify lateral variations also from TE mode. When using the TM mode, resistivities close to the boundary are overestimated when the resistivity is high, and underestimated for low resistivities [157]. This does not occur with the TE mode, which is more stable for estimation of apparent resistivity.

1.3.5 3D Survey

When the source and the materials depend upon the three spatial variables, the problem is 3D. In this case, Maxwell's equations do not have known analytical solution in general. Additionally, no decoupling can be devised and therefore, it is necessary to compute the whole impedance tensor:

$$\mathcal{Z}_{3D} = \begin{pmatrix} \mathcal{Z}_{xx} & \mathcal{Z}_{xy} \\ \mathcal{Z}_{yx} & \mathcal{Z}_{yy} \end{pmatrix}. \quad (1.52)$$

1.4 SUMMARY OF MT ASSUMPTIONS

We summarize here the main assumptions of the MT method (modified from [130]):

- Maxwell's equations are satisfied.
- The Earth does not generate EM energy, but it only absorbs or dissipates it.
- Far from the source, all fields are conservative and analytic, that is, weakly differentiable at all points. Remember that the normal component of the electric field is discontinuous across the boundary of two materials, and therefore it is only weakly differentiable, not differentiable in the classical way.
- The source is a uniform plane-polarized EM wave that has near-vertical angle of incidence to the Earth's surface, and which is generated far from the surface [154]. This assumption may be violated in polar or equatorial regions.

- No accumulation of free charges is sustained in 1D layered Earth. In 2D or 3D Earth models, non-inductive static shift effects can be caused by charges that are accumulated and dissipated along conductivity discontinuities.
- Charges are kept in the Earth ($\frac{\partial \rho}{\partial t} + \nabla \cdot \mathbf{j} = 0$).
- If we consider the maximum value for ε around $100\varepsilon_r$ and the minimal conductivity of 10^{-6} Sm^{-1} (as in [118] for instance), variations in the electric and magnetic permittivities are negligible in front of conductivity variations for frequencies higher than 10^4 Hz. Most MT measurements are performed at lower frequencies, and moreover, larger conductivity values are more likely. Therefore, variations of the electrical permittivity will not strongly impact on the result. The inversion process only makes sense for the conductivity, which is a much more sensitive parameter.
- To reproduce the source of the MT problem (an incident plane wave traveling towards the Earth), we model it as an infinitely long (in y-plane) volumetric rectangular section bar with:

$$\mathbf{J}^{imp} = \left(0, J_y^{imp}, 0 \right), \quad \text{and} \quad \mathbf{M}^{imp} = \left(0, M_y^{imp}, 0 \right). \quad (1.53)$$

VARIATIONAL FORMULATION OF THE FORWARD PROBLEM

In the present Chapter, we derive suitable variational formulations for the FEM MT computations in 3D, 2D, and 1D. We truncate the domain by employing a Perfectly Matched Layer (PML), and we derive a variational formulation that incorporates such absorbing layer and which allows us to compute accurate solutions without introducing spurious numerical reflections. A PML transforms propagating and evanescent waves into exponentially fast decaying evanescent waves inside the layers. We follow the interpretation of Teixeira and Chew [29, 149] for the PML, which consists of considering a change of the variables in the governing equations into the complex plane. Thus, we define this change of variable to be different on each material (or layer) to avoid problems when the materials properties exhibit high contrast between them (a typical scenario in MT). Since waves are strongly attenuated inside the PML region, the bounded computational domain can be limited by a surface on which one can set proper boundary conditions (BCs). Indeed, any reflected wave is so much absorbed inside the layer that it does not pollute the solution in the domain of study. Then, it is possible to consider Dirichlet homogeneous BC, and therefore to set $\hat{n} \times E|_{\Gamma_D} = 0$ for the electric field formulation and $\hat{n} \times H|_{\Gamma_D} = 0$ for the magnetic field formulation. The Dirichlet BC is sometimes represented by using a *lift* which corresponds to an extension of the value of the Dirichlet BC to the whole domain. Since we employ homogeneous BC, we avoid the use of any lift, and for this reason, the variational formulation does not incorporate it.

In this chapter, we also provide the mathematical setting to derive a variational formulation when the goal is to compute secondary field variations. When the subsurface distribution of the resistivity depends upon multiple spatial variables, it is sometimes possible to interpret it as a 1D formation plus some 2D (or 3D) inhomogeneities. In the particular case of a horizontally layered Earth model with higher dimension inhomogeneities, an alternative approach to solve Maxwell's equations consists of splitting the electric and magnetic fields into their primary and secondary components. The first one corresponds to the fields arisen from some reference conductivity model (1D), while the second one arises from the difference between the actual conductivity distribution with respect to the reference model (2D or 3D).

Since the 1D solution is known analytically, the main advantage of this approach is that we only need to accurately solve the secondary field (also known as "scattered field" in the electrical engineering community), which in general is easier to solve, since it exhibits less variations (smaller gradients) than the primary field.

Additionally, in MTs, the computational domains are usually large if one models the incident plane wave source. In the secondary field formulation, the source term is not at the ionosphere, but where the inhomogeneities are considered. Since it is not necessary to model the ionosphere source anymore, this allows us to considerably reduce the size of the computational domain. Finally, since we separate the primary field from the secondary one, we may obtain additional physical relevant information by analyzing each field (primary and secondary) separately.

For the sake of simplicity, and to avoid the technical issues associated to *cohomology spaces* (see e.g. [26]), we restrict ourselves to the case of a bounded and simply connected domain Ω . To derive the variational formulation, we first define the L^2 -inner product of two possible complex and vector valued functions \mathbf{g}_1 and \mathbf{g}_2 as:

$$\langle \mathbf{g}_1, \mathbf{g}_2 \rangle_{L^2(\Omega)} = \int_{\Omega} \mathbf{g}_1^* \mathbf{g}_2 d\Omega, \quad (2.1)$$

where \mathbf{g}^* denotes the adjoint (transpose of the complex conjugate) of \mathbf{g} .

2.1 3D FORMULATION

When the source and materials depend upon the three spatial variables, no uncoupling occurs, and either of the general 3D equations introduced in the previous chapter need to be solved, namely:

$$\nabla \times (\boldsymbol{\mu}^{-1} \nabla \times \mathbf{E}) - \mathbf{k}^2 \mathbf{E} = -j\omega \mathbf{J}^{imp} - \nabla \times (\boldsymbol{\mu}^{-1} \mathbf{M}^{imp}), \quad \text{or} \quad (2.2)$$

$$\nabla \times (\hat{\sigma}^{-1} \nabla \times \mathbf{H}) + j\omega \boldsymbol{\mu} \mathbf{H} = -\mathbf{M}^{imp} + \nabla \times (\hat{\sigma}^{-1} \mathbf{J}^{imp}). \quad (2.3)$$

We assume that the electromagnetic fields are regular enough. To derive the variational formulation of the problem we pre-multiply the adjoint of any vector-valued test function \mathbf{F}^* by equation (2.2), and we integrate by parts over domain Ω . The corresponding variational formulation is then

$$\langle \nabla \times \mathbf{F}, \boldsymbol{\mu}^{-1} \nabla \times \mathbf{E} \rangle_{L^2(\Omega)} - \langle \mathbf{F}, \mathbf{k}^2 \mathbf{E} \rangle_{L^2(\Omega)} = -j\omega \langle \mathbf{F}, \mathbf{J}^{imp} \rangle_{L^2(\Omega)} - \langle \nabla \times \mathbf{F}, \boldsymbol{\mu}^{-1} \mathbf{M}^{imp} \rangle_{L^2(\Omega)}. \quad (2.4)$$

This expression is well defined for any \mathbf{E} and \mathbf{F} in $V(\Omega)$, where $V(\Omega) = H_0(\text{curl}, \Omega) = \{\mathbf{F} \in L^2(\Omega) : \hat{\mathbf{n}} \times \mathbf{F}|_{\Gamma_D} = 0, \nabla \times \mathbf{F} \in L^2(\Omega)\}$. In a similar way, from (2.3) a variational formulation for the magnetic reads as:

$$\langle \nabla \times \mathbf{F}, \hat{\sigma}^{-1} \nabla \times \mathbf{H} \rangle_{L^2(\Omega)} + j\omega \langle \mathbf{F}, \boldsymbol{\mu} \mathbf{H} \rangle_{L^2(\Omega)} = -\langle \mathbf{F}, \mathbf{M}^{imp} \rangle_{L^2(\Omega)} + \langle \nabla \times \mathbf{F}, \hat{\sigma}^{-1} \mathbf{J}^{imp} \rangle_{L^2(\Omega)}. \quad (2.5)$$

By defining $V(\Omega) = H_0(\mathbf{curl}, \Omega)$ we guarantee the integrability of all expressions above, while we ensure a sufficiently enriched spaces to guarantee that the solution of the variational problem coincides with that of the original boundary value problem.

2.2 2D FORMULATION

When the materials and source depend only upon the two spatial variables (x, z) , then two independent and uncoupled modes are derived from Maxwell's equations. The uncoupled TE mode involves (E_y, H_x, H_z) field components, while TM only considers (H_y, E_x, E_z) (see section 1.3.4).

While the y component of the electric and magnetic fields satisfy scalar equations, the remaining field components satisfy coupled vectorial equations (equations (1.44) and (1.46)). The scalar equations are often much easier to solve numerically. Moreover, once they are computed, the rest of the fields can be obtained via postprocessing. Therefore, we derive suitable variational formulations for the FEM for the fields E_y and H_y .

To obtain a variational formulation for the electric and magnetic fields, we proceed exactly as previously. For the electric field, we multiply the first equation of (1.44) by the adjoint of any scalar function F , while for the magnetic field we employ the first equation of (2.3). Then, the two variational formulations are given by:

$$\langle \nabla F, \mu^{-1} \nabla E_y \rangle_{L^2(\Omega)} - \langle F, k^2 E_y \rangle_{L^2(\Omega)} = -j\omega \langle F, J_y^{imp} \rangle_{L^2(\Omega)}, \quad (2.6)$$

and

$$\langle \nabla F, \hat{\sigma}^{-1} \nabla H_y \rangle_{L^2(\Omega)} + j\omega \langle F, \mu H_y \rangle_{L^2(\Omega)} = -\langle F, M_y^{imp} \rangle_{L^2(\Omega)}. \quad (2.7)$$

These expressions are well defined for E_y, H_y and F in $V(\Omega)$, where $V(\Omega) = H_0^1(\Omega) = \{F \in L^2(\Omega) : F|_{\Gamma_D} = 0, \nabla F \in L^2(\Omega)\}$. Additionally, this definitions also guarantee that the space is sufficiently enrich so that the solution to the variational formulation is equivalent to the solution to the boundary value problem.

2.3 1D FORMULATION

In this scenario, the materials and source only depend upon one spatial variable z . The variational formulations are analogous than for the 2D case, but we explicitly derive them since they will be employed for obtaining various numerical results. The variational formulation for the electric field is given by:

$$\langle \nabla F, \mu^{-1} \nabla E_y \rangle_{L^2(\Omega)} - \langle F, k^2 E_y \rangle_{L^2(\Omega)} = -j\omega \langle F, J_y^{imp} \rangle_{L^2(\Omega)}, \quad (2.8)$$

and for the magnetic field by:

$$\langle \nabla F, \hat{\sigma}^{-1} \nabla H_y \rangle_{L^2(\Omega)} + j\omega \langle F, \mu H_y \rangle_{L^2(\Omega)} = -\langle F, M_y^{imp} \rangle_{L^2(\Omega)}. \quad (2.9)$$

These expressions are well defined for E_y, H_y and F in $V(\Omega)$, where $V(\Omega) = H_0^1(\Omega) = \{F \in L^2(\Omega) : F|_{\Gamma_D} = 0, \nabla F \in L^2(\Omega)\}$. This definition also provides sufficiently enriched spaces to guarantee that the solution of the variational problem coincides with that of the original boundary value problem.

2.4 TRUNCATION OF THE DOMAIN

When applying a FEM to unbounded region problems such as MT, the computational domain must be truncated. Different approaches can be employed for this purpose. We use a PML, which maintains unchanged the continuous solution inside the region of interest. This enables to match the high-accuracy level delivered by the hp -adaptive FEM. The work of Gomez-Revuelto et al. [49] demonstrates the suitability of the utilization of PMLs in the context of hp -FEM computations.

2.4.1 Perfectly Matched Layers

In 1994, in a seminal paper of Berenger [17], PMLs were proposed in an electromagnetic context as an artificial layer intended to reduce reflections from the boundary of a truncated computational domain. This pioneering work was justified by arguments from physics. To help providing a mathematical setting of PMLs, a new interpretation was introduced later on by Teixeira and Chew [29, 149], which allowed to interpret a PML as an analytic continuation of the governing equations into the complex plane (see also [148]).

In this method, one has to *select* the decay profile of the wave into the PML region. This profile needs to ensure that reflections from the boundary are arbitrarily small, which implies that the solution decays arbitrarily fast, creating then a *boundary layer* with strong gradients within the PML region. Thus, while a low decay produces incoming waves reflected from the boundary, an excessive decay requires a very fine grid to approximate the boundary layer. To find an equilibrium between a fast and a slow decay, it is necessary to properly adjust the PML parameters, which is usually tricky since they depend on the problem itself. Moreover, when we have a layered material with high contrasts on the material properties, this selection of the parameters is even more challenging. For a further understanding and for a recent review of the state of the art of this truncation technique, see for instance [18, 66].

In here, we provide a method to automatically adjust the PML parameters, even in the most complex scenarios where the material contrast properties among neighboring materials might be as high as sixteen orders of magnitude. These types of scenarios often appear in geophysical EM applications that involve both air and ground. Our aim is to obtain an appropriate decay of the solution in the air and in the subsurface without introducing spurious reflections, and thus, providing accurate solutions.

Following Chew and Weedon's interpretation [29], we introduce a general change of coordinates, and we derive a variational formulation under an arbitrary system of coordinates.

2.4.2 PML Definition

Let the Cartesian coordinate system $x = (x, y, z)$ be the reference system of coordinates in a 3D scenario, where for simplicity we select the vertical coordinate z as the direction perpendicular to the ground-air interface. Given an arbitrary complex system of coordinates $\zeta = (\zeta_1, \zeta_2, \zeta_3)$, we define our change of coordinates by $x = \psi(\zeta)$ and we denote the Jacobian matrix and its determinant by \mathcal{J} and $\det(\mathcal{J})$. The change of coordinates is assumed to be represented by an injective differentiable function with continuous partial derivatives and nonzero determinant at any point.

We define a one dimensional change of variables in the positive direction of the i -th coordinate as

$$\zeta_i(x_i) = \int_0^{x_i} Y(x') dx', \quad \text{for } i = 1, 2, 3, \quad x_1 = x, \quad x_2 = y, \quad x_3 = z, \quad (2.10)$$

where $Y(\cdot)$ is a possibly complex valued function to be determined in section 2.4.4. The case corresponding to the negative direction can be defined analogously. The Jacobian is defined as usual by $[\mathcal{J}]_{ij} = \left[\frac{\partial \zeta_i}{\partial x_j} \right]_{ij}$, for $i, j = 1, 2$, or 3 ,

$$\mathcal{J}_{3D} = \begin{pmatrix} Y(x) & 0 & 0 \\ 0 & Y(y) & 0 \\ 0 & 0 & Y(z) \end{pmatrix}, \quad \mathcal{J}_{2D} = \begin{pmatrix} Y(x) & 0 \\ 0 & Y(z) \end{pmatrix}, \quad \mathcal{J}_{1D} = Y(z), \quad (2.11)$$

and its determinant is given for each dimension by

$$\det(\mathcal{J}_{3D}) = Y(x)Y(y)Y(z), \quad \det(\mathcal{J}_{2D}) = Y(x)Y(z), \quad \det(\mathcal{J}_{1D}) = Y(z). \quad (2.12)$$

With this particular change of coordinates, the Jacobian is diagonal. However, we derive herein the variational formulation for a general, non orthogonal change of variables. This may be useful for other purposes, e.g. development of non-orthogonal Fourier FEMs in certain geometries (see [113, 106]).

2.4.3 Variational Formulation in an Arbitrary System of Coordinates

3D Model

Let \hat{e}_{x_i} and \hat{e}_{ζ_i} be the basis vectors corresponding to the Cartesian and new system of coordinates, respectively. We define the change of coordinates $\hat{E} := E \circ \boldsymbol{\psi} = \hat{E}(\boldsymbol{\zeta})$, $\hat{F} := F \circ \boldsymbol{\psi} = \hat{F}(\boldsymbol{\zeta})$, and $\hat{J}^{imp} := J^{imp} \circ \boldsymbol{\psi} = \hat{J}^{imp}(\boldsymbol{\zeta})$. Using Einstein's summation convention, $E = E_{x_i} \hat{e}_{x_i}$ and $\hat{E} = \tilde{E}_{\zeta_i} \hat{e}_{\zeta_i}$, where (see for instance [113]),

$$\tilde{E}_{\zeta_i} = E_{x_l} \frac{\partial x_l}{\partial \zeta_i}. \quad (2.13)$$

Defining $\tilde{E} := \tilde{E}_{\zeta_i} \hat{e}_{x_i}$, $\tilde{F} := \tilde{F}_{\zeta_i} \hat{e}_{x_i}$, and $\tilde{J}^{imp} := \tilde{J}_{\zeta_i}^{imp} \hat{e}_{x_i}$, and taking into account that if $f \in C^1(\Omega)$, then for all i

$$\frac{\partial \bar{f}}{\partial \zeta_i} = \frac{\partial \bar{f}}{\partial \bar{\zeta}_i}, \quad \frac{\partial \bar{f}}{\partial \bar{\zeta}_i} = \frac{\partial \bar{f}}{\partial \zeta_i}, \quad (2.14)$$

stands, we have then that

$$\begin{aligned} \tilde{E} &= \tilde{E}_{\zeta_i} \hat{e}_{x_i} = E_{x_l} \frac{\partial x_l}{\partial \zeta_i} \hat{e}_{x_i} = (\mathcal{J}_{3D}^{-1})^T E, \\ \nabla^{\zeta} \times \tilde{E} &= \epsilon_{ijk} \frac{\partial \tilde{E}_{\zeta_k}}{\partial \zeta_j} \hat{e}_{x_i} = \frac{1}{\det(\mathcal{J}_{3D})} \frac{\partial \zeta_i}{\partial x_n} \left(\epsilon_{nml} \frac{\partial E_{x_l}}{\partial x_m} \right) \hat{e}_{x_i} = \frac{1}{\det(\mathcal{J}_{3D})} \mathcal{J}_{3D} \nabla \times E, \\ \nabla^{\bar{\zeta}} \times \tilde{E} &= \epsilon_{ijk} \frac{\partial \tilde{E}_{\zeta_k}}{\partial \bar{\zeta}_j} \hat{e}_{x_i} = \frac{1}{\det(\overline{\mathcal{J}_{3D}})} \frac{\partial \bar{\zeta}_i}{\partial x_n} \left(\epsilon_{nml} \frac{\partial E_{x_l}}{\partial x_m} \right) \hat{e}_{x_i} = \frac{1}{\det(\overline{\mathcal{J}_{3D}})} \overline{\mathcal{J}_{3D}} \nabla \times E, \end{aligned} \quad (2.15)$$

where ϵ_{ijk} is the so called Levi-Civita symbol, defined as 1 if $\{n, m, l\}$ is an even permutation of $\{1, 2, 3\}$, -1 if $\{n, m, l\}$ is an odd permutation of $\{1, 2, 3\}$, and 0 if $n = m$, or $n = l$, or $m = l$.

Then, we have that:

$$\begin{aligned} \langle \nabla^{\bar{\zeta}} \times \tilde{F}, \tilde{\boldsymbol{\mu}}^{-1} \nabla^{\zeta} \times \tilde{E} \rangle_{L^2(\tilde{\Omega})} &= \left\langle \frac{1}{\det(\overline{\mathcal{J}_{3D}})} \overline{\mathcal{J}_{3D}} \nabla \times F, \boldsymbol{\mu}^{-1} \frac{1}{\det(\mathcal{J}_{3D})} \mathcal{J}_{3D} \nabla \times E \det(\mathcal{J}_{3D}) \right\rangle_{L^2(\Omega)} = \\ &= \left\langle \nabla \times F, (\mathcal{J}_{3D})^T \boldsymbol{\mu}^{-1} \mathcal{J}_{3D} \nabla \times E \frac{1}{\det(\mathcal{J}_{3D})} \right\rangle_{L^2(\Omega)}, \\ \langle \tilde{F}, \tilde{\mathbf{k}}^2 \tilde{E} \rangle_{L^2(\tilde{\Omega})} &= \left\langle (\mathcal{J}_{3D}^{-1})^T F, \mathbf{k}^2 (\mathcal{J}_{3D}^{-1})^T E \det(\mathcal{J}_{3D}) \right\rangle_{L^2(\Omega)} = \\ &= \left\langle F, \overline{\mathcal{J}_{3D}}^{-1} \mathbf{k}^2 (\mathcal{J}_{3D}^{-1})^T E \det(\mathcal{J}_{3D}) \right\rangle_{L^2(\Omega)}, \end{aligned} \quad (2.16)$$

$$\begin{aligned}
\langle \tilde{\mathbf{F}}, \tilde{\mathbf{J}}^{imp} \rangle_{L^2(\tilde{\Omega})} &= \langle (\mathcal{J}_{3D}^{-1})^T \mathbf{F}, (\mathcal{J}_{3D}^{-1})^T \mathbf{J}^{imp} \det(\mathcal{J}_{3D}) \rangle_{L^2(\Omega)} = \\
&= \langle \mathbf{F}, \overline{\mathcal{J}_{3D}^{-1}} (\mathcal{J}_{3D}^{-1})^T \mathbf{J}^{imp} \det(\mathcal{J}_{3D}) \rangle_{L^2(\Omega)}, \\
\langle \nabla^{\bar{\zeta}} \times \tilde{\mathbf{F}}, \tilde{\boldsymbol{\mu}}^{-1} \tilde{\mathbf{M}}^{imp} \rangle_{L^2(\tilde{\Omega})} &= \left\langle \frac{1}{\det(\overline{\mathcal{J}_{3D}})} \overline{\mathcal{J}_{3D}} \nabla \times \mathbf{F}, \boldsymbol{\mu}^{-1} (\mathcal{J}_{3D}^{-1})^T \mathbf{M}^{imp} \det(\mathcal{J}_{3D}) \right\rangle_{L^2(\Omega)} = \\
&= \langle \nabla \times \mathbf{F}, (\mathcal{J}_{3D})^T \boldsymbol{\mu}^{-1} (\mathcal{J}_{3D}^{-1})^T \mathbf{M}^{imp} \rangle_{L^2(\Omega)},
\end{aligned} \tag{2.17}$$

where $\tilde{\boldsymbol{\mu}} := \boldsymbol{\mu} \circ \boldsymbol{\psi}$, $\tilde{\mathbf{k}} := \mathbf{k} \circ \boldsymbol{\psi}$, $\tilde{\Omega} := \Omega \circ \boldsymbol{\psi}$, and $\tilde{\Gamma}_D := \Gamma_D \circ \boldsymbol{\psi}$. We remark that, since the change of variables is to the complex plane, and since the derivative is with respect a complex variable, the double curl term of the variational formulation is given by

$$\langle \nabla^{\bar{\zeta}} \times \tilde{\mathbf{F}}, \tilde{\boldsymbol{\mu}}^{-1} \nabla^{\bar{\zeta}} \times \tilde{\mathbf{E}} \rangle_{L^2(\tilde{\Omega})}, \tag{2.18}$$

where the derivative is with respect to $\bar{\zeta}$ instead of ζ (see Appendix 8.2).

Following the ideas of [162] regarding the inclusion of metric-dependent variables within material coefficients, we define the following new quantities for the case of a PML:

$$\begin{aligned}
\boldsymbol{\mu}_{NEW}^E &= \mathcal{J}_{3D}^{-1} \boldsymbol{\mu} (\mathcal{J}_{3D}^{-1})^T \det(\mathcal{J}_{3D}) = \begin{pmatrix} \mu \frac{Y(y)Y(z)}{Y(x)} & 0 & 0 \\ 0 & \mu \frac{Y(x)Y(z)}{Y(y)} & 0 \\ 0 & 0 & \mu \frac{Y(x)Y(y)}{Y(z)} \end{pmatrix}, \\
\mathbf{k}_{NEW}^2 &= \overline{\mathcal{J}_{3D}^{-1}} \mathbf{k}^2 (\mathcal{J}_{3D}^{-1})^T \det(\mathcal{J}_{3D}) = \begin{pmatrix} k \frac{Y(y)Y(z)}{Y(x)} & 0 & 0 \\ 0 & k \frac{Y(x)Y(z)}{Y(y)} & 0 \\ 0 & 0 & k \frac{Y(x)Y(y)}{Y(z)} \end{pmatrix},
\end{aligned} \tag{2.19}$$

$$\begin{aligned}
\mathbf{J}_{NEW}^{imp} &= \overline{\mathcal{J}_{3D}^{-1}} (\mathcal{J}_{3D}^{-1})^T \mathbf{J}^{imp} \det(\mathcal{J}_{3D}) = \left(0, J_y^{imp} \frac{Y(x)Y(z)}{Y(y)}, 0 \right)^T, \\
\mathbf{M}_{NEW}^{imp} &= (\mathcal{J}_{3D})^T (\mathcal{J}_{3D}^{-1})^T \mathbf{M}^{imp} = \left(0, M_y^{imp}, 0 \right)^T.
\end{aligned} \tag{2.20}$$

A similar approach for the magnetic field yields to the following coefficients:

$$\begin{aligned} \hat{\sigma}_{NEW} &= \mathcal{J}_{3D}^{-1} \hat{\sigma} (\mathcal{J}_{3D}^{-1})^T \det(\mathcal{J}_{3D}) = \begin{pmatrix} \hat{\sigma} \frac{Y(y)Y(z)}{Y(x)} & 0 & 0 \\ 0 & \hat{\sigma} \frac{Y(x)Y(z)}{Y(y)} & 0 \\ 0 & 0 & \hat{\sigma} \frac{Y(x)Y(y)}{Y(z)} \end{pmatrix}, \\ \mu_{NEW}^H &= \overline{\mathcal{J}_{3D}}^{-1} \mu (\mathcal{J}_{3D}^{-1})^T \det(\mathcal{J}_{3D}) = \begin{pmatrix} \mu \frac{Y(y)Y(z)}{Y(x)} & 0 & 0 \\ 0 & \mu \frac{Y(x)Y(z)}{Y(y)} & 0 \\ 0 & 0 & \mu \frac{Y(x)Y(y)}{Y(z)} \end{pmatrix}, \end{aligned} \quad (2.21)$$

$$\begin{aligned} \mathbf{J}_{NEW}^{imp,H} &= (\mathcal{J}_{3D})^T (\mathcal{J}_{3D}^{-1})^T \mathbf{J}^{imp} = \left(0, J_y^{imp}, 0 \right)^T, \\ \mathbf{M}_{NEW}^{imp,H} &= \overline{\mathcal{J}_{3D}}^{-1} (\mathcal{J}_{3D}^{-1})^T \mathbf{M}^{imp} \det(\mathcal{J}_{3D}) = \left(0, M_y^{imp} \frac{Y(x)Y(z)}{Y(y)}, 0 \right)^T. \end{aligned} \quad (2.22)$$

The new variational formulation in the new system of coordinates for the electric field reads as:

$$\begin{aligned} \langle \nabla \times \mathbf{F}, (\mu_{NEW}^E)^{-1} \nabla \times \mathbf{E} \rangle_{L^2(\Omega)} - \langle \mathbf{F}, \mathbf{k}_{NEW}^2 \mathbf{E} \rangle_{L^2(\Omega)} = \\ -j\omega \langle \mathbf{F}, \mathbf{J}_{NEW}^{imp} \rangle_{L^2(\Omega)} - \langle \nabla \times \mathbf{F}, \mu_{NEW}^{-1} \mathbf{M}_{NEW}^{imp} \rangle_{L^2(\Omega)}, \end{aligned} \quad (2.23)$$

while for the magnetic field, we have:

$$\begin{aligned} \langle \nabla \times \mathbf{F}, \hat{\sigma}_{NEW}^{-1} \nabla \times \mathbf{H} \rangle_{L^2(\Omega)} + j\omega \langle \mathbf{F}, \mu_{NEW}^H \mathbf{H} \rangle_{L^2(\Omega)} = \\ -\langle \mathbf{F}, \mathbf{M}_{NEW}^{imp,H} \rangle_{L^2(\Omega)} + \langle \nabla \times \mathbf{F}, \hat{\sigma}_{NEW}^{-1} \mathbf{J}_{NEW}^{imp,H} \rangle_{L^2(\Omega)}, \end{aligned} \quad (2.24)$$

where $\tilde{V}(\mathit{curl}, \Omega) = \{ \mathcal{J}_{3D}^{-1} \mathbf{F} \in \mathbf{L}^2(\Omega) : (\mathbf{n} \times \mathbf{F})|_{\Gamma_D} = 0, \frac{1}{\det(\mathcal{J}_{3D})} \mathcal{J}_{3D} \nabla \times \mathbf{F} \in \mathbf{L}^2(\Omega) \}$.

2D Model

We define the change of coordinates $\tilde{E}_y := E_y \circ \psi = \tilde{E}_y(\zeta)$, $\tilde{F} := F \circ \psi = \tilde{F}(\zeta)$, and $\tilde{J}^{imp} := J^{imp} \circ \psi = J^{imp}(\zeta)$, where now $\mathbf{x} = (x, z)$ and $\zeta = (\zeta_1, \zeta_2)$. Using Einstein's summation

convention, according to the chain rule, and taking into account equation (2.14) we obtain that

$$\begin{aligned}\nabla^{\zeta} \tilde{E}_y &= \frac{\partial \tilde{E}_y}{\partial x_i} \frac{\partial x_i}{\partial \zeta_n} \mathbf{e}_{x_n} = (\mathcal{J}_{2D}^{-1})^T \nabla E_y, \\ \nabla^{\bar{\zeta}} \tilde{E}_y &= \frac{\partial \tilde{E}_y}{\partial x_i} \frac{\partial x_i}{\partial \bar{\zeta}_n} \mathbf{e}_{x_n} = (\mathcal{J}_{2D}^{-1})^* \nabla E_y.\end{aligned}\tag{2.25}$$

Thus, we obtain that:

$$\begin{aligned}\langle \nabla^{\bar{\zeta}} \tilde{F}, \tilde{\mu}^{-1} \nabla^{\zeta} \tilde{E}_y \rangle_{L^2(\tilde{\Omega})} &= \langle (\mathcal{J}_{2D}^{-1})^* \nabla F, \mu^{-1} (\mathcal{J}_{2D}^{-1})^T \nabla E_y \det(\mathcal{J}_{2D}) \rangle_{L^2(\Omega)} = \\ &= \langle \nabla F, \mathcal{J}_{2D}^{-1} \mu^{-1} (\mathcal{J}_{2D}^{-1})^T \nabla E_y \det(\mathcal{J}_{2D}) \rangle_{L^2(\Omega)}, \\ \langle \tilde{F}, \tilde{k}^2 \tilde{E}_y \rangle_{L^2(\tilde{\Omega})} &= \langle F, k^2 E_y \det(\mathcal{J}_{2D}) \rangle_{L^2(\Omega)}, \\ \langle \tilde{F}, \tilde{J}^{imp} \rangle_{L^2(\tilde{\Omega})} &= \langle F, J^{imp} \det(\mathcal{J}_{2D}) \rangle_{L^2(\Omega)},\end{aligned}\tag{2.26}$$

where $\tilde{\mu} := \mu \circ \psi$ and $\tilde{k} := k \circ \psi$. Again, we remark that, since the change of variables is to the complex plane, and since the derivative is with respect a complex variable the variational formulation is effectively given by

$$\langle \nabla^{\bar{\zeta}} \tilde{F}, \tilde{\mu}^{-1} \nabla^{\zeta} \tilde{E}_y \rangle_{L^2(\tilde{\Omega})},\tag{2.27}$$

where the derivative is with respect to the complex conjugate of ζ (see Appendix 8.2).

Following the ideas of [162] concerning the inclusion of metric-dependent variables within material coefficients, we define the following functions for the TE Mode:

$$\begin{aligned}\mu_{NEW}^E &= (\mathcal{J}_{2D})^T \mu \mathcal{J}_{2D} \frac{1}{\det(\mathcal{J}_{2D})} = \begin{pmatrix} \mu \frac{Y(x)}{Y(z)} & 0 \\ 0 & \mu \frac{Y(z)}{Y(x)} \end{pmatrix}, \\ k_{NEW}^2 &= k^2 \det(\mathcal{J}_{2D}) = k^2 Y(x) Y(z), \\ J_{NEW}^{imp} &= J^{imp} \det(\mathcal{J}_{2D}) = J^{imp} Y(x) Y(z).\end{aligned}\tag{2.28}$$

Similarly, for the TM mode we have that:

$$\begin{aligned}\hat{\sigma}_{NEW} &= (\mathcal{J}_{2D})^T \hat{\sigma} \mathcal{J}_{2D} \frac{1}{\det(\mathcal{J}_{2D})} = \begin{pmatrix} \hat{\sigma} \frac{Y(x)}{Y(z)} & 0 \\ 0 & \hat{\sigma} \frac{Y(z)}{Y(x)} \end{pmatrix}, \\ \mu_{NEW}^H &= \mu \det(\mathcal{J}_{2D}) = \mu Y(x) Y(z), \\ M_{NEW}^{imp} &= M^{imp} \det(\mathcal{J}_{2D}) = M^{imp} Y(x) Y(z).\end{aligned}\tag{2.29}$$

The new variational formulation for the electric field in the new system of coordinates is then given by

$$\langle \nabla F, (\mu_{NEW}^E)^{-1} \nabla E_y \rangle_{L^2(\Omega)} - \langle F, k_{NEW}^2 E_y \rangle_{L^2(\Omega)} = -j\omega \langle F, J_{NEW}^{imp} \rangle_{L^2(\Omega)}, \quad (2.30)$$

and for the magnetic field

$$\langle \nabla F, \hat{\sigma}_{NEW}^{-1} \nabla H_y \rangle_{L^2(\Omega)} + j\omega \langle F, \mu_{NEW}^H H_y \rangle_{L^2(\Omega)} = -\langle F, M_{NEW}^{imp} \rangle_{L^2(\Omega)}, \quad (2.31)$$

where $\tilde{V}(\Omega) = \{F \in L^2(\Omega) : F|_{\Gamma_D} = 0, (\mathcal{J}_{2D}^{-1})^T \nabla F \in L^2(\Omega)\}$ in both cases.

1D Model

For the 1D case, $x = x$ and $\zeta = \zeta_1$ and the new material parameters for the electric field are then given by:

$$\begin{aligned} \mu_{NEW}^E &= (\mathcal{J}_{1D})^T \mu \mathcal{J}_{1D} \frac{1}{\det(\mathcal{J}_{1D})} = \mu Y(z) \\ k_{NEW}^2 &= k^2 \det(\mathcal{J}_{1D}) = k^2 Y(z), \\ J_{NEW}^{imp} &= J^{imp} \det(\mathcal{J}_{1D}) = J^{imp} Y(z), \end{aligned} \quad (2.32)$$

while for the magnetic field:

$$\begin{aligned} \hat{\sigma}_{NEW} &= (\mathcal{J}_{1D})^T \hat{\sigma} \mathcal{J}_{1D} \frac{1}{\det(\mathcal{J}_{1D})} = \hat{\sigma} Y(z) \\ \mu_{NEW}^H &= \mu \det(\mathcal{J}_{1D}) = \mu Y(z), \\ M_{NEW}^{imp} &= M^{imp} \det(\mathcal{J}_{1D}) = M^{imp} Y(z). \end{aligned} \quad (2.33)$$

The new variational formulations for the electric field in the new system of coordinates are then given by:

$$\langle \nabla F, (\mu_{NEW}^E)^{-1} \nabla E_y \rangle_{L^2(\Omega)} - \langle F, k_{NEW}^2 E_y \rangle_{L^2(\Omega)} = -j\omega \langle F, J_{NEW}^{imp} \rangle_{L^2(\Omega)}, \quad (2.34)$$

and for the magnetic field we have that:

$$\langle \nabla F, \hat{\sigma}_{NEW}^{-1} \nabla H_y \rangle_{L^2(\Omega)} + j\omega \langle F, \mu_{NEW}^H H_y \rangle_{L^2(\Omega)} = -\langle F, M_{NEW}^{imp} \rangle_{L^2(\Omega)}, \quad (2.35)$$

where $\tilde{V}(\Omega) = \{F \in L^2(\Omega) : F|_{\Gamma_D} = 0, (\mathcal{J}_{1D}^{-1})^T \nabla F \in L^2(\Omega)\}$.

The resulting formulations (2.23), (2.24), (2.30), (2.31), (2.34), and (2.35) are again governed by Maxwell's equations (with possibly anisotropic material properties). Because of that, all known convergence and stability properties of Maxwell's equations still hold on the new system of coordinates. In particular, for proving convergence and stability of a PML interpreted as a change of coordinates, it is sufficient to show that the resulting waves decay sufficiently fast within the PML region, which amounts to select a proper

decay function as a change of coordinates within PML [29, 149]. Notice that in linear elasticity, proving stability of PML is a much more challenging issue (see, for instance, [86]), because a change of coordinates produces the appearance of Christoffel symbols leading to a system of equations that is no longer governed by linear elasticity.

2.4.4 Automatic Adjustment of PML Parameters

Given the general change of coordinates (2.10), we select

$$Y(x_i) = \begin{cases} 1, & x_i < x_i^a, \\ \beta_i \in \mathbb{C}, & x_i \in [x_i^a, x_i^b], \end{cases} \quad (2.36)$$

where $[x_i^a, x_i^b]$ defines the position of the PML in the positive direction of the i -th coordinate.

Far away from the source, the solution can be assumed to be a sum of plane waves. Thus, it may be decomposed into functions of the form $e^{-j\gamma x \cdot v}$ (see [65]), where $\gamma = \sqrt{\omega^2 \mu \epsilon - j\omega \mu \sigma}$ is the wavenumber and v is a unit vector that indicates the direction of propagation of the wave.

When implementing a PML, one has to *select* the decay profile of the wave into the PML region, which is usually a tricky task due to the dependence on the problem itself. To find an equilibrium between a fast and a slow decay, it is necessary to properly adjust the PML parameters. Moreover, for layered formations with highly contrasted material properties, this selection of the parameters is even more challenging.

We consider the scenario in which the wave travels the shortest distance, that is, a plane wave traveling perpendicularly to the PML in the x_i variable towards the end of the computational domain. Then, the solution in the PML region, in the positive direction of x_i , for the new variable is given by (an analogous analysis can be performed for the negative direction):

$$E(\zeta(x_i)) = e^{-j\gamma\zeta(x_i)} = e^{-j\gamma\beta_i x_i}. \quad (2.37)$$

We aim at making the solution to diminish within the PML region without introducing reflections. Therefore, we define the decay factor $\alpha < 1$, which measures the decay of the solution from x_i^a to x_i^b , as

$$\alpha := \frac{E(x_i^b)}{E(x_i^a)} = e^{-j\gamma\beta_i(x_i^b - x_i^a)}. \quad (2.38)$$

Then, we have

$$\beta_i = j \frac{\log(\alpha)}{\gamma(x_i^b - x_i^a)}. \quad (2.39)$$

Remark. The above formula gives us an Automatically Adapted PML. It adjusts the parameters without further user interaction, even if the material properties change abruptly. This is especially important for our MT application, since we have layers with highly varying conductivities. The most prominent example of this occurs on the air-Earth inter-

face. The only user interaction is to define the desired decay into the PML region, i.e., α . Then, β_i is automatically computed guaranteeing a specific decay in the PML according to the selected α .

2.5 SECONDARY FIELD FORMULATION

We consider the reference (primary) conductivity model as a 1D layered medium with a known analytical solution (see section 3.1), and we denote it by σ^P . Let Ω_S be the domain where the higher dimensional inhomogeneities are located while Ω_P corresponds to the remaining part. Defining $\sigma^S = \sigma - \sigma^P$, then σ^S is equal to zero outside Ω_S . If we denote the solution to the primary field by (E^P, H^P) , then the secondary field (E^S, H^S) is defined as the difference between the total and the primary fields as:

$$E^S = E - E^P, \quad H^S = H - H^P. \quad (2.40)$$

Then, the governing equations (2.2) and (2.3) for the electric fields become:

$$\nabla \times \left(\boldsymbol{\mu}^{-1} \nabla \times E^S \right) - k^2 E^S = -j\omega \sigma^S E^P, \quad (2.41)$$

$$\nabla \times \left(\hat{\sigma}^{-1} \nabla \times H^S \right) + j\omega \boldsymbol{\mu} H^S = -\nabla \times \left(\tilde{\sigma}^{-1} \nabla \times H^P \right), \quad (2.42)$$

where $\tilde{\sigma}^{-1} = \hat{\sigma}^{-1} - (\hat{\sigma}^P)^{-1}$. These equations yield a similar weak formulation to the one derived in Section 2.4.3. The only significant modification occurs on the right hand side. This implies that after incorporating the PML, the new materials are also computed in the same way.

2.5.1 3D Model

In a 3D model for the Earth formation, it is possible to consider the reference conductive model as a 2D Earth (a 1D Earth is also possible). This scenario with the two domains Ω_P and Ω_S is illustrated in Figure 2.1. The new variational formulation for the electric field reads as:

$$\langle \nabla \times F, (\boldsymbol{\mu}_{NEW}^E)^{-1} \nabla \times E^S \rangle_{L^2(\Omega)} - \langle F, \mathbf{k}_{NEW}^2 E^S \rangle_{L^2(\Omega)} = -j\omega \langle F, \sigma_{NEW}^S E^P \rangle_{L^2(\Omega)}, \quad (2.43)$$

and for the magnetic field:

$$\langle \nabla \times F, \hat{\sigma}_{NEW}^{-1} \nabla \times H^S \rangle_{L^2(\Omega)} + j\omega \langle F, \boldsymbol{\mu}_{NEW}^H H^S \rangle_{L^2(\Omega)} = -\langle \nabla \times F, \tilde{\sigma}_{NEW}^{-1} \nabla \times H^P \rangle_{L^2(\Omega)}, \quad (2.44)$$

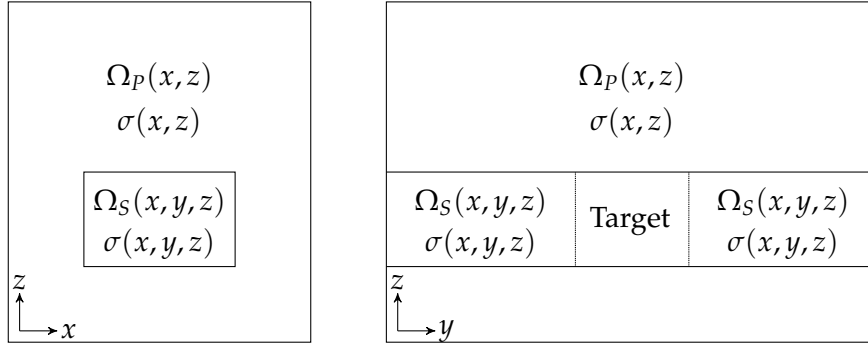


Figure 2.1: Illustration of the computational subdomains Ω_P and Ω_S and the material properties inside each subdomain. Left: x - z section. Right: y - z section.

where $\tilde{\sigma}_{NEW}$ is then given by

$$\tilde{\sigma}_{NEW} = \begin{pmatrix} \tilde{\sigma} \frac{Y(y)Y(z)}{Y(x)} & 0 & 0 \\ 0 & \tilde{\sigma} \frac{Y(x)Y(z)}{Y(y)} & 0 \\ 0 & 0 & \tilde{\sigma} \frac{Y(x)Y(y)}{Y(z)} \end{pmatrix}. \quad (2.45)$$

In both cases, these expressions are well defined for any E and F in $V(\Omega)$, where $F \in \tilde{V}(\mathit{curl}, \Omega) = \{ \mathcal{J}_{3D}^{-1} F \in L^2(\Omega) : (\mathbf{n} \times F)|_{\Gamma_D} = 0, \frac{1}{\det(\mathcal{J}_{3D})} \mathcal{J}_{3D} \nabla \times F \in L^2(\Omega) \}$.

2.5.2 2D Model

For a 2D Earth model we select a reference conductivity model that corresponds to a 1D problem. We illustrate this scenario in Figure 2.2. The variational formulation for the

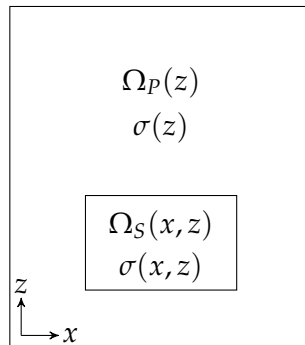


Figure 2.2: Illustration of the computational subdomains Ω_P and Ω_S and the material properties inside each subdomain. σ only depends on z in Ω_P , and on x and z in Ω_S .

electric field is given by

$$\langle \nabla F, (\boldsymbol{\mu}_{NEW}^E)^{-1} \nabla E_y^S \rangle_{L^2(\Omega)} - \langle F, k_{NEW}^2 E_y^S \rangle_{L^2(\Omega)} = -j\omega \langle F, \sigma_{NEW}^S E_y^P \rangle_{L^2(\Omega)}, \quad (2.46)$$

while for the magnetic field we have that

$$\langle \nabla F, \hat{\sigma}_{NEW}^{-1} \nabla H_y^S \rangle_{L^2(\Omega)} + j\omega \langle F, \mu_{NEW}^H H_y^S \rangle_{L^2(\Omega)} = -\langle \nabla F, \tilde{\sigma}_{NEW}^{-1} \nabla H_y^P \rangle_{L^2(\Omega)}, \quad (2.47)$$

where $\tilde{\sigma}_{NEW}$ is then given by

$$\tilde{\sigma}_{NEW} = \begin{pmatrix} \tilde{\sigma} \frac{Y(x)}{Y(z)} & 0 \\ 0 & \tilde{\sigma} \frac{Y(z)}{Y(x)} \end{pmatrix}, \quad (2.48)$$

and for the two variational formulations, $\tilde{V}(\Omega) = \{F \in L^2(\Omega) : F|_{\Gamma_D} = 0, (\mathcal{J}_{2D}^{-1})^T \nabla F \in L^2(\Omega)\}$.

2.6 ABSTRACT FORMULATION

The derived variational formulations can be represented using the following abstract variational setting that will be useful in the next Chapter, that is:

$$\begin{cases} \text{Find } \hat{u} \in V, & \text{such that} \\ b(v, \hat{u}) = G(v) & \forall v \in V, \end{cases} \quad (2.49)$$

where $b(v, \hat{u})$ is a sesquilinear form (antilinear in v and linear in \hat{u}) and $G(v)$ (an antilinear form in v). We then have that:

3D MODEL:

- In both cases

$$\left\| \begin{aligned} v &= \mathbf{F}, \\ V &= \{ \mathcal{J}_{3D}^{-1} \mathbf{F} \in L^2(\Omega) : (\mathbf{n} \times \mathbf{F})|_{\Gamma_D} = 0, \frac{1}{\det(\mathcal{J}_{3D})} \mathcal{J}_{3D} \nabla \times \mathbf{F} \in L^2(\Omega) \}. \end{aligned} \right. \quad (2.50)$$

- E-Formulation

$$\left\| \begin{aligned} \hat{u} &= \mathbf{E}, \\ b(\mathbf{F}, \mathbf{E}) &= \langle \nabla \times \mathbf{F}, (\boldsymbol{\mu}_{NEW}^E)^{-1} \nabla \times \mathbf{E} \rangle_{L^2(\Omega)} - \langle \mathbf{F}, k_{NEW}^2 \mathbf{E} \rangle_{L^2(\Omega)}, \\ G(\mathbf{F}) &= -j\omega \langle \mathbf{F}, \mathbf{J}_{NEW}^{imp} \rangle_{L^2(\Omega)} - \langle \nabla \times \mathbf{F}, \boldsymbol{\mu}^{-1} \mathbf{M}_{NEW}^{imp} \rangle_{L^2(\Omega)}. \end{aligned} \right. \quad (2.51)$$

- H-Formulation

$$\left\| \begin{aligned} \hat{u} &= \mathbf{H}, \\ b(\mathbf{F}, \mathbf{H}) &= \langle \nabla \times \mathbf{F}, \hat{\sigma}_{NEW}^{-1} \nabla \times \mathbf{H} \rangle_{L^2(\Omega)} + j\omega \langle \mathbf{F}, \mu_{NEW}^H \mathbf{H} \rangle_{L^2(\Omega)}, \\ G(\mathbf{F}) &= -\langle \mathbf{F}, \mathbf{M}_{NEW}^{imp} \rangle_{L^2(\Omega)} + \langle \nabla \times \mathbf{F}, \hat{\sigma}_{NEW}^{-1} \mathbf{J}_{NEW}^{imp} \rangle_{L^2(\Omega)}. \end{aligned} \right. \quad (2.52)$$

2D MODEL:

- In both cases

$$\left\| \begin{aligned} v &= F, \\ V &= \{F \in L^2(\Omega) : F|_{\Gamma_D} = 0, (\mathcal{J}_{2D}^{-1})^T \nabla F \in L^2(\Omega)\}. \end{aligned} \right. \quad (2.53)$$

- E-Formulation

$$\left\| \begin{aligned} \hat{u} &= E_y, \\ b(F, E_y) &= \langle \nabla F, (\mu_{NEW}^E)^{-1} \nabla E_y \rangle_{L^2(\Omega)} - \langle F, k_{NEW}^2 E_y \rangle_{L^2(\Omega)}, \\ G(F) &= -j\omega \langle F, \mathbf{J}_{NEW}^{imp} \rangle_{L^2(\Omega)}. \end{aligned} \right. \quad (2.54)$$

- H-Formulation

$$\left\| \begin{aligned} \hat{u} &= H_y, \\ b(F, H_y) &= \langle \nabla F, \hat{\sigma}_{NEW}^{-1} \nabla H_y \rangle_{L^2(\Omega)} + j\omega \langle F, \mu_{NEW}^H H_y \rangle_{L^2(\Omega)}, \\ G(F) &= -\langle F, \mathbf{M}_{NEW}^{imp} \rangle_{L^2(\Omega)}. \end{aligned} \right. \quad (2.55)$$

1D MODEL:

- In both cases

$$\left\| \begin{aligned} v &= F, \\ V &= \{F \in L^2(\Omega) : F|_{\Gamma_D} = 0, (\mathcal{J}_{1D}^{-1})^T \nabla F \in L^2(\Omega)\}. \end{aligned} \right. \quad (2.56)$$

- E-Formulation

$$\left\| \begin{aligned} \hat{u} &= E_y, \\ b(F, E_y) &= \langle \nabla F, \mu_{NEW}^{-1} \nabla E_y \rangle_{L^2(\Omega)} - \langle F, k_{NEW}^2 E_y \rangle_{L^2(\Omega)}, \\ G(F) &= -\langle F, \mathbf{M}_{NEW}^{imp} \rangle_{L^2(\Omega)}. \end{aligned} \right. \quad (2.57)$$

- H-Formulation

$$\left\| \begin{aligned} \hat{u} &= H_y, \\ b(F, H_y) &= \langle \nabla F, \hat{\sigma}_{NEW}^{-1} \nabla H_y \rangle_{L^2(\Omega)} + j\omega \langle F, \mu_{NEW}^H H_y \rangle_{L^2(\Omega)}, \\ G(F) &= -\langle F, M_{NEW}^{imp} \rangle_{L^2(\Omega)}. \end{aligned} \right. \quad (2.58)$$

These variational formulations are valid with and without PML. For the latter, it is only necessary to define $\beta_i = 1$ for all directions in equation (2.36). For the 1D and 2D problems, \hat{u} is a scalar-valued solution function, while for the 3D problem, it corresponds to a vector-valued function. With the FE solution we compute the *quantity of interest* (QoI) $L^i(\hat{u})$ using the so called *output functional* L^i , a linear and continuous functional [111, 110] associated to the i -th receiver and defined as:

$$L^i(u) = \frac{1}{|\Omega_{R^i}|} \int_{\Omega_{R^i}} u, \quad (2.59)$$

where Ω_{R^i} is the domain occupied by the i -th receiver. In this expression, u is a scalar function. Therefore, when vectorial measurements are performed as in 3D Earth models, each component of the vector is calculated separately as a scalar-valued function according to (2.59).

In the case of the secondary field formulation, because of the linearity of L^i , we compute the linear QoI as:

$$L^i(\mathbf{E}) = L^i(\mathbf{E}^P) + L^i(\mathbf{E}^S), \quad (2.60)$$

and

$$L^i(\mathbf{H}) = L^i(\mathbf{H}^P) + L^i(\mathbf{H}^S). \quad (2.61)$$

SOLUTION OF THE FORWARD PROBLEM

The MT problem requires to accurately solve Maxwell's equations in an arbitrary domain with limited computational cost. Analytical solutions for 1D scenarios are known. However, for general 2D and 3D configurations, the estimation of the electric and magnetic fields requires a suitable numerical method. FD were able to accurately solve some complex scenarios (see [80, 135, 136] for instance). However, FDs use structured grids, and this limits their application range. In particular, when the solution includes special features requiring a refinement of the mesh, even if the refinement is justified in a given region, it must be applied in the whole domain to keep structured grids. Unstructured grids, which are usually employed in the FEM, offer more flexibility than structured grids. They allow refinements only in specific areas, and hence become ideal to correctly capture the complexity of the Earth's subsurface. FEM has become popular in the context of MT by the works of Mogi in 1996 [89] or Mitsuhashi and Uchida in 2004 [88]. Adaptive methods have been also applied to 2D MT modeling. For instance, Key and Weiss in 2006 [73] and Franke et al. [45] in 2007, employed h -adaptive mesh refinements using a posteriori error estimators.

We propose to use the self-adaptive hp -FEM [35] (h denotes the element size and p the order of approximation associated to each element). It is a numerical method that provides low discretization errors and thus accurate results with reduced computational cost. We build the refined hp -mesh by employing a goal-oriented adaptive strategy [119], which minimizes the error of a prescribed QoI represented by a linear functional (see [98, 119, 103, 122, 56] for details).

In MTs, it is necessary to obtain accurate results at multiple receiver positions, which justifies to extend the goal-oriented strategy to a multigoal-oriented one. There exist two possible approaches towards multigoal-oriented adaptivity. The first one consists in using one grid for each goal, as in [140], where the implementation needs to handle multiple grids, which in general may be complicated. The second one consists in defining a new QoI that simultaneously takes into account all goals (see [55, 54]). Based on this second approach, we propose to implement the algorithm proposed by Pardo in [105].

3.1 SOLUTION FOR A 1D LAYERED MEDIA

We consider the same underlying Earth formation as in section 1.3.3, that is, a sequence of N horizontal layers, where the conductivity of the i -th layer is given by $\sigma_i = \sigma_i(z)$. Omitting the source term, the fundamental solutions of the y component of the electric field at each layer should satisfy the following equation:

$$\frac{\partial E_y}{\partial z} + \eta_i^2 E_y = 0, \quad (3.1)$$

where $\eta_i^2 = \omega^2 \mu \varepsilon - j\omega \mu \sigma_i$.

For this 1D layered configuration of the Earth, assuming piecewise constant material properties, it is possible to obtain the 1D analytical solution for the electromagnetic fields everywhere, and from there, the impedance tensor.

COMPUTATION OF THE ELECTRIC AND MAGNETIC FIELDS:

We employ an approach described by Chew in the second chapter of his book [28] to obtain explicitly the solution for the electric field. Once it is computed, the magnetic field can be obtained according to Faradays's law, and subsequently, one could compute the impedance. Notice that, as shown in the second chapter of Weaver's book [164], it is also possible to compute directly the impedance at the layer interfaces by using Wait's recursion formula.

Being the electrical permittivity and magnetic permeability constant, the Fresnel reflection and transmission coefficients (R and T), between two different media indexed by i and k , are equal for the TE and TM modes and read as:

$$R_{ik} = \frac{\eta_i - \eta_k}{\eta_i + \eta_k}, \quad (3.2)$$

$$T_{ik} = 1 + R_{ik} = \frac{2\eta_i}{\eta_i + \eta_k}. \quad (3.3)$$

These coefficients were first derived by Fresnel in 1823, and they can be obtained for instance, by imposing the BC at the layer interfaces.

To derive the solution for the y component of the electric field in a general N -layered medium, we first consider the case of a subsurface composed of three layers (see Figure 3.1).

In the first layer, the solution is of the form

$$E_{y1} = A_1(e^{-j\eta_1 z} + \tilde{R}_{12}e^{2j\eta_1 z_1 + j\eta_1 z}), \quad (3.4)$$

where \tilde{R}_{12} is a reflection coefficient, given by the ratio of the upgoing and downgoing wave amplitudes at the first interface ($z = -z_1$). In the second layer, we have that

$$E_{y2} = A_2(e^{-j\eta_2 z} + R_{23}e^{2j\eta_2 z_2 + j\eta_2 z}), \quad (3.5)$$

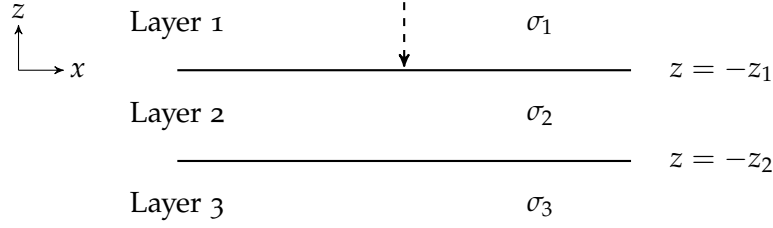


Figure 3.1: Incident plane wave impinging perpendicularly to a three horizontal layered domain.

where R_{23} is the Fresnel reflection coefficient for a downgoing wave in region 2 reflected by region 3. Since the third region extends to infinity, only the downgoing wave exists and then the solution is given by

$$E_{y3} = A_3 e^{-j\eta_3 z}. \quad (3.6)$$

In these expressions, A_1, A_2, A_3 , and \tilde{R}_{12} are unknown. We obtain them by imposing *constraint conditions* at the interfaces. Namely,

At $z = -z_1$:

- The downgoing wave in region 2 is equal to the transmission of the downgoing wave amplitude in region 1 plus the reflection of the upgoing wave in region 2. Then,

$$A_2 e^{j\eta_2 z_1} = A_1 e^{j\eta_1 z_1} T_{12} + R_{21} A_2 R_{23} e^{2j\eta_2 z_2 - j\eta_2 z_1}. \quad (3.7)$$

- The upgoing wave in region 1 is equal to the reflection of the downgoing wave in region 1 plus the transmission of the upgoing wave in 2. Then,

$$A_1 \tilde{R}_{12} e^{j\eta_1 z_1} = R_{12} A_1 e^{j\eta_1 z_1} + T_{21} A_2 R_{23} e^{2j\eta_2 z_2 - j\eta_2 z_1}. \quad (3.8)$$

From (3.7), A_2 is:

$$A_2 = \frac{A_1 e^{j(\eta_1 - \eta_2) z_1} T_{12}}{1 - R_{21} R_{23} e^{2j\eta_2(z_2 - z_1)}}. \quad (3.9)$$

Introducing this expression in (3.8), we obtain

$$\tilde{R}_{12} = R_{12} + \frac{T_{12} R_{23} T_{21} e^{2j\eta_2(z_2 - z_1)}}{1 - R_{21} R_{23} e^{2j\eta_2(z_2 - z_1)}}, \quad (3.10)$$

where \tilde{R}_{12} is the *generalized reflection coefficient*, which relates the amplitude of the upgoing wave to the amplitude of the downgoing wave in region 1. It includes the effect of subsurface reflection as well as the reflection from the first interface. In fact, we can add a new layer at the bottom and compute \tilde{R}_{12} just by replacing R_{23} by \tilde{R}_{23} .

We extend this result to the N -layered media (see Figure 3.2). Thus, the solution in the i -th region is given by

$$E_{yi} = A_i (e^{-j\eta_i z} + \tilde{R}_{i,i+1} e^{2j\eta_i z_i + j\eta_i z}). \quad (3.11)$$

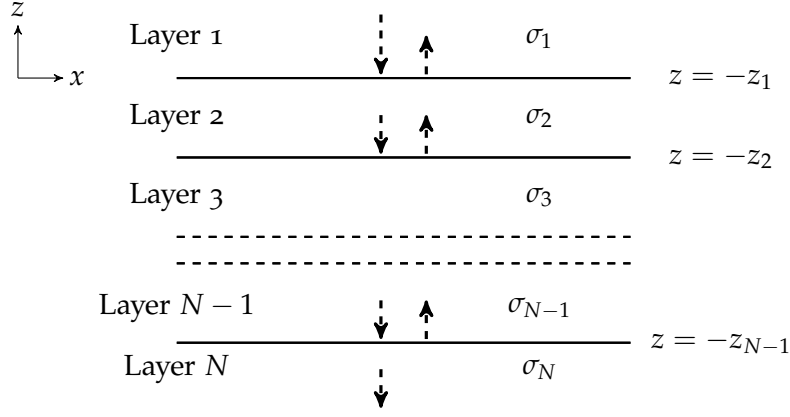


Figure 3.2: Incident plane wave impinging perpendicularly to a N horizontal layered medium.

Here, we need to compute the $\tilde{R}_{i,i+1}$ and A_i coefficients for all regions. We compute the generalized reflection coefficient $\tilde{R}_{i,i+1}$, at the interface between $i, i+1$ according to:

$$\tilde{R}_{i,i+1} = \frac{R_{i,i+1} + \tilde{R}_{i+1,i+2} e^{2j\eta_{i+1}(z_{i+1}-z_i)}}{1 + R_{i,i+1} \tilde{R}_{i+1,i+2} e^{2j\eta_{i+1}(z_{i+1}-z_i)}}, \quad (3.12)$$

with $\tilde{R}_{N,N+1} = 0$. This recursive relation has been traced back to Stokes (see Bellman and Wing [13]) and allows us to compute $\tilde{R}_{i,i+1}$ in terms of $\tilde{R}_{i+1,i+2}$.

The coefficients A_i are also recursively computed in terms of adjacent layers thanks to this expression

$$A_i = \frac{A_{i-1}(1 + R_{i-1,i})e^{j(\eta_{i-1}-\eta_i)z_{i-1}}}{1 + R_{i-1,i}\tilde{R}_{i,i+1}e^{2j\eta_i(z_i-z_{i-1})}}, \quad (3.13)$$

according to the fact that we have computed $\tilde{R}_{i,i+1}$ already.

3.2 SOLUTION TO THE 2D PROBLEM: hp -FEM

In the h -adaptive version of the FEM, the polynomial order of approximation p is fixed (and usually small), while the element size h varies from element to element. In the case of p -adaptivity, the contrary happens, that is, h is fixed and p varies from element to element. The hp -FEM incorporates both features and both h and/or p may vary across elements, which constitutes a tremendous advantage since the combination of both types of refinements may provide faster convergence.

Optimal hp -meshes provide exponential convergence rates for elliptic problems with a piecewise analytic solution, whereas h or p versions converge only algebraically. This was proven in 1D by Gui and Babuska [52] and in 2D by Babuska and Gui [7] and Schwab [129]. Only the hp -FEM is able to combine small elements (needed to capture geometrical details such as thin edges) with higher orders of approximation (necessary to decrease the dispersion error in wave propagation problems [61, 62, 97]). Additionally,

it is robust for singularly perturbed problems, that is, it still performs appropriately when a parameter involved in a given elliptic problem approximates a critical value [129].

Both the implementation and the theoretical analysis of hp -FEM are difficult, forcing to design adequate data structures and proper *a posteriori* error estimators. We thus want to point out the work in data structures performed by Demkowicz et al [35, 42], and the one carried out by Babuska et al [7, 6], Oden et al [96], and Demkowicz et al [43] in the area of error estimation.

The FEM is a special case of the Galerkin method that differs from others by the construction of the basis functions. The domain Ω is divided into disjoint subdomains called *finite elements*. They are usually either triangles or quads in 2D (other types of elements also exist, but their use is more rare), being the latter the ones employed in our computations.

3.2.1 Discretization of the Variational Problem

We restrict ourselves to the Bubnov-Galerkin method, which employs the same trial and test functions.

Let $V_h \subset V$ be an hp -FEM subspace and let $\{e_h^1, \dots, e_h^N\}$ be a basis of V_h , where $N = \dim(V_h)$ is the dimension of the approximate space. We discretize the abstract variational problem (2.49) to obtain the Forward Direct Problem

$$\begin{cases} \text{Find } u_h \in V_h \text{ such that:} \\ b(v_h, u_h) = G(u_h) \quad \forall v_h \in V_h. \end{cases} \quad (3.14)$$

The approximate solution is then represented as:

$$u_h(\mathbf{x}) = \sum_{k=1}^N u_h^k e_h^k(\mathbf{x}), \quad (3.15)$$

where the unknown coefficients u_h^k , $k = 1, \dots, N$ correspond to the so called *global degrees of freedom* (dof), and e_h^k are the *basis functions*. Substituting the approximate solution (3.15) into the discrete variational problem (3.14), and selecting one test basis function $v_h^l = e_h^l$, $l = 1, \dots, N$ at a time, we obtain the following algebraic system of equations:

$$\begin{cases} \text{Find } u_h^k, \quad k = 1, \dots, N \text{ such that:} \\ b(e_h^l, \sum_{k=1}^N u_h^k e_h^k) = G(e_h^l), \quad l = 1, \dots, N, \end{cases} \quad (3.16)$$

which can be rewritten as:

$$\begin{cases} \text{Find } u_h^k, \quad k = 1, \dots, N \text{ such that:} \\ \sum_{k=1}^N u_h^k B_{kl} = G_l, \quad l = 1, \dots, N. \end{cases} \quad (3.17)$$

Here, B_{kl} corresponds to each of the entries of the *global stiffness matrix* \mathbf{B} ,

$$B_{kl} = b(e_h^l, e_h^k), \quad (3.18)$$

and G_l is the l -th component of the *load vector* or *forcing term* \mathbf{G} ,

$$G_l = G(e_h^l). \quad (3.19)$$

This system of algebraic equations is equivalent to the approximate problem (3.14), and can be represented using matricial notation

$$\mathbf{B}\mathbf{u} = \mathbf{G}, \quad (3.20)$$

where \mathbf{u} corresponds to the vector that contains the unknown dof coefficients u_h^i . The approximate solution depends upon the selected space V_h , but it is independent of the choice of basis functions e_h^k . In practice, however, the choice of the basis functions affects the conditioning of the final linear system [9, 59] of equations and in some cases round-off error may notably affect the obtained solution [2].

3.2.2 Master Element and Basis Functions

For each *physical element* K , we define the corresponding *shape functions* $\hat{\phi}$ as the restriction of a basis function e_h^k to an element.

1D MASTER ELEMENT AND BASIS FUNCTIONS:

Geometrically, the 1D *master element* \hat{K} occupies the $[0, 1]$ interval. Each of the N physical elements in which the domain is partitioned is associated to the master element (via a bijective map) in which calculations are easier to perform. The element endpoints are known as *vertex nodes*. The *element space of shape functions* is identified with the space of polynomials of order p . We decide to use a set of *hierarchical shape functions* defined as:

$$\begin{aligned} \hat{\chi}_1(\xi) &= 1 - \xi, \\ \hat{\chi}_2(\xi) &= \xi, \\ \hat{\chi}_3(\xi) &= -(1 - \xi)\xi, \\ \hat{\chi}_{2+j}(\xi) &= (1 - \xi)\xi \frac{-1}{j(j+1)} \frac{dP_j}{d\xi}(-1 + 2\xi) \quad j = 1, \dots, p-1, \end{aligned} \quad (3.21)$$

where $P_j(-1 + 2\xi)$ are rescaled Integrated Legendre polynomials [145].

We classify the global basis functions into vertex nodes basis functions and in *middle nodes* basis functions. The construction of the first ones is illustrated in Figure 3.3 and they are given as the sum of the two shape functions associated to the same vertex node and extended zero elsewhere. The middle node basis functions vanish at the element endpoints, and they are also called *bubble functions* for this reason. This fact makes their construction easier, since it is only necessary to extend them by zero everywhere.

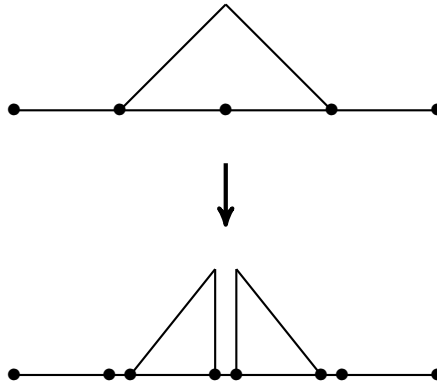


Figure 3.3: Construction of a vertex node basis function (from [35]).

2D QUADRILATERAL MASTER ELEMENT AND BASIS FUNCTIONS:

The 2D master element \hat{K} corresponds to a canonical quadrilateral that occupies the standard reference space $[0, 1] \times [0, 1]$. Again, we associate each quadrilateral *physical element* in which the domain is partitioned with the master element to perform the calculations. The element space of shape functions corresponds to polynomials of order p_h in ζ_1 and order p_v with respect ζ_2 . Each of the element edges may have a different order of approximation $p_i, i = 1, \dots, 4$, satisfying the so-called minimum rule [35], namely:

$$p_1, p_3 \leq p_h, \quad \text{and} \quad p_2, p_4 \leq p_v. \quad (3.22)$$

Three different groups of element shape functions over the master element exist attending to the nodal connectivity. To understand how these functions are built, we illustrate in Figure 3.4 the notion of abstract nodes. Each \hat{a}_j with $j = 1, \dots, 4$, corresponds to a vertex

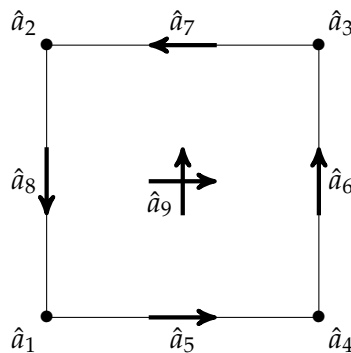


Figure 3.4: Nodes in a quadrilateral master element (from [35]).

node; $j = 5, \dots, 8$ to mid-edge nodes, and $j = 9$ to the middle node. For the first ones, the associated order of approximation is $p = 1$, p_i is the order for the edge nodes, while (p_h, p_v) correspond to the middle node.

Thus, the three different groups of element shape functions over the master element, which are obtained as tensor products of the 1D shape functions defined before, are given by:

- 4 vertex shape functions:

$$\begin{aligned}
 \hat{\phi}_1(\xi_1, \xi_2) &= \hat{\chi}_1(\xi_1)\hat{\chi}_1(\xi_2) = (1 - \xi_1)(1 - \xi_2), \\
 \hat{\phi}_2(\xi_1, \xi_2) &= \hat{\chi}_2(\xi_1)\hat{\chi}_1(\xi_2) = \xi_1(1 - \xi_2), \\
 \hat{\phi}_3(\xi_1, \xi_2) &= \hat{\chi}_2(\xi_1)\hat{\chi}_2(\xi_2) = \xi_1\xi_2, \\
 \hat{\phi}_4(\xi_1, \xi_2) &= \hat{\chi}_1(\xi_1)\hat{\chi}_2(\xi_2) = (1 - \xi_1)\xi_2.
 \end{aligned} \tag{3.23}$$

- $p_i - 1$ edge shape functions for each edge:

$$\begin{aligned}
 \hat{\phi}_{5,j}(\xi_1, \xi_2) &= \hat{\chi}_{2+j}(\xi_1)\hat{\chi}_1(\xi_2) & j = 1, \dots, p_1 - 1, \\
 \hat{\phi}_{6,j}(\xi_1, \xi_2) &= \hat{\chi}_2(\xi_1)\hat{\chi}_{2+j}(\xi_2) & j = 1, \dots, p_2 - 1, \\
 \hat{\phi}_{7,j}(\xi_1, \xi_2) &= \hat{\chi}_{2+j}(1 - \xi_1)\hat{\chi}_2(\xi_2) & j = 1, \dots, p_3 - 1, \\
 \hat{\phi}_{8,j}(\xi_1, \xi_2) &= \hat{\chi}_1(\xi_1)\hat{\chi}_{2+j}(1 - \xi_2) & j = 1, \dots, p_4 - 1.
 \end{aligned} \tag{3.24}$$

- $(p_h - 1)(p_v - 1)$ interior (bubble) shape functions:

$$\hat{\phi}_{9,j}(\xi_1, \xi_2) = \hat{\chi}_{2+i}(\xi_1)\hat{\chi}_{2+j}(\xi_2) \quad i = 1, \dots, p_h - 1; j = 1, \dots, p_v - 1. \tag{3.25}$$

We obtain the global basis functions by “gluing together” the element shape functions. For more information, we refer to [37].

3D HEXAEDRAL MASTER ELEMENT:

It is possible to build the basis functions in a similar manner by using the *tensor-product* structure. The resulting basis functions correspond then to vertex nodes basis functions, edge nodes basis functions, face nodes basis functions, and interior nodes basis functions. Due to the implementation complexity of the 3D *hp*-FEM computations, in this dissertation we avoid dealing with them. However, all results presented here can be extended to that case. For further information on the construction of 3D basis functions, we refer to [42].

3.3 MESH CONSTRUCTION

Realistic geological models are often geometrically complex since they exhibit inhomogeneities. The first and usually easiest approach when defining a finite element grid consists in using regular meshes. Sufficiently fine structured grids are often able to capture these inhomogeneities and/or to ensure enough accuracy at the receivers. However, the resulting grids may include elements with very large aspect ratios, which are well known to produce bad conditioning of the resulting linear system. Moreover, when us-

ing structured grids, the refinements extend to the whole domain, rapidly increasing the problem size.

Adaptive grids iteratively approximate the solution using a sequence of refined grids (in the case of hp -FEM in both, h and/or p) until a desired error tolerance is achieved. They easily capture any inhomogeneity and provide a sufficiently fine grid in the neighborhood of the receivers (where high accuracy in the solution is desired), introducing small elements only in the areas of interest. They become, therefore, highly suitable for modeling arbitrarily shaped interfaces as the ones that may appear in MT. Furthermore, since the size of the unstructured elements can rapidly increase with distance, the total number of unknowns is under control. Thus, to build the hp -mesh, we employ an adaptive algorithm based on the so called goal-oriented adaptivity.

3.3.1 Goal-Oriented Adaptivity

This strategy was first proposed by Becker and Rannacher in the mid 90's [12, 11, 10] as an attempt to overcome the problems arisen from energy norm based self-adaptive strategies [8]. Even if energy norm based adaptive strategies are robust in many applications, when the goal is to obtain results only in some specific areas of the domain as in MT, the energy norm based strategies provide limited information about the accuracy of the solution. It is known (see [104] for instance) that adaptive grids based on the energy norm may give relative errors in the solution surpassing 1000% even in situations where energy norm errors are below 1%. For these reasons, we employ a goal-oriented strategy to design the mesh.

This strategy approximates the solution by minimizing the error of a prescribed QoI that has physical or engineering applications and it is mathematically expressed in terms of a linear functional [98, 119]. This error in the QoI is represented as a function of the errors of the original and adjoint problems. Then, an upper bound of this error is defined in terms of some norms, and finally this upper bound is employed to perform local refinements only in the required specific areas. The objective of traditional goal-oriented strategies is to construct an optimal grid in the sense that it minimizes the problem size needed to achieve a given tolerance error for a given QoI.

The ability of goal-oriented algorithms to provide accurate solutions in a region of interest in the context of hp -FEM has been described in various works [139, 110]. In addition to Electromagnetics, where it has been widely employed (see for example [109]), it has also been applied to other fields such as fluid flow or fluid-structure interaction (for instance [153]), control theory (see [14]), or structural problems [74].

To describe this strategy, we start with the definitions of the forward direct problem and its discrete counterpart:

$$\left\{ \begin{array}{l} \text{Find } \hat{u} \in V, \hat{u}_h \in V_h, \quad \text{such that:} \\ \qquad \qquad \qquad b(v, \hat{u}) = G(v), \quad \forall v \in V, \\ \qquad \qquad \qquad b(v_h, \hat{u}_h) = G(v_h), \quad \forall v_h \in V_h. \end{array} \right. \quad (3.26)$$

We define its associated i -th adjoint problem (there is one adjoint problem for each of the N_{rec} receivers) as:

$$\left\{ \begin{array}{l} \text{Find } \hat{v}^i \in V, \hat{v}_h^i \in V_h, \quad \text{such that:} \\ \qquad \qquad \qquad b(\hat{v}^i, u) = L^i(u), \quad \forall u \in V, \\ \qquad \qquad \qquad b(\hat{v}_h^i, u_h) = L(u_h), \quad \forall u_h \in V_h. \end{array} \right. \quad (3.27)$$

Each problem admits a unique solution \hat{v}^i in V . This solution is usually referred to as the *influence function* and L^i is the linear functional that defines the linear QoI for the i -th receiver. Since we use a direct solver, the linear system of equations is factorized only once and the extra cost for solving the adjoint problems reduces to only backward and forward substitutions.

We define the error function of the direct problem as $e = \hat{u} - \hat{u}_h$ and we denote the error in the QoI by E_Q^i . Then, we have the following identity from the adjoint problem:

$$E_Q^i := L^i(e) = b(\hat{v}^i, e). \quad (3.28)$$

We aim at obtaining a bound for this error (in terms of some norm) that only depends on local and computable quantities. When b is asymmetric or indefinite, it is then necessary to define a new sesquilinear form to define a norm. Since b mainly corresponds to the weak form of the Helmholtz operator, then a natural choice is to select the new sesquilinear form \tilde{b} as the weak form of the operator $(-\Delta + \eta^2)(\cdot)$, which is symmetric and positive definite. The inner product and norm associated with the form \tilde{b}_K are denoted by

$$\langle \cdot, \cdot \rangle_{\tilde{b}_K}, \quad \text{and} \quad \|\cdot\|_{\tilde{b}_K}, \quad (3.29)$$

respectively.

LEMMA 3.3.1. *Let u and v be in V and let*

$$b(v, u) := \langle \nabla v, \nabla u \rangle_{L^2} - \langle v, \eta^2 u \rangle_{L^2}, \quad (3.30)$$

$$\tilde{b}(v, u) := \langle \nabla v, \nabla u \rangle_{L^2} + \langle v, |\eta^2| u \rangle_{L^2}, \quad (3.31)$$

where η is the corresponding value for the TE and TM modes. Then, denoting by $b_K(\cdot, \cdot)$ the contribution of each element K to the bilinear form $b(\cdot, \cdot)$,

$$\sum_K |b_K(v, u)| \leq \sum_K \|v\|_{\tilde{b}_K} \|u\|_{\tilde{b}_K}. \quad (3.32)$$

Proof.

$$\begin{aligned} \sum_K |b_K(v, u)| &= \sum_K |\langle \nabla v, \nabla u \rangle_{L^2} - \langle v, \eta^2 u \rangle_{L^2}| \\ &\stackrel{\text{Tr.}}{\leq} \sum_K (|\langle \nabla v, \nabla u \rangle_{L^2}| + |\langle v, \eta^2 u \rangle_{L^2}|) \\ &\leq \sum_K (|\langle \nabla v, \nabla u \rangle_{L^2}| + |\eta^2| |\langle v, u \rangle_{L^2}|), \quad (\eta^2 \text{ cte in } K) \\ &\stackrel{\text{C.S.}}{\leq} \sum_K (\|\nabla v\|_{L^2} \|\nabla u\|_{L^2} + |\eta^2| \|v\|_{L^2} \|u\|_{L^2}) \\ &\leq \sum_K (\|v\|_{\tilde{b}_K} \|u\|_{\tilde{b}_K}). \end{aligned} \quad (3.33)$$

Here “Tr.” corresponds to the triangular inequality and “C.S.” to the Cauchy-Schwarz inequality. To demonstrate the last inequality we have that for each element K ,

$$\begin{aligned} (\|v\|_{\tilde{b}_K} \|u\|_{\tilde{b}_K})^2 &= \|\nabla v\|_{L^2}^2 \|\nabla u\|_{L^2}^2 + |\eta^4| \|v\|_{L^2}^2 \|u\|_{L^2}^2 \\ &\quad + |\eta^2| \|\nabla v\|_{L^2}^2 \|u\|_{L^2}^2 + |\eta^2| \|\nabla u\|_{L^2}^2 \|v\|_{L^2}^2 \\ &= \|\nabla v\|_{L^2}^2 \|\nabla u\|_{L^2}^2 + |\eta^4| \|v\|_{L^2}^2 \|u\|_{L^2}^2 \\ &\quad + 2|\eta^2| \|\nabla v\|_{L^2} \|\nabla u\|_{L^2} \|v\|_{L^2} \|u\|_{L^2} + c, \quad c \geq 0. \\ &\geq \|\nabla v\|_{L^2}^2 \|\nabla u\|_{L^2}^2 + |\eta^4| \|v\|_{L^2}^2 \|u\|_{L^2}^2 \\ &\quad + 2|\eta^2| \|\nabla v\|_{L^2} \|\nabla u\|_{L^2} \|v\|_{L^2} \|u\|_{L^2}, \\ &= \left(\|\nabla v\|_{L^2} \|\nabla u\|_{L^2} + |\eta^2| \|v\|_{L^2} \|u\|_{L^2} \right)^2, \end{aligned} \quad (3.34)$$

where

$$\begin{aligned}
 c &= |\eta^2| \|\nabla v\|_{L^2}^2 \|u\|_{L^2}^2 + |\eta^2| \|\nabla u\|_{L^2}^2 \|v\|_{L^2}^2 - 2|\eta^2| \|\nabla v\|_{L^2} \|\nabla u\|_{L^2} \|v\|_{L^2} \|u\|_{L^2} \\
 &= |\eta^2| \left(\|\nabla u\|_{L^2} \|v\|_{L^2} - \|\nabla v\|_{L^2} \|u\|_{L^2} \right)^2 \geq 0,
 \end{aligned} \tag{3.35}$$

and therefore,

$$\sum_K \left(\|\nabla v\|_{L^2} \|\nabla u\|_{L^2} + |\eta^2| \|v\|_{L^2} \|u\|_{L^2} \right) \leq \sum_K \|v\|_{\tilde{b}_K} \|u\|_{\tilde{b}_K}. \tag{3.36}$$

□

Using the triangular inequality together Lemma 3.3.1, we have that

$$\begin{aligned}
 |E_Q^i| = |L^i(e)| &= |b(\hat{\vartheta}^i, e)| = \left| \sum_K b_K(\hat{\vartheta}^i, e) \right| \leq \sum_K |b_K(\hat{\vartheta}^i, e)| \\
 &\leq \sum_K \|\hat{\vartheta}^i\|_{\tilde{b}_K} \|e\|_{\tilde{b}_K}.
 \end{aligned} \tag{3.37}$$

Although $\|e\|_{\tilde{b}_K}$ tends to zero as we refine the mesh, $\|\hat{\vartheta}^i\|_{\tilde{b}_K}$ does not. We can obtain a sharper bound *for free* by using the error of the adjoint problem $\epsilon^i := \hat{\vartheta}^i - \hat{\vartheta}_h^i$. The b -orthogonality of e with respect to V_h , that is, $b(v_h, e) = 0$, $\forall v_h \in V_h$ implies that $b(\hat{\vartheta}, e) = b(\epsilon^i, e)$, which allows us to obtain a sharper bound of the error $|E_Q^i|$:

$$\begin{aligned}
 |L^i(e)| &= |b(\epsilon^i, e)| = \left| \sum_K b_K(\epsilon^i, e) \right| \leq \sum_K |b_K(\epsilon^i, e)| \\
 &\leq \sum_K \|\epsilon^i\|_{\tilde{b}_K} \|e\|_{\tilde{b}_K},
 \end{aligned} \tag{3.38}$$

where now both factors tend to zero when the mesh is refined. Here, e and ϵ^i can be approximated by the difference between the fine and coarse grid solutions for the direct and adjoint problems, respectively.

This upper bound, which utilizes only local and computable quantities, allows us to design a goal-oriented hp -adaptive refinement strategy that minimizes $|L^i(e)|$. However, in MT, we need to efficiently compute several linear quantities of interest $L^i(u)$, $i = 1, \dots, N_{rec}$, at all receivers. This can be accomplished with goal-oriented strategies that solve N_{rec} different adjoint problems. However, to generate and refine multiple grids may become computationally expensive and difficult to implement. Therefore, we propose the use of a multigoal-oriented strategy, in which the solution at all receivers is computed simultaneously.

3.3.2 Extension to the Multigoal-Oriented Adaptivity

We now need to construct a proper hp -discretization that makes $L^i(u_h)$ be a good approximation of $L^i(u)$ not only at a single receiver, but for each value $i = 1, \dots, N_{rec}$. To know which elements have to be refined, we follow the strategy proposed in [105], and we adopt a multigoal-oriented strategy.

We would like to bound all relative errors in percentage by a given error tolerance denoted by TOL, that is,

$$\max_i \left\{ \frac{|L^i(u_h) - L^i(u)|}{|L^i(u)|} * 100 \right\} \leq TOL, \quad (3.39)$$

where we assume that $L^i(u) \neq 0$.

However, our QoI -right hand side of (3.27)- has to be defined as a linear functional, making expression (3.39) invalid. We thus proceed as follows:

- We first define a new linear QoI (new right hand side for the adjoint problem (3.27)):

$$\tilde{L}_u^{NEW}(v) := \sum_{i=1}^M \frac{L^i(v)}{L^i(u)}, \quad \forall v \in V, \quad (3.40)$$

where u is the solution of the forward problem. The stopping criteria for the adaptivity is given by:

$$\tilde{L}_u^{STOP}(v) := \sum_{i=1}^M \frac{|L^i(v)|}{|L^i(u)|} \leq TOL/100, \quad \forall v \in V. \quad (3.41)$$

At the discrete level, we approximate

$$\tilde{L}_{u_h}^{NEW}(v_h) := \sum_{i=1}^M \frac{L^i(v_h)}{L^i(u_h)}, \quad \forall v_h \in V_h. \quad (3.42)$$

These definitions allow us to define a self-adaptive goal-oriented hp -strategy that satisfies equation (3.39) and therefore bounds all relative errors (in percentage) by a given tolerance

$$\max_i \left\{ \frac{|L^i(u_h) - L^i(u)|}{|L^i(u)|} * 100 \right\} \leq \tilde{L}^{STOP}(e_h) * 100 \leq TOL. \quad (3.43)$$

- The relative error varies from receiver to receiver. To weight the importance in consonance with the error size (having more influence those with larger error), a correction to Equation (3.42) is introduced as follows:

$$\tilde{L}^{NEW}(v_h) := \sum_{i=1}^M R^i(e_h) \frac{L^i(v_h)}{L^i(u_h)}, \quad \forall v_h \in V_h, \quad (3.44)$$

where $R^i(e_h)$ is an estimation of the relative error of the i -th QoI. From a practical point of view, this relative error can be estimated by approximating the exact solution by the solution computed in a globally refined grid.

The same approach as in the goal-oriented adaptivity yields to the new error bound:

$$\begin{aligned} \max_i \left\{ \frac{|L^i(u_h) - L^i(u)|}{|L^i(u)|} * 100 \right\} &\leq |\tilde{E}^{NEW}| = |\tilde{L}^{NEW}(e)| \leq \sum_K |\tilde{b}_K(\epsilon, e)| \\ &\leq \sum_K \|\epsilon\|_{\tilde{b}_K} \|e\|_{\tilde{b}_K}, \end{aligned} \quad (3.45)$$

where again, \tilde{b}_K corresponds to the local contribution of element K to the sesquilinear form \tilde{b} .

Once we have this representation formula for the error in the QoI, we describe the adaptive algorithm.

3.3.3 Automatic hp -Adaptivity in 2D

We employ the adaptive algorithm described in [36], which corresponds to a modification of the original algorithm developed in [43]. It is based on the two following design features:

- Fine grid solution: Given a *coarse mesh*, we refine the mesh in both h and p to obtain a *fine mesh*, whose corresponding solution is referred to as the *fine mesh solution*. Thus, the hp refined grid provides a reference solution to compare with.
- Optimal mesh selection: Given the fine mesh solution, we use it to determine optimal mesh refinements on the coarse mesh by minimizing the projection based interpolation error, which we define next.

In contrast with the actual approximation error, which is global, the projection based interpolation error is determined locally, over one element at a time. That is the key point for the construction of the minimization algorithm. An example of such an adaptive strategy can be found in [110], where u is approximated by a fine grid solution and the *projection based interpolation operator* is used. This operator is defined in [39] and also used in [43] and [120]. It delivers optimal h -convergence and optimal (up to a logarithmic factor) p -convergence rates [38]. Then, by minimizing the interpolation error, we expect to obtain asymptotically optimal meshes. Thus, the operator projects the fine grid solution into the coarse mesh. To do so, it first interpolates the solution at each vertex node for each element. Having these values of the solution fixed, it projects the solution first along the edges and subsequently into the interior of the element. The main advantage of employing this projector comes from computing the projected solution locally rather than globally. Thus, we can estimate the difference between the fine and projected solutions in terms of local quantities (element by element), that is, in terms of quantities that do not vary globally when we modify the grid locally.

THE hp -ADAPTIVE ALGORITHM:

Once we have computed the fine grid solution to compare with, the algorithm works as follows:

- Step 1: For each element in the coarse mesh, select between p and h refinements. Using the projection-based interpolation error, select the refinement that produces the biggest error decrease rate per added unknown by comparing the fine mesh solution with the projected solution of the fine grid over the coarse space.
- Step 2: Determine which elements have to be refined: first, compute the maximum decrease rate over all elements, and then select elements having a decrease rate larger than a fraction of the maximum. As suggested by Demkowicz et. al in [43], we select this fraction as $1/3$.
- Step 3: Determine the optimal order of approximation for the elements to be refined: if a p -refinement is selected, then increase p by one. If h -refinement is preferred, then determine the value of the new polynomial orders for the new elements that yields the biggest decrease rate per added unknown and perform the h -refinement.

Once the forward problem is defined and the numerical method to solve it has been explained, in the next chapter we formulate the inverse MT problem and we propose a method to solve it.

FORMULATION AND NUMERICAL METHOD FOR THE SOLUTION OF THE INVERSE PROBLEM

In this Chapter, we describe the formulation of the MT inverse problem (IP) and we present it as a general constrained optimization problem (COP). We employ gradient based methods to numerically solve it, and we describe an efficient computation of the Jacobian and Hessian matrices for the *hp*-FEM. For our implementation, we select the L-BFGS-U method (where BFGS corresponds to the name of the authors: Broyden, Fletcher, Goldfarb, and Shanno) which is a quasi-Newton method. Finally, we present the proposed multi-dimensional inversion algorithm for MT measurements.

4.1 FORMULATION OF THE INVERSE PROBLEM

We start defining some basic ideas:

- The *model parameters* (or *model* m) are the physical parameters that capture the essential characteristics of the studied process. In MT, they correspond to the conductivity distribution of the Earth's subsurface.
- The *data* d are collected (or synthetic) observations consisting of EM measurements obtained at different surface locations and frequencies. Each measurement is associated with a *weight* θ to ponder its importance, which can correspond, for instance, to the noise that measurements incorporate.

In particular, if we discretize the inverse problem selecting N measurements and M model parameters, then the model parameters correspond to the set $m = \{m^1, m^2, \dots, m^M\}$, the data to $d = \{d^1, d^2, \dots, d^N\}^T$, and its associated weights to $\theta = \{\theta^1, \theta^2, \dots, \theta^N\}^T$.

- We call *forward operator* (or *mathematical model*) $g(\cdot)$ to the nonlinear operator that relates the data with the model:

$$g(m) = d, \tag{4.1}$$

where $g(m) = \{g^1(m), g^2(m), \dots, g^P(m)\}$ is the vector with the i -th component being equal to the QoI corresponding to the i -th experiment.

- The *cost function* $C(m)$ is a function that measures the *misfit* or agreement, in some l^p norm, between the data and the results of the mathematical model for some given model parameters. It can include a *regularization term* $R(m)$.

Thus, by solving the forward problem we predict or obtain the data (given a quantitative model and some model parameters), while by solving the IP we retry information about the model parameters (given a quantitative model and some measurements).

The objective in MT is to determine the conductivity distribution of the subsurface as a function of space. Hence, assuming that the remaining variables are known, the conductivity is the natural choice for the model parameters. Indeed, since we employ a truncated Taylor's series expansion in the inversion process, and since the quality of such approximation depends upon the variable with respect to which we perform such expansion, the selection of the model parameters becomes crucial. We represent by $m = m(\sigma)$ the different physical magnitudes that may be considered as model parameters. For example, in borehole resistivity logging, it is customary to design logging instruments in such a way that their response is (almost) inversely proportional to the formation conductivity, *i.e.* proportional to the resistivity of the formation. Under this design assumption, if we employ the change of variables $m(\sigma) = \sigma^{-1}$, then the cost functional is expected to be an (almost) linear function of the new variable m , and a method based on a first order Taylor's series expansion with respect to m should converge in (almost) one iteration.

Thus, we can consider a possible change of variables in the model and perform the inversion with the new variable. For that purpose, we develop a general theory of optimization (or inversion) with respect to this arbitrary variable m .

To define the cost functional, we select the l^2 -norm in the data space because it provides a quadratic functional, and thus, the first derivative becomes linear. We also consider a real valued function $R(m)$, employed for regularization purposes in the model space. Hence, the cost functional is given by:

$$C(m) = \sum_{\omega}^{N_{\omega}} \left(\|\theta(g_{\omega}(m) - d_{\omega})\|_{l^2(N)}^2 \right) + \lambda R(m), \quad (4.2)$$

where $\lambda > 0$ is the so-called regularization parameter and N_{ω} is the number of different frequencies that are considered. If the impedance is employed as QoI and several frequencies are considered, we need to include in the weights a term to ponder the different magnitude arisen from different frequencies. Thus, we divide the computed impedance and the measurements by $\sqrt{\omega}$ to normalize the order of magnitude. This factor comes from the formula (1.41) to compute apparent resistivities.

The model parameters are discretized according to

$$m(\sigma) = \sum_{i=1}^M m_i \chi_i(x), \quad (4.3)$$

where m_i are the coefficients and P is the number of basis functions employed to model the conductivity distribution (or the corresponding new variables throughout the change of coordinates) defined as:

$$\chi_i(\mathbf{x}) = \begin{cases} 1 & \text{if } x \in \Omega_i, \\ 0 & \text{if } x \notin \Omega_i, \end{cases} \quad (4.4)$$

where Ω_i stands for a particular i -th rectangular block of the domain.

Hence, our objective is to seek the argument \hat{m} , that is, the coefficients m_i in (4.3), that minimizes the cost functional:

$$\hat{m} = \arg \min_{m_l \leq m \leq m_u} C(m), \quad (4.5)$$

where lower (m_l) and upper (m_u) bounds of m are imposed in order to avoid unphysical values of the variable.

It is impossible to solve this nonlinear optimization problem explicitly. Therefore, it has to be solved numerically with some numerical method. Gradient based methods have been historically widely employed within the MT community. One of the initial approaches for solving nonlinear IPs in Geophysics consists in linearizing a cost functional related to a first-order Taylor expansion of some reference model, computing the solution to this linear inverse problem, taking this solution as the new reference model, and repeating this process iteratively until it converges. These schemes were generally solved with Newton's methods (often Gauss-Newton (GN) and Levenberg-Marquardt) and they were referred to as iterative linearized methods. The works of Wu [168] and Jupp and Vozoff [71] provide 1D examples for which nonlinear least-squares solutions are obtained. Constable et al. [33] and Booker [137] extended these works to problems including regularization parameters. 2D Earth models with regularization were studied by different authors [64, 83, 124, 138] or [34]. It is worth noting that [34] introduced the so called Occam's inversion in MTs, which had the basic idea of fitting the data by a model as simple and as smooth as possible in order to reduce the over interpretation of the data.

However, these linearized iterative methods are susceptible to detect local optimal solutions and in general could be slow due to the need of: (a) computing the full Jacobian of the forward operator and (b) solving a linear system on the model space at each iteration. Different authors tried to overcome these problems. Smith and Booker [138] employed a rapid relaxation inversion (RRI) technique to approximate horizontal derivatives with their values calculated from the fields of the previous iteration. Still, this method has some limitations when dealing with structures with little TM responses, ignoring lateral effects. Mackie and Madden [80] considered an approximation of the linearized IP, solving at each step a GN iteration incompletely using a truncated conjugate gradient (CG) technique. As Rodi and Mackie showed in [167], this approach is faster (but slower than the RRI) and less memory demanding than other linearized inversion methods because it only computes its action on specific vectors. The use of the CG method in nonlinear geophysical IP was suggested by Tarantola [147], and later in the context of MT by

Rodi and Mackie [167]. This widely used algorithm (e.g. [87, 101]) is based on a new nonlinear conjugate gradient (NLCG) scheme to minimize an objective function that penalizes data residuals and second spatial derivatives with respect to the resistivity of the structure, avoiding excessive evaluations of the forward problem and exploiting the computational techniques for performing Jacobian operations used in the Mackie-Maden algorithm. A GN type approach has also been used in MT, for instance in the works of Sasaki [126] and Siripunvaraporn et al [134], and also the limited-memory quasi-Newton method (L-BFGS-U) was employed by Avdeev and Avdeeva [4]. Further developments in MT inversion include the works of Ogawa and Uchida [100], Siripunvaraporn and Edbert [132, 133], Owaga [99], and Leet et al [77] (see [131] for a recent review of 3D MT inversion algorithms).

As stated in Ghaedrahmati et al [46], by comparing some of the aforementioned methods, it turns out that most of the 2D MT inversion algorithms fall in one of the following categories: the classical Occam's inversion, the data space Occam's inversion, the NLCG method or the GN method. Their implementations can be found in OCCA [33], DASOCC [132], NLCG [167], and MT2DInvMatlab [77].

4.2 SELECTING THE QUANTITY OF INTEREST

The traditional theory of goal-oriented adaptivity employs a linear and continuous functional [111, 110] in u as QoI, which in MT is often associated with the solution at the i -th receiver and defined as

$$L^i(u) = \frac{1}{|\Omega_{R^i}|} \int_{\Omega_{R^i}} u \, d\Omega. \quad (4.6)$$

Here, Ω_{R^i} stands for the domain occupied by the i -th receiver and u corresponds to some component of the electric or magnetic field.

In the case of geophysical resistivity applications, the appearance of nonlinear QoI is common, and therefore we need to compute them. Since the MT source intensity is unknown, it is then natural to define a QoI independent of it. A good candidate for this purpose is the impedance matrix \mathcal{Z} , a nonlinear quantity whose entries are defined as ratios between the electric and magnetic fields (see Section 1.3.1). Postprocessing the impedance, we obtain other suitable candidate for QoI, namely, the apparent resistivity of the subsurface (see Section 1.3.3), which is also nonlinear.

The definition of the impedance at the i -th receiver in terms of linear functionals is given by:

$$g^i(m) = \mathcal{Z}_{lk}^i(m) = \frac{L^i(E_l)}{L^i(H_k)}, \quad (4.7)$$

where l and k can be either x or y in 2D Cartesian coordinates.

4.3 NUMERICAL METHOD IN MT

4.3.1 Fundamentals of Gradient Based Methods

Given an initial guess $m^{(0)}$, our goal is to construct a sequence $m^{(n)}$ that iteratively converges towards the solution \hat{m} of problem (4.5) as the iteration number n tends to infinity. We consider iterations of the following type:

$$m^{(n+1)} = m^{(n)} + \alpha^{(n)} \delta m^{(n)}. \quad (4.8)$$

Here, $\delta m^{(n)}$ is the n -th increment to the solution (also called search direction), and $\alpha^{(n)}$ is the step size at iteration n .

Using a second order Taylor's series expansion of $C(m)$ in the neighborhood of $m^{(n)}$, we obtain:

$$C(m^{n+1}) \approx C(m^{(n)}) + \nabla C^T(m^{(n)}) \delta m^{(n)} + \frac{1}{2} (\delta m^{(n)})^T \mathcal{H}_C(m^{(n)}) \delta m^{(n)}, \quad (4.9)$$

where $\nabla C(m^{(n)})$ is the gradient and $\mathcal{H}_C(m^{(n)})$ the Hessian matrix. Thus, given an approximation $m^{(n)}$, in order to find a (local) minimum, we need the gradient to vanish, that is,

$$\frac{\partial C(m^{(n)})}{\partial \delta m^{(n)}} = 0. \quad (4.10)$$

SEARCH DIRECTION:

Imposing (4.10) to (4.9), we obtain the following search direction:

$$\delta m^{(n+1)} = -[\mathcal{H}_C(m^{(n)})]^{-1} \nabla C(m^{(n)}), \quad (4.11)$$

which yields to the Newton-Raphson method. If we choose

$$\mathcal{H}_C(m^{(n)}) \approx \left(\nabla C(m^{(n)}) \right)^T \nabla C(m^{(n)}), \quad (4.12)$$

we obtain the Gauss-Newton method, and selecting $\mathcal{H}_C(m^{(n)}) \approx I$, the steepest descend method is recovered.

The presence of the Hessian may imply additional difficulties. In particular, its calculation may be difficult, computationally expensive or even impossible. In addition, since the Hessian may not be positive definite, the computed direction defined as (4.11) may not be a descent direction. Furthermore, the Hessian may take a value equal to zero, which would make the method to break down. An approach to avoid these problems is to consider Quasi-Newton methods. In these methods, the Hessian is replaced by other symmetric and positive definite matrix that is updated at every iteration. This is the case of the L-BFGS-U method, which updates and approximates the Hessian at each iteration based on the limited-memory BFGS formula.

For this method, the search direction is computed employing the gradient projection [19, 32, 78, 91] (GP) in order to identify a set of active variables (the ones that will be held at their bounds). Then, the approximated quadratic model is minimized with respect to the free variables. The vector leading from the current iterate to this approximate minimizer corresponds then to the search direction.

Although a higher-order Taylor's series approximation of the cost functional may lead to more accurate methods, such approaches present two major drawbacks. They require to (1) find the roots of a high-order polynomial, and (2) evaluate high-order derivatives.

STEP SIZE:

Given the n -th iterate $m = m^{(n)}$ and the corresponding search direction $\delta m = \delta m^{(n)}$, there exist a plethora of algorithms for computing the step size $\alpha = \alpha^{(n)}$. Most of the methods (including Wolfe, Goldstein, and Armijo conditions, interpolation, and backtracking) require the evaluation of $C(m + \alpha \delta m)$ for several values of α . This operation may be computationally expensive, since for each value of α , we need to evaluate $g(m + \alpha \delta m)$, that is, we need to solve forward problems for all experiments. The L-BFGS-U method computes the step size performing a line search along the search direction using a subroutine described in Moré and Thunent [90].

4.3.2 Computation of the Jacobian and Hessian

When employing gradient based methods, we often need to compute the first and second derivatives of the cost functional, and hence, the first and second derivatives of the nonlinear QoI.

We always express the nonlinear QoI in terms of the linear functionals obtained with the hp -FEM. Thus, we express the analytical derivative of the nonlinear QoI also in terms of the derivatives of the linear functionals, which are computed numerically. Then, for the impedance, from equation (4.7) we have that the derivative of g^i is computed in terms of linear derivatives according to the following analytical expression:

$$\frac{\partial g^i(m)}{\partial m_j} = \frac{\partial \mathcal{Z}_{lk}^i(m)}{\partial m_j} = \frac{\frac{\partial L^i(E_l)}{\partial m_j} L^i(H_k) - \frac{\partial L^i(H_k)}{\partial m_j} L^i(E_l)}{\left(L^i(H_k)\right)^2}, \quad (4.13)$$

where l and k can be either x or y in 2D Cartesian coordinates.

To compute the entries of the first derivative of $L^i(u)$ with respect to each of the inversion variables m_j , we employ the chain rule:

$$[\mathcal{J}_{L_m}]_j^i = \frac{\partial L^i(u)}{\partial m_j} = \underbrace{\frac{\partial L^i(u)}{\partial \sigma_j}}_{[\mathcal{J}_{L_\sigma}]_j^i} \frac{\partial \sigma_j}{\partial m_j}, \quad (4.14)$$

where \mathcal{J}_{L_m} and \mathcal{J}_{L_σ} can be understood as arrays of N_{rec} vectors (one for each component of L^i) of dimension equal to the number of materials (basis functions for m or σ in the formation) M , or as matrices of dimension $N_{rec} \times M$. Notice that \mathcal{J}_{L_σ} is computed numerically, while $\partial\sigma_j/\partial m_j$ analytically.

Using again the chain rule, we compute the entries of the second derivatives as:

$$[\mathcal{H}_{L_m}]_{jk}^i = \frac{\partial^2 L^i(u)}{\partial m_j \partial m_k} = \underbrace{\frac{\partial^2 L^i(u)}{\partial \sigma_j \partial \sigma_k}}_{[\mathcal{H}_{L_\sigma}]_{jk}^i} \frac{\partial \sigma_j}{\partial m_j} \frac{\partial \sigma_k}{\partial m_k} + \underbrace{\frac{\partial L^i(u)}{\partial \sigma_j}}_{[\mathcal{J}_{L_\sigma}]_j^i} \frac{\partial^2 \sigma_j}{\partial m_j \partial m_k}. \quad (4.15)$$

\mathcal{H}_{L_m} and \mathcal{H}_{L_σ} are third order tensors, which can be understood as an array of N_{rec} Hessian matrices of dimension $M \times M$. Notice that once \mathcal{J}_{L_σ} and \mathcal{H}_{L_σ} are numerically evaluated, the calculation of \mathcal{J}_{L_m} and \mathcal{H}_{L_m} is straightforward and costless for any selection of m .

In the above two expressions, all terms are analytically computed except those corresponding to $[\mathcal{J}_{L_\sigma}]_j^i$ and $[\mathcal{H}_{L_\sigma}]_{jk}^i$, which are numerically evaluated by employing the solutions of the forward direct and adjoint problems (equations (3.26) and (3.27), respectively) and evoking the Representation Theorem [119], which states that:

$$L^i(\hat{u}) = G(\hat{\sigma}^i) = b(\hat{\sigma}^i, \hat{u}). \quad (4.16)$$

For that purpose, we first rewrite the bilinear form as follows:

$$b(v, u) := b(v, u; h(\sigma)) = b_1(v, u) + b_2(v, u; h(\sigma)), \quad (4.17)$$

where, b , b_1 and b_2 are sesquilinear forms in the first two variables, b_2 is linear in the third variable h , and b_1 is independent of h , a function that depends on the considered mode. We now derive the formulas to compute the entries of $[\mathcal{J}_{L_\sigma}]_j^i$. For more details on the exact finally implemented expressions, see Section 5.3.1, in Chapter 5, devoted to the impementation.

Jacobian

Applying the definition of L^i and its linearity with respect to u , we obtain:

$$\frac{\partial L^i(u)}{\partial \sigma_j} = b\left(\frac{\partial \hat{\sigma}^i}{\partial \sigma_j}, u; h(\sigma)\right) + b\left(\hat{\sigma}^i, \frac{\partial u}{\partial \sigma_j}; h(\sigma)\right) + b_2\left(\hat{\sigma}^i, u; \frac{\partial h(\sigma)}{\partial \sigma_j}\right), \quad (4.18)$$

$$L^i\left(\frac{\partial u}{\partial \sigma_j}\right) = b\left(\hat{\sigma}^i, \frac{\partial u}{\partial \sigma_j}; h(\sigma)\right).$$

Subtracting the above two equations, we have:

$$b\left(\frac{\partial \hat{\sigma}^i}{\partial \sigma_j}, u; h(\sigma)\right) = -b_2\left(\hat{\sigma}^i, u; \frac{\partial h(\sigma)}{\partial \sigma_j}\right). \quad (4.19)$$

With a similar argument and the definition of G and its linearity with respect to v , we obtain:

$$\frac{\partial G(v)}{\partial \sigma_j} = b \left(\frac{\partial v}{\partial \sigma_j}, \hat{u}; h(\sigma) \right) + b \left(v, \frac{\partial \hat{u}}{\partial \sigma_j}; h(\sigma) \right) + b_2 \left(v, \hat{u}; \frac{\partial h(\sigma)}{\partial \sigma_j} \right),$$

||

(4.20)

$$G \left(\frac{\partial v}{\partial \sigma_j} \right) = b \left(\frac{\partial v}{\partial \sigma_j}, \hat{u}; h(\sigma) \right).$$

Thus, we have:

$$b \left(v, \frac{\partial \hat{u}}{\partial \sigma_j}; h(\sigma) \right) = -b_2 \left(v, \hat{u}; \frac{\partial h(\sigma)}{\partial \sigma_j} \right).$$
(4.21)

Using the first equality in (4.16), we know that:

$$\frac{\partial L^i(\hat{u})}{\partial \sigma_j} = \frac{\partial G(\hat{v}^i)}{\partial \sigma_j},$$
(4.22)

so, combining the above formulas, we conclude:

$$[\mathcal{J}_{L^i}]_j^i = \frac{\partial L^i(\hat{u})}{\partial \sigma_j} = -b_2 \left(\hat{v}^i, \hat{u}; \frac{\partial h(\sigma)}{\partial \sigma_j} \right).$$
(4.23)

Evaluation of the Jacobian using the above formula requires integrating a function that depends both on the solutions to the forward direct and adjoint problems. Assuming that solutions for these two problems are already available from the simulations of the forward problems, the additional cost for computing the Jacobian reduces to a simple (Gaussian) integration scheme. This computational cost is negligible compared with the computational cost required for solving the corresponding forward problems.

Hessian

For second-order derivatives, we follow a similar approach as the one used for computing the Jacobian. We have that

$$\begin{aligned} \frac{\partial^2 L^i(u)}{\partial \sigma_j \partial \sigma_k} &= \\ &= b \left(\frac{\partial^2 \hat{v}^i}{\partial \sigma_j \partial \sigma_k}, u; h(\sigma) \right) + b \left(\frac{\partial \hat{v}^i}{\partial \sigma_j}, \frac{\partial u}{\partial \sigma_k}; h(\sigma) \right) + b_2 \left(\frac{\partial \hat{v}^i}{\partial \sigma_j}, u; \frac{\partial h(\sigma)}{\partial \sigma_k} \right) + \\ &+ b \left(\frac{\partial \hat{v}^i}{\partial \sigma_k}, \frac{\partial u}{\partial \sigma_j}; h(\sigma) \right) + b \left(\hat{v}^i, \frac{\partial^2 u}{\partial \sigma_j \partial \sigma_k}; h(\sigma) \right) + b_2 \left(\hat{v}^i, \frac{\partial u}{\partial \sigma_j}, \frac{\partial h(\sigma)}{\partial \sigma_k} \right) + \\ &+ b_2 \left(\frac{\partial \hat{v}^i}{\partial \sigma_k}, u; \frac{\partial h(\sigma)}{\partial \sigma_j} \right) + b_2 \left(\hat{v}^i, \frac{\partial u}{\partial \sigma_k}, \frac{\partial h(\sigma)}{\partial \sigma_j} \right) + b_2 \left(\hat{v}^i, u; \frac{\partial^2 h(\sigma)}{\partial \sigma_j \partial \sigma_k} \right). \end{aligned}$$
(4.24)

On the other hand,

$$\begin{aligned} \frac{\partial}{\partial \sigma_k} \left[L^i \left(\frac{\partial u}{\partial \sigma_j} \right) \right] &= \\ &= b \left(\frac{\partial \hat{\sigma}^i}{\partial \sigma_k}, \frac{\partial u}{\partial \sigma_j}; h(\sigma) \right) + b \left(\hat{\sigma}^i, \frac{\partial^2 u}{\partial \sigma_j \partial \sigma_k}; h(\sigma) \right) + b_2 \left(\hat{\sigma}^i, \frac{\partial u}{\partial \sigma_j}, \frac{\partial h(\sigma)}{\partial \sigma_k} \right). \end{aligned} \quad (4.25)$$

Using the definition of G and its linearity with respect to v , we obtain:

$$\begin{aligned} \frac{\partial G(v)}{\partial \sigma_j \partial \sigma_k} &= \\ &= b \left(\frac{\partial^2 v}{\partial \sigma_j \partial \sigma_k}, \hat{u}; h(\sigma) \right) + b \left(\frac{\partial v}{\partial \sigma_j}, \frac{\partial \hat{u}}{\partial \sigma_k}; h(\sigma) \right) + b_2 \left(\frac{\partial v}{\partial \sigma_j}, \hat{u}; \frac{\partial h(\sigma)}{\partial \sigma_k} \right) + \\ &+ b \left(\frac{\partial v}{\partial \sigma_k}, \frac{\partial \hat{u}}{\partial \sigma_j}; h(\sigma) \right) + b \left(v, \frac{\partial^2 \hat{u}}{\partial \sigma_j \partial \sigma_k}; h(\sigma) \right) + b_2 \left(v, \frac{\partial \hat{u}}{\partial \sigma_j}; \frac{\partial h(\sigma)}{\partial \sigma_k} \right) + \\ &+ b_2 \left(\frac{\partial v}{\partial \sigma_k}, \hat{u}; \frac{\partial h(\sigma)}{\partial \sigma_j} \right) + b_2 \left(v, \frac{\partial \hat{u}}{\partial \sigma_k}; \frac{\partial h(\sigma)}{\partial \sigma_j} \right) + b_2 \left(v, \hat{u}; \frac{\partial^2 h(\sigma)}{\partial \sigma_j \partial \sigma_k} \right). \end{aligned} \quad (4.26)$$

Moreover,

$$\begin{aligned} \frac{\partial}{\partial \sigma_k} \left[G \left(\frac{\partial v}{\partial \sigma_j} \right) \right] &= \\ &= b \left(\frac{\partial^2 v}{\partial \sigma_j \partial \sigma_k}, \hat{u}; h(\sigma) \right) + b \left(\frac{\partial v}{\partial \sigma_j}, \frac{\partial \hat{u}}{\partial \sigma_k}; h(\sigma) \right) + b_2 \left(\frac{\partial v}{\partial \sigma_j}, \hat{u}; \frac{\partial h(\sigma)}{\partial \sigma_k} \right). \end{aligned} \quad (4.27)$$

Assuming enough regularity and using the first equality in (4.16), the definition of $L(u)$, and the linearity of L and G , we obtain:

$$\begin{aligned} L^i \left(\frac{\partial^2 \hat{u}}{\partial \sigma_j \partial \sigma_k} \right) &= \frac{\partial}{\partial \sigma_k} \left[L^i \left(\frac{\partial \hat{u}}{\partial \sigma_j} \right) \right] = \frac{\partial^2 L^i(\hat{u})}{\partial \sigma_j \partial \sigma_k} = \\ &= \frac{\partial^2 G(\hat{\sigma}^i)}{\partial \sigma_j \partial \sigma_k} = \frac{\partial}{\partial \sigma_k} \left[G \left(\frac{\partial \hat{\sigma}^i}{\partial \sigma_j} \right) \right] = G \left(\frac{\partial^2 \hat{\sigma}^i}{\partial \sigma_j \partial \sigma_k} \right). \end{aligned} \quad (4.28)$$

Therefore, from (4.28), (4.24) and (4.25) we have that:

$$\begin{aligned} & b\left(\frac{\partial^2 \hat{\sigma}^i}{\partial \sigma_j \partial \sigma_k}, \hat{u}; h(\sigma)\right) + b\left(\frac{\partial \hat{\sigma}^i}{\partial \sigma_j}, \frac{\partial \hat{u}}{\partial \sigma_k}; h(\sigma)\right) + b_2\left(\frac{\partial \hat{\sigma}^i}{\partial \sigma_j}, \hat{u}, \frac{\partial h(\sigma)}{\partial \sigma_k}\right) = \\ & = -b_2\left(\frac{\partial \hat{\sigma}^i}{\partial \sigma_k}, \hat{u}; \frac{\partial h(\sigma)}{\partial \sigma_j}\right) - b_2\left(\hat{\sigma}^i, \frac{\partial \hat{u}}{\partial \sigma_k}, \frac{\partial h(\sigma)}{\partial \sigma_j}\right) - b_2\left(\hat{\sigma}^i, \hat{u}, \frac{\partial^2 h(\sigma)}{\partial \sigma_j \partial \sigma_k}\right), \end{aligned} \quad (4.29)$$

and from (4.28), (4.26) and (4.27) we obtain that:

$$\begin{aligned} & b\left(\frac{\partial \hat{\sigma}^i}{\partial \sigma_k}, \frac{\partial \hat{u}}{\partial \sigma_j}; h(\sigma)\right) + b\left(\hat{\sigma}^i, \frac{\partial^2 \hat{u}}{\partial \sigma_k \partial \sigma_j}; h(\sigma)\right) + b_2\left(\hat{\sigma}^i, \frac{\partial \hat{u}}{\partial \sigma_j}, \frac{\partial h(\sigma)}{\partial \sigma_k}\right) = \\ & = -b_2\left(\frac{\partial \hat{\sigma}^i}{\partial \sigma_k}, \hat{u}; \frac{\partial h(\sigma)}{\partial \sigma_j}\right) - b_2\left(\hat{\sigma}^i, \frac{\partial \hat{u}}{\partial \sigma_k}, \frac{\partial h(\sigma)}{\partial \sigma_j}\right) - b_2\left(\hat{\sigma}^i, \hat{u}, \frac{\partial^2 h(\sigma)}{\partial \sigma_j \partial \sigma_k}\right). \end{aligned} \quad (4.30)$$

Combining equations (4.28), (4.29) and (4.30), we conclude:

$$\begin{aligned} [\mathcal{H}_{L\sigma}]_{jk}^i & = \frac{\partial^2 L^i(\hat{u})}{\partial \sigma_j \partial \sigma_k} = \\ & = -b_2\left(\frac{\partial \hat{u}}{\partial \sigma_j}, \hat{\sigma}^i, \frac{\partial h(\sigma)}{\partial \sigma_k}\right) - b_2\left(\hat{u}, \frac{\partial \hat{\sigma}^i}{\partial \sigma_j}, \frac{\partial h(\sigma)}{\partial \sigma_k}\right) - b_2\left(\hat{u}, \hat{\sigma}^i, \frac{\partial^2 h(\sigma)}{\partial \sigma_j \partial \sigma_k}\right). \end{aligned} \quad (4.31)$$

The evaluation of second-order derivatives using the above formula requires integrating a function that depends upon the exact solutions and first-order derivatives of the forward direct and adjoint problems. Solutions $\hat{u}, \hat{\sigma}^i$ are already available. In order to evaluate the first-order derivatives $\hat{u}_{\sigma_j} := \frac{\partial \hat{u}}{\partial \sigma_j}$, and $\hat{\sigma}_{\sigma_j}^i := \frac{\partial \hat{\sigma}^i}{\partial \sigma_j}$, we may employ equations (4.19) and (4.21) and solve the following two FE problems for each unknown of the IP $j = 1, \dots, M$:

$$\begin{aligned} \text{Find } \hat{\sigma}_{\sigma_j}^i \text{ such that: } & b\left(\hat{\sigma}_{\sigma_j}^i, u; h(\sigma)\right) = L_{\sigma_j}^i(u) \quad \forall u, \\ \text{Find } \hat{u}_{\sigma_j} \text{ such that: } & b\left(v, \hat{u}_{\sigma_j}; h(\sigma)\right) = G_{\sigma_j}(v) \quad \forall v, \end{aligned} \quad (4.32)$$

where

$$L_{\sigma_j}^i(u) = -b_2\left(\hat{\sigma}^i, u; \frac{\partial h(\sigma)}{\partial \sigma_j}\right), \quad \text{and} \quad G_{\sigma_j}(v) = -b_2\left(v, \hat{u}; \frac{\partial h(\sigma)}{\partial \sigma_j}\right). \quad (4.33)$$

At first glance, solving FE problems (4.32) may seem computationally expensive. However, if we employ the same discretization spaces when solving for $\hat{u}, \hat{u}_{\sigma_j}, \hat{\sigma}^i$, and $\hat{\sigma}_{\sigma_j}^i$, then (for a given experiment) the stiffness matrix associated with problem (3.26) is the same as the stiffness matrix associated with problems (3.27) and (4.32). Therefore, once we have performed the LU factorization of the stiffness matrix associated with problem (3.26), solving problems (3.27) and (4.32) reduces to performing multiple backwards substitutions (one for each right-hand side). The number of right-hand sides needed to solve (4.32) is twice the number of unknowns of the IP, which is expected to be much smaller than

the number of unknowns needed to solve the forward problems. As a result, the cost of solving (4.32) and computing the Hessian matrix becomes often a small fraction (1-10%) of the total cost required to solve the forward problems.

4.3.3 Solution Methods

We have already stated our problem as a COP with simple bounds. There are plenty of methods well-suited for solving this kind of problems. Among those, we decided to employ the L-BFGS-U method, which is especially suitable for simple bounded problems.

Broyden, Fletcher, Goldfarb, and Shanno (L-BFGS-U) Method

We employ a FORTRAN implementation [170] of this method. It is a quasi-Newton method, which avoids to explicitly compute the Hessian by employing the limited-memory BFGS approximation updating formula [94, 24]. Since the Hessian of the cost functional is not required, this method is useful for large scale problems in which the Hessian is dense or difficult to compute. This use of the limited memory BFGS matrices to approximate the Hessian of the cost functional makes this algorithm different from those proposed in [91] and [31]. Another difference comes from the use of line searches instead of trust regions.

Active set (AS) methods [95] consist in making a guess of the active set \mathcal{A} , and then solve a sequence of linear or quadratic approximations of (4.2). For the obtained stationary point, one analyzes whether there exists or not a solution for the current AS satisfying the KKT conditions. If there exists, the point is accepted as the solution, and otherwise, the entire process is repeated selecting a different working set.

Because of the slow changes in the AS, usually by a single index at each iteration, AS methods may require multiple iterations to converge on large-scale problems. The GP method [19, 48, 32, 78, 91] tries to overcome this issue and allows rapid variations from iteration to iteration in the active set, being, in particular, especially efficient for bound constrained problems. It works as follows:

BUILD A QUADRATIC MODEL OF THE COST FUNCTIONAL AT EACH ITERATION m_k :

$$\varphi^{(n)}(m) = C(m^{(n)}) + \nabla C^T(m^{(n)})\delta m^{(n)} + \frac{1}{2}(\delta m^{(n)})^T B_k(m^{(n)})\delta m^{(n)}. \quad (4.34)$$

Here, B_k corresponds to the positive definite limited BFGS approximation of the Hessian evaluated at $m^{(n)}$. These matrices do not require a large amount of memory, and the computational cost is similar to that required in the limited memory algorithm (L-BFGS, described in [79, 47]) for unconstrained problems.

The Hessian is approximated from the curvature information encountered only on the most recent iterations, which allows memory storage.

COMPUTATION OF THE SEARCH DIRECTION IN TWO STEPS (MINIMIZING (4.34)):

In order to find the search direction, we perform the following two steps:

- Identify the set of active bounds using the GP method:

First, the AS is defined. To do this, the steepest descend direction has to be projected into the feasible box (defined by the bounds in (4.5)). The i -th component of the projection of an arbitrary point m onto the feasible region $m_l \leq m \leq m_u$ is given by

$$[P(m, m_l, m_u)]_i = \begin{cases} m_{l_i} & \text{if } m_i < m_{l_i}, \\ m_i & \text{if } m_i \in [m_{l_i}, m_{u_i}], \\ m_{u_i} & \text{if } m_i > m_{u_i}, \end{cases} \quad (4.35)$$

and the piecewise-linear path $m(t)$ is obtained by projecting the steepest descent direction onto the feasible region by

$$m(t) = P(m^{(n)} - t\nabla C(m^{(n)}), m_l, m_u), \quad \text{with } t > 0. \quad (4.36)$$

Now, the generalized Cauchy Point m^c is computed. It is defined as the first local minimizer of $\varphi^{(n)}(m(t))$. Then, the AS is defined as the components of m^c that are at their lower or upper bounds, namely $\mathcal{A}(m^c) = \{i : m_i^c = m_{l_i} \text{ or } m_i^c = m_{u_i}\}$.

- Approximately minimize the quadratic model with respect to the free variables:

The minimization problem is now defined as:

$$\begin{aligned} \min_m \quad & \varphi^{(n)}(m) \\ \text{subject to} \quad & m_i = m^c, \quad \forall i \in \mathcal{A}(m^c), \\ & m_{l_i} \leq m_i \leq m_{u_i}, \quad \forall i \notin \mathcal{A}(m^c). \end{aligned} \quad (4.37)$$

At least three different approaches can be considered for the subspace optimization: direct primal method based on the Sherman-Morrison-Woodbury formula, a primal iterative method using the CG method, and a direct dual method using Lagrange multipliers. The direct primal method is selected in this implementation, since numerical tests [170] indicate that the primal and dual methods perform similarly, while the performance of primal CG is worse. The obtained approximate solution is denoted by $\bar{m}^{(k+1)}$ and the search direction is defined as $\delta m^{(n)} = \bar{m}^{(n+1)} - m^{(n)}$.

COMPUTATION OF THE STEP SIZE: A line search along the search direction is performed. The new iterate $m^{(k+1)}$ is computed by a line search along $\delta m^k = \bar{m}^{(n+1)} - m^{(n)}$. Since B_k is positive definite, this direction corresponds to a descending direction. This line search ensures that each new iterate remains in the feasible region. The new iterate has to satisfy the sufficient decrease condition

$$C(m^{(n+1)}) \leq C(m^{(n)}) + \eta \lambda^k \nabla C^T(m^{(n)}) \delta m^{(n)}, \quad (4.38)$$

where λ^k is the step length and $\eta > 0$ a parameter, and also attempts to fulfill the curvature condition defined as

$$|\nabla C^T(m^{(n+1)})\delta m^{(n)}| \leq \vartheta |\nabla C^T(m^{(n)})\delta m^{(n)}|, \quad (4.39)$$

where $\vartheta > 0$ is a parameter. As suggested in [23], we employ $\eta = 10^{-4}$ and $\vartheta = 0.9$.

Once it is computed, the gradient is evaluated and a new $B_k(m^{(k+1)})$ is obtained. The routine that performs this line search is described in [90] and attempts to enforce conditions (4.38) and (4.39) by a sequence of polynomial interpolations.

The entire process is repeated until the convergence test is satisfied, which is defined as:

$$\|P(m^{(n)} - \nabla C(m^{(n)}), l, u)\| < \epsilon. \quad (4.40)$$

where ϵ is the tolerance.

For additional details about some of the existing methods to solve (4.37), we refer to [23].

4.4 NEW APPROACH: DIMENSIONALLY ADAPTIVE INVERSION

The dimensionality analysis of MT data is an ongoing and prevalent matter of study. Different works provide a criteria to discern when the MT data corresponds to a 1D, 2D or 3D problem. We highlight the contributions of Weaver et al. [165], who presented a dimensionality study based on the rotational invariants of the MT tensor, and the more recent work of Martí et al. [85], who based on this rotational invariants, implemented a software that provides a robust description of the dimensionality of the problem when dealing with real measurements.

In some scenarios, the dimension of the formation is unclear. Moreover, sometimes it is possible to interpret 3D MT data as 2D (see, for instance, [76] and [75]). Traditional inversion techniques usually select one fixed dimension (the full 2D (or 3D) problem) for both, the forward simulations and the inversion.

However, a good dimensionality study of the problem may indicate some zones where the problem is fully 2D (or 3D), while others where a 1D (or 2D) consideration of the problem may be sufficient. Based on this idea, we propose an inversion algorithm that takes advantage of this scenario.

In this dissertation, we first consider a full 1D IP, with an already known forward analytical solution (see section 3.1), and after that, we introduce this 1D IP solution into the 2D IP. That is:

- In the first step, we solve the IP for a 1D background model consisting of a layered media. From here, we obtain \hat{m}_{1D} , the solution of the 1D IP. Notice that the corresponding forward solution is inexpensively computed analytically.

- After that, incorporate the 1D solution into the 2D IP by defining the 1D solution as the initial solution of the 2D problem and/or via the regularization term $R(m)$ by defining

$$R(m) = \|m - \hat{m}_{1D}\|_{L^p(\Omega)}, \quad (4.41)$$

where p is usually 1 or 2.

- Finally, we solve the full 2D IP. To do so, we can employ the full field or the secondary field based formulation, which is computationally more inexpensive.

The main advantages of this approach are:

- We can study separately 1D and 2D effects in the IP.
- The inversion process is faster. Being each of the direct computations cheaper, the IP is also computationally faster.
- The 1D IP has less unknowns and is more stable. Employing this information in the 2D problem, we increase the robustness of the algorithm.
- If we employ the secondary field formulation to solve the direct problem, since we only need to accurately solve the secondary field variations in the forward simulations, which in general are more localized than the total fields, the numerical computation of the QoI is often faster and more accurate [1].

IMPLEMENTATION DETAILS

This chapter provides a description of the software package developed during this dissertation. It is implemented in FORTRAN90, and we can differentiate two main parts: the *hp*-FEM solver of the direct problem to simulate MT measurements, and the software related to the inversion of those measurements.

For the direct solver, we have developed a software based on an extension of the work performed by Demkowicz [37] in the context of goal-oriented *hp*-FEM, which incorporates a self-adaptive goal-oriented strategy for the construction of the *optimal* mesh. This software employs quadrilateral elements and integrated Legendre hierarchical polynomials as shape functions [145]. Apart from supporting anisotropic *h* and *p*-refinements, it also performs automatic *hp*-refinements. We have added a MT module to the software, which stores and handles all the information about the physical problem under consideration; that is, the physical domain, its geometry, the values of the conductivity everywhere, the frequency, the considered mode (TE, TM mode, or both at the same time), the formulation type (full or secondary field formulation), and all information regarding the PML and the inputs/outputs.

We have implemented the inversion software independently. All the information related to the inversion is managed and stored on its corresponding kernel, and it is possible to easily switch from one optimization method to another (if implemented) with a simple flag. To evaluate the cost functional and its gradient, we need to compute the QoI and its derivatives. To do so, we solved both the forward direct and adjoint problems. We have designed an interface to share this information between the two kernels, and we have implemented an specific routine to compute the gradient of the cost functional.

5.1 STRUCTURE AND MAIN FEATURES

Figure 5.1 describes the structure of the software. Its main components are:

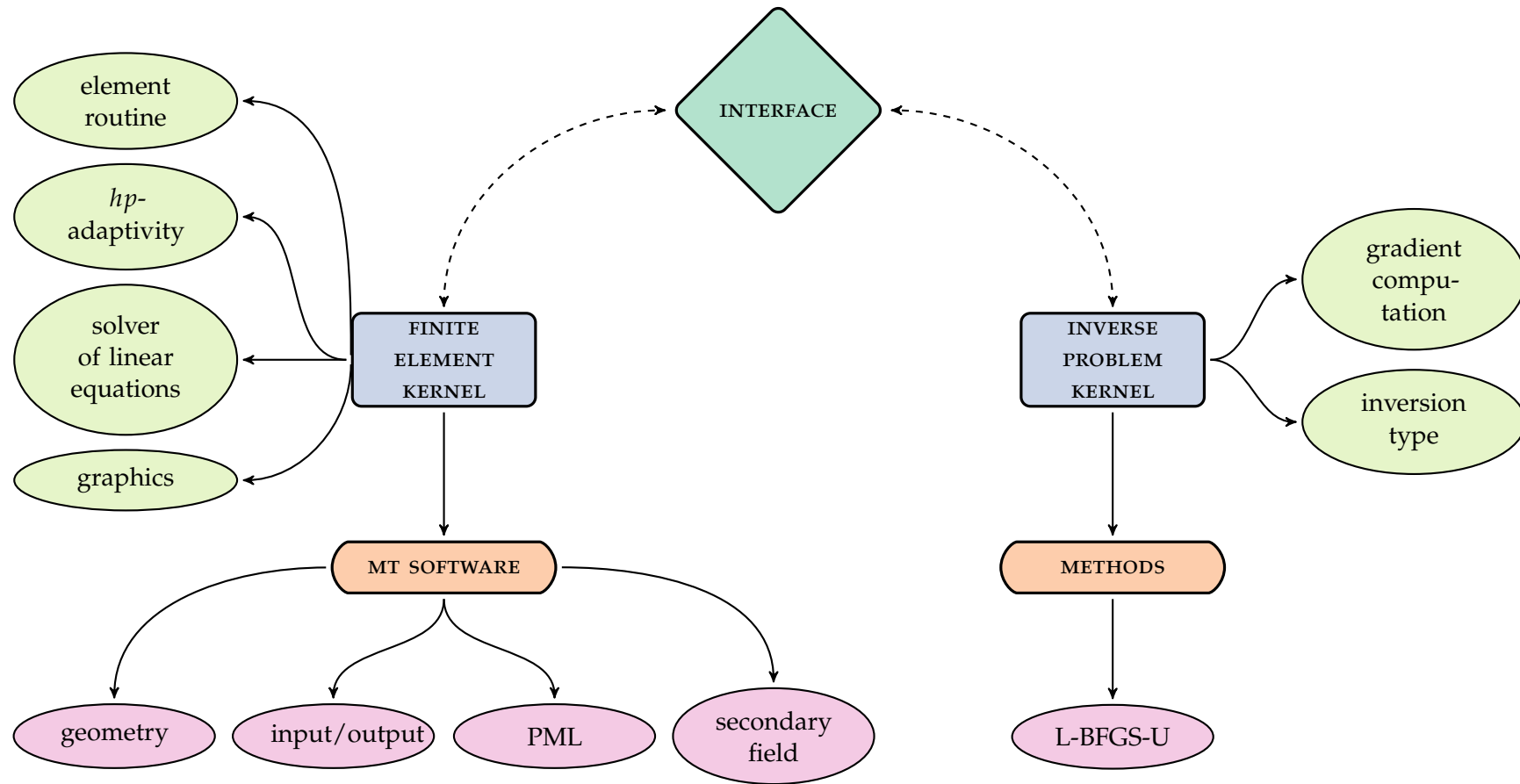


Figure 5.1: Structure of the implemented software.

THE MT SIMULATION SOFTWARE:

This part of the software handles and stores the following information:

- Geometry definition: The self adaptive process of the mesh generation needs an initial *sufficiently good* mesh to converge. We define it by employing rectangular elements obtained from tensor products of the coordinates. At the same time, we also define the size and the mesh for the PML. The mesh needs to be conforming to the material discontinuities, and therefore we always make any boundary of a material, receivers, or source coincide with the boundary of one (or more) elements. This facilitates the integration process and avoids approximation and stability problems.
- Input/output: Given the initial mesh, we need the following information to solve a forward direct problem:
 - Material properties: resistivity and position.
 - Frequency.
 - Formulation type.
 - Desired QoI.
 - Set the use of the PML. If yes, provide a value to α in (2.39).
- PML: We have implemented an automatically adaptive PML for truncation of the computational domain. We interpret a PML as a change of variables in the complex plane that for the electromagnetic fields yields to the same variational formulations with different materials. Since the source is always outside the PML region, for implementation purposes, no variations are needed in the forcing term. The modifications in the element routine to implement the PML are:
 - Check whether an element is in the PML region or not.
 - If yes, compute the new materials.
 - To compute the new materials, automatically calculate the value of β in Equation (2.39).
- Secondary field formulation: To solve the secondary field, we employ the variational formulation given by (2.30) and (2.31). They both have the same structure than the ones for the total fields, except for the right hand side. The new right hand sides appearing on the secondary field formulation, incorporate the primary field solution and its derivative with respect to z . We analytically compute them using the solution described by Chew in the second chapter of book [28]. From the implementation point of view, we only need to modify the element routine. Thus, we incorporate a flag that allows us to switch between the new right hand sides and the original ones. If we employ a PML, we also need to compute the new materials, which in this case also appear in the forcing term.

THE FEM SOFTWARE:

The main ingredients of the hp -FEM software are:

- The element routine: Most FE codes perform a loop through the elements, calculate the contribution of each of them to the stiffness matrix and/or the load vector by performing the corresponding integrals, and assemble these contributions afterwards. The routine intended to compute these contributions (integrals) corresponds to the element routine, the core routine of most FE codes. We use piecewise polynomials as basis functions, and consistently, we employ a Gaussian quadrature rule that procures exact results to compute the integrals.
- The hp -adaptivity algorithm: The adaptive process is based on an interplay between two meshes: the current coarse mesh and a fine mesh, which is obtained from the coarse one through a global hp -refinement. Then, the problem is solved in both meshes. The fine grid is used to guide optimal hp -refinements over the coarse grid (see [43] for details).

When performing adaptive h -refinements, *constrained (hanging) nodes* appear. A constrained node is a *phantom* node, in the sense that it is not associated with a global degree of freedom of the problem. The value of the solution there depends upon the value of the solution in neighboring nodes. Figure 5.2 (a) illustrates a typical situation where, as a result of an h -refinement, one big element has two smaller neighbors. The vertex node that lies in the interior of the big element edge, and the two middle edge nodes lying on the small element edges, are constrained nodes. The nodes lying on the big element edge are identified as the parent nodes of the constrained nodes. We employ the *1-irregularity rule* [41] to guarantee that parent nodes of constrained nodes are themselves always unconstrained. This allows refinements as in Figure 5.2 (b), but prevents refinements such as the ones described in Figure 5.2 (c).

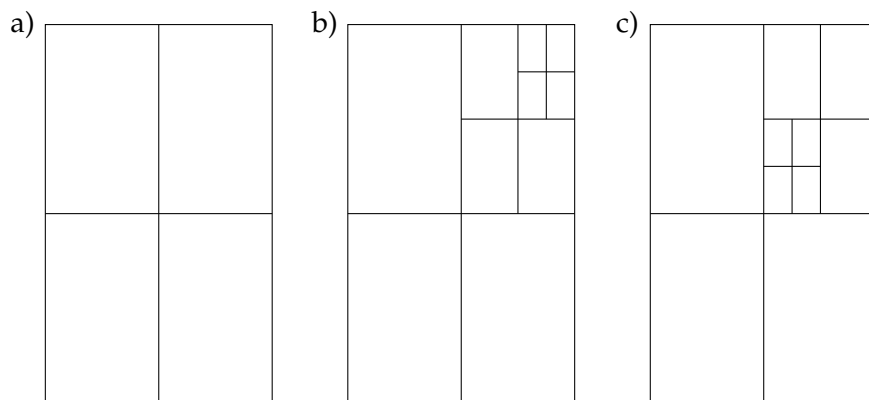


Figure 5.2: Illustration of different h -refinements.

- The solver of linear equations: While the use of iterative solvers typically requires lower computational resources (time and memory) than direct solvers (see Table 5.1),

they suffer from a number of problems. First, iterative solvers often present severe convergence issues. Thus, different solvers are needed for each application (elasticity [44], electromagnetism [57], fluid dynamics [3]) and numerical method (h -FEM [21], p -FEM [5], hp -FEM [107, 108], etc.). Second, in addition to the convergence problems, iterative solvers may be slower than direct solvers when a problem with multiple right hand side needs to be solved, as in our case. Hence, we employ

Scalability	Direct Solver	Iterative Solver
CPU Time	$\mathcal{O}(N^2b) + \mathcal{O}(NMb)$ LU fact. + Backward Subst.	$\mathcal{O}(n^2b) + \mathcal{O}(MNbc)$ Preconditioner + Iter. Solution
Memory	$\mathcal{O}(Nsb)$	$\mathcal{O}(Nb)$

Table 5.1: Resource consumption of different solvers in 3D. N is the problem size, b is the (average) bandwidth of the matrix, M is the number of right-hand sides, s is a constant that depends upon the structure of the matrix, and can be as large as N , n is the size of the preconditioner, and c is a constant that depends upon the condition number of the matrix and the choice of preconditioner.

the direct solver MUMPS (“MUltilfrontal Massively Parallel Solver”) [92] as an external library. It is a package for solving systems of linear equations of the form $Ax = b$, where A is a square sparse matrix that can be either unsymmetric, symmetric positive definite, or symmetric. It is based on a multifrontal approach which performs a direct factorization $A = LU$ or $A = LDL^T$ depending on the symmetry of the matrix and exploits parallelism arising from both, sparsity in the matrix A and from dense factorizations kernels. Thus, we factorize the stiffness matrix only once, and problems with different right hand sides (rhs) reduce to performing multiple backwards substitutions (one for each right-hand side). For a recent survey on direct solvers, we refer to [112].

- The graphics package: This software incorporates a package that draws a color representation of the FE mesh with a reference color scale. The different colors correspond to different orders of approximation. It also displays the numerical solution (and the exact one if available) allowing to zoom at any region of the computational domain.

THE INVERSION SOFTWARE:

We implemented a kernel that stores all information about the inverse problem.

- Gradient computation: We employ the representation theorem (see section 4.3.2) to efficiently compute the gradient of the cost functional once the forward direct and adjoint problems are solved.
- Inversion type: We include a flag to change between the TE mode, the TM mode, and the joint TE+TM modes to perform the inversion.

- **Solution methods:** We incorporate a flag to easily switch between the different possibly implemented algorithms. In this dissertation we only consider the L-BFGS-U method.

5.2 IMPLEMENTATION OF THE FORWARD DIRECT AND ADJOINT PROBLEMS:

Algorithms 5.1 and 5.2 describe the pseudocode used to solve the forward direct and adjoint problems with the *hp*-FEM, respectively.

Algorithm 5.1 Computation of the direct forward problem.

procedure SOLVE (3.26)

Step 0: *Define the problem information:*

- Define the *hp*-grid.
- Define the materials and frequency.

Step 1: *Compute the linear QoI:*

- Assemble the stiffness matrix.
- Assemble the right hand side.
- Solve the linear system of equations.
- Compute the linear quantity of interest (equation (2.59)).

Step 2: *Compute the impedance as QoI:*

if (impedance is needed) **then**

- Postprocess the corresponding field from Maxwell's equations.
- Compute the impedance (equation (4.7)).

end if

end procedure

5.3 IMPLEMENTATION OF THE INVERSE SOLVER

We describe the main implementation features of the inverse solver.

5.3.1 Computation of the Jacobian

We start explaining how the derivatives of the linear QoI are computed, that is, the terms $[\mathcal{J}_{L\sigma}]_j^i$ in equation (4.14). Let a general bilinear form $b(v, u)$ be written as follows (equation (4.17)):

$$b(v, u) := b(v, u; h(\sigma)) = b_1(v, u) + b_2(v, u; h(\sigma)), \quad (5.1)$$

where, b , b_1 and b_2 are sesquilinear forms in the first two variables, b_2 is linear in the third variable h , and b_1 is independent of h , a function that depends on the considered mode, being $h = h_{TE}$ for the TE mode and $h = h_{TM}$ for the TM mode.

Algorithm 5.2 Computation of the forward adjoint problems.

procedure SOLVE (3.26) AND (3.27)

Step 0: Define the problem information:

- Define the hp -grid.
- Define the materials and frequency.

Step 1: Solve the forward problem (3.26) (see Algorithm 5.1):

- Compute the forward direct problem.
the stiffness matrix is assembled and the LU factorization performed.

Step 2: Solve the forward adjoint problems (3.27):

loop through receivers

for ($irec = 1 \rightarrow$ Number of receivers) **do**

- Compute and assemble the right hand side for the $irec$ -th receiver.
- Employ the same stiffness matrix than for the forward problem.
- Solve the linear system of equations with the new rhs.
the stiffness matrix is already factorized, hence, each problem reduces to performing a new backward substitution.

end for

end procedure

Let the direct problem (D) and its adjoint problem (A) be defined as:

$$D : \text{ Find } \hat{u} \in V, \text{ such that } b(v, \hat{u}) = G(v), \quad \forall \hat{u}, v \in V, \quad (5.2)$$

$$A : \text{ Find } \hat{v} \in V, \text{ such that } b(\hat{v}, u) = P(u), \quad \forall u, \hat{v} \in V, \quad (5.3)$$

where in both cases $v = F$ and $V = H_0^1 = \{v \in L^2(\Omega) : v|_{\Gamma_D} = 0, \nabla v \in L^2(\Omega)\}$. For the two 2D uncoupled modes we have that:

- TE Mode:

$$\left\| \begin{aligned} \hat{u} &= E_y, \\ G(F) &= -j\omega \langle F, J^{imp} \rangle_{L^2(\Omega)}, \\ b_1(F, E_y) &= -\langle \nabla F, \mu^{-1} \nabla E_y \rangle_{L^2(\Omega)}, \\ b_2(F, E_y; h_{TE}(\sigma)) &= -\langle F, h_{TE}(\sigma) E_y \rangle_{L^2(\Omega)}, \\ h_{TE}(\sigma) &= \omega^2 \varepsilon - j\omega \sigma. \end{aligned} \right. \quad (5.4)$$

- TM Mode:

$$\begin{aligned}
 \hat{u} &= H_y, \\
 G(F) &= -\langle F, M^{imp} \rangle_{L^2(\Omega)}, \\
 b_1(F, H_y) &= j\omega \langle F, \mu H_y \rangle_{L^2(\Omega)}, \\
 b_2(F, H_y; h_{TM}(\sigma)) &= -\langle \nabla F, h_{TM}(\sigma) \nabla H_y \rangle_{L^2(\Omega)}, \\
 h_{TM}(\sigma) &= \frac{1}{\sigma + j\omega\varepsilon}.
 \end{aligned} \tag{5.5}$$

For simplicity in the notation, in this section we employ the formulations without the new materials arisen from the PML. However, it is straightforward to consider the PML by only switching the materials with the new ones defined in Chapter 2.

TE MODE:

We define the following two linear operators associated to each receiver:

$$L^i(u) = \frac{1}{|\Omega_{R^i}|} \int_{\Omega_{R^i}} u \, d\Omega, \tag{5.6}$$

$$L_{TE}^i(u) = \frac{1}{j\omega\mu|\Omega_{R^i}|} \int_{\Omega_{R^i}} \frac{\partial u}{\partial z} \, d\Omega. \tag{5.7}$$

- If $P(u) = L^i(u)$:

$$D : b(v, \hat{u}) = G(v), \quad \forall v \in V, \tag{5.8}$$

$$A : b(\hat{v}_E^i, u) = L^i(u), \quad \forall u \in V. \tag{5.9}$$

From (5.8) we obtain the solution for $\hat{E}_y = \hat{u}$, and we compute the associated linear QoI as $L^i(\hat{E}_y)$. By solving (5.9) we obtain the solution for \hat{v}_E^i . Since (5.8) stands for all v , in particular it is also valid for \hat{v}_E^i , and therefore we have that:

$$b(\hat{v}_E^i, \hat{E}_y) = G(\hat{v}_E^i) = L^i(\hat{E}_y). \tag{5.10}$$

From this expression and employing equations (5.4) we obtain that:

$$\frac{\partial L^i(\hat{E}_y)}{\partial \sigma_j} = -b_2(\hat{v}_E^i, \hat{E}_y; \frac{\partial h_{TE}(\sigma)}{\partial \sigma_j}) = \langle \hat{v}_E^i, \hat{E}_y \rangle_{L^2(\Omega)}. \tag{5.11}$$

- If $P(u) = L_{TE}^i(u)$:

$$D : b(v, \hat{u}) = G(v), \quad \forall v \in V, \tag{5.12}$$

$$A : b(\hat{v}_H^i, u) = L_{TE}^i(u), \quad \forall u \in V. \tag{5.13}$$

Since \hat{E}_y is already computed, from Maxwell's equations we have that

$$L^i(\hat{H}_x) = L_{TE}^i(\hat{E}_y). \quad (5.14)$$

Following the same argument, solving equation (5.13) we obtain the solution for $\hat{\vartheta}_H^i$ and then

$$b(\hat{\vartheta}_H^i, \hat{E}_y) = G(\hat{\vartheta}_H^i) = L_{TE}^i(\hat{E}_y), \quad (5.15)$$

is satisfied. From this expression and employing equations (5.4) we obtain that:

$$\frac{\partial L^i(\hat{H}_x)}{\partial \sigma_j} = \frac{\partial L_{TE}^i(\hat{E}_y)}{\partial \sigma_j} = -b_2(\hat{\vartheta}_H^i, \hat{E}_y; \frac{\partial h_{TE}(\sigma)}{\partial \sigma_j}) = \langle \hat{\vartheta}_H^i, \hat{E}_y \rangle_{L^2(\Omega)}. \quad (5.16)$$

TM MODE:

We define the following linear operator:

$$L_{TM}^i(u) = \frac{1}{(\sigma + j\omega\varepsilon)|\Omega_{R^i}|} \int_{\Omega_{R^i}} \frac{\partial u}{\partial z} d\Omega. \quad (5.17)$$

• If $P(u) = L^i(u)$:

$$D : b(v, \hat{u}) = G(v), \quad \forall v \in V, \quad (5.18)$$

$$A : b(\hat{\vartheta}_H^i, u) = L^i(u), \quad \forall u \in V. \quad (5.19)$$

From (5.18) we obtain the solution for $\hat{H}_y = \hat{u}$, and we compute the associated linear QoI as $L^i(\hat{H}_y)$. By solving (5.19) we obtain the solution for $\hat{\vartheta}_H^i$. Since (5.18) stands for all v , in particular it is also valid for $\hat{\vartheta}_H^i$, and therefore we have that:

$$b(\hat{\vartheta}_H^i, \hat{H}_y) = G(\hat{\vartheta}_H^i) = L^i(\hat{H}_y). \quad (5.20)$$

From this expression and employing equations (5.5) we obtain that:

$$\frac{\partial L^i(\hat{H}_y)}{\partial \sigma_j} = -b_2(\hat{\vartheta}_H^i, \hat{H}_y; \frac{\partial h_{TM}(\sigma)}{\partial \sigma_j}) = -\langle \nabla \hat{\vartheta}_H^i, \frac{1}{(\sigma_j + j\omega\varepsilon)^2} \nabla \hat{H}_y \rangle_{L^2(\Omega)}. \quad (5.21)$$

• If $P(u) = L_{TM}^i(u)$:

$$D : b(v, \hat{u}) = G(v), \quad \forall v \in V, \quad (5.22)$$

$$A : b(\hat{\vartheta}_E^i, u) = L_{TM}^i(u), \quad \forall u \in V, \quad (5.23)$$

Since \hat{H}_y is already computed, from Maxwell's equations we have that

$$L^i(\hat{E}_x) = L_{TM}^i(\hat{H}_y). \quad (5.24)$$

Following the same argument, solving equation (5.23) we obtain the solution for $\hat{\vartheta}_E^i$ and then

$$b(\hat{\vartheta}_E^i, \hat{H}_y) = G(\hat{\vartheta}_E^i) = L_{TM}^i(\hat{H}_y), \quad (5.25)$$

is satisfied. Now $L_{TM}^i(\hat{H}_y)$ depends on σ and therefore, instead of equation (4.23) we have that

$$\begin{aligned} \frac{\partial L^i(\hat{E}_x)}{\partial \sigma_j} &= \frac{\partial L_{TM}^i(\hat{H}_y)}{\partial \sigma_j} = -b_2(\hat{\vartheta}_E^i, \hat{H}_y; \frac{\partial h_{TM}(\sigma)}{\partial \sigma_j}) + \frac{\partial h_{TM}(\sigma)}{\partial \sigma_j} \int_{\Omega_{R^i}} \frac{\partial \hat{H}_y}{\partial z} d\Omega \\ &= -\langle \nabla \hat{\vartheta}_E^i, \frac{1}{(\sigma_j + j\omega\varepsilon)^2} \nabla \hat{H}_y \rangle_{L^2(\Omega)} - \frac{1}{(\sigma_j + j\omega\varepsilon)^2} \int_{\Omega_{R^i}} \frac{\partial \hat{H}_y}{\partial z} d\Omega, \end{aligned} \quad (5.26)$$

where we have also employ equations (5.5). This new term is 0 for the domains where $\Omega_{R^i} \cap \Omega_{\sigma_j} = \emptyset$. Notice that a similar modification is necessary when computing second derivatives.

5.3.2 Inversion Algorithms

A traditional approach to solve a 2D MT inverse problem is to consider the 2D problem with all the model parameters, the full field formulation for the direct problem, and then solve the corresponding inverse problem. Alternatively, we can use a dimensionally adaptive strategy and employ the secondary field formulation to solve the direct problem. In Algorithm 5.3 we show the pseudocode for solving a typical inverse problem when a traditional approach is employed, while algorithm 5.4 illustrates an inverse problem solution process based on the dimensionally adaptive strategy.

5.3.3 Implementation of the L-BFGS-U

This method is implemented using double precision under FORTRAN in a software package called L-BFGS-U [170]. As a limited-memory variable metric method, the number of iterations needed to converge grows rapidly as the number of variables increase. Algorithm 5.5 illustrates the pseudocode of the L-BFGS-U method.

When employing this software, the user has to estimate and provide the following quantities:

- The cost functional $C(m)$ and its gradient, $\nabla C(m)$.
- The amount of storage required by L-BFGS-U. This number can be estimated by selecting a parameter which defines the number of saved BFGS corrections. A number between 3 and 20 is recommended. We use 10 saved BFGS corrections.
- The stopping criteria. There are two different tests that can be selected by the user. The first one is designed to terminate the execution when the variations in the objective function are sufficiently small. The second one terminates the execution when the l^∞ -norm of the projected gradient becomes sufficiently small.

Algorithm 5.3 Solve the traditional inverse problem.

procedure MINIMIZE (4.2)

Step 0: *Obtain the data:*

if (real measurements available) **then**

- Process the measurements and obtain the data .

else (solve the synthetic problem)

- $m = \hat{m} \rightarrow$ Set the solution of the inverse problem for the synthetic problem.

- Define the hp -grid.

- Simulate the data:

* Compute the forward problem (3.26).

* $d^i = g^i(\hat{u}(\hat{m}))$.

end if

Step 1: *Solve the optimization problem (4.5):*

$m^0 = m_0 \rightarrow$ Set a feasible starting point

$k = 1 \rightarrow$ First iteration.

while (m^k does not satisfy the stopping criteria) **do**

repeat (*here employ the desired optimization method: L-BFGS-U*)

- Compute the forward and adjoint problems with Algorithm 5.2

- Compute the Jacobian (4.23)

- Compute the cost functional (4.2)

- $k = k + 1$

until (the optimization method converges)

end while

Result: $\hat{m} = m^k$

end procedure

Algorithm 5.4 Solve the inverse problem using a DAM

procedure MINIMIZE (4.2)**Step 0:** *Obtain the data:***if** (real measurements available) **then**

- Process the measurements and obtain the data.

else (solve the synthetic problem)- $m = \hat{m} \rightarrow$ Set the solution of the inverse problem for the synthetic problem.- Define the hp -grid.

* Compute the forward problem (3.26).

* $d^i = g^i(\hat{u}(\hat{m}))$.**end if****Step 1:** *Solve the optimization problem for the 1D layered media:* $m^0 = m_0 \rightarrow$ Set a feasible starting point for the 1D problem $k = 1 \rightarrow$ First iteration.**while** (m^k does not satisfy the stopping criteria) **do****repeat** (*here employ the desired optimization method: L-BFGS-U*)

- Compute the 1D analytical solution (see Section 3.1).

- Compute the 1D Jacobian analytically.

- Compute the cost functional (4.2).

- $k = k + 1$.**until** (the optimization method converges)**end while**Result: $\hat{m}_{1D} = m^k$ **Step 2:** *Incorporate the 1D solution in the definition of the 2D inverse problem.***Step 3:** *Solve the optimization problem for the 2D problem employing the secondary field formulation for the direct forward problem (new reduced domain):* $m^0 = m_0 \rightarrow$ Set a feasible starting point for the 2D problem. $k = 1 \rightarrow$ First iteration.**while** (m^k does not satisfy the stopping criteria) **do****repeat** (*here employ the desired optimization method: L-BFGS-U*)

- Compute the forward and adjoint problems with Algorithm 5.2.

- Compute the Jacobian (4.23).

- Compute the cost functional (4.2).

- $k = k + 1$ **until** (the optimization method converges)**end while**Result: $\hat{m} = m^k$ **end procedure**

Algorithm 5.5 Pseudocode of L-BFGS-U.

procedure MINIMIZE $C(m)(m_{min}, m_{max})$ **Step 1:** *Initialize:*

- $m^0 = m_0 \rightarrow$ Set a feasible starting point.
- $k = 1 \rightarrow$ First iteration.
- Initial BFGS matrix: Identity.

Step 2: *Start the iterative process:***while** (m^k does not satisfy the stopping criteria) **do****repeat**

- Update B_k .
- Compute the quadratic approximation (4.34).
- Compute the search direction by the direct primal method.
(solve (4.37) such that it satisfies (4.38) and it is feasible).
- Perform a line search along the search direction.
- $k = k + 1$.

until (convergence test (4.40) is satisfied)**end while**Result: $\hat{m} = m^k$ **end procedure**

Different problems may arise during the course of each iteration, including:

- If after 20 evaluations of the objective function the algorithm (via the line search) is unable to find a point with a low enough value, the current direction is discarded. Then, the iteration is restarted along the steepest descent direction.
- The line search algorithm may fail along the steepest descent direction. If this occurs, the algorithm may have problems achieving high-accuracy solutions.
- The algorithm ensures that the Hessian approximation is sufficiently positive definite. However, if the search direction does not correspond to a descent direction, or the BFGS matrix (or a related submatrix) becomes singular or indefinite at some point, the iteration is restarted along the steepest descent direction.

Other important aspects of the implementation include:

- The step length parameter η in (4.38) is computed using the line search program of Moré and Thuente [90]. The parameters η and θ in (4.38) and (4.39) respectively take the values 10^{-4} and 0.9 in the code.
- It has been numerically observed that even with a sufficiently accurate function, the L-BFGS-B is sometimes unable to reduce the projected gradient in order to satisfy the stopping conditions.

 NUMERICAL RESULTS

This Chapter is devoted to the numerical results. It is organized as follows. First, we mention the general considerations of our model problems employed in this chapter. Then, we verify our 2D solver for the forward and IPs. After that, we study numerically our simulation and inversion methods. Finally, we present and analyze some relevant geophysical results. The analytical solution for the 1D problem and the numerical calculation performed with the multi-goal-oriented hp -FEM employed in this chapter are described in Chapter 3

6.1 GENERAL CONSIDERATIONS OF OUR MODEL PROBLEMS

- In this work, for simplicity we consider only synthetic problems.
 - If one wants to apply the results of this Dissertation to real measurements, a number of additional obstacles which are outside the scope of this work need to be resolved. Briefly, MT practitioners first need to explore and *clean* the recorded time series data and remove the possible defective entries (in [142] we find a typical real data example for 2D data processing and analysis). After that, they usually need to convert the time series into MT responses (see Jones et al. [69] for a description of different methods) and they have to analyze these responses for distortion effects. These effects become crucial, since they may lead to erroneous model characterization. Berdichevsky et al. [16] divided them into galvanic effects (through distributions of charges that generate electric field) and inductive effects (due to distribution of currents that generate magnetic fields). In MT surveys, the galvanic distortion is generally more important. It is typically produced by small-scale geological inhomogeneities located near the surface and usually results in a displacement of the apparent resistivity curves. This effect is known as static shift. A comparison of different methods to treat the distortion can be found in [27]. Finally, practitioners need to find the strike direction of the subsurface, which is also possible to achieve by employing different techniques such as [51, 84].
 - We simulate synthetic measurements using a highly refined mesh as follows: given a distribution of the subsurface $\hat{\rho} = \{\rho_i\}_i^M$, where $\hat{\rho}$ denotes the solution of the IP, we solve the forward direct problem (3.26) and we define $d_{obs}^i = g^i(\hat{\rho})$.

To avoid the inverse crime, the formulation that we use for this purpose is intentionally different from that employed in the inversion algorithm. Specifically, if we employ the full field formulation in the inversion, the measurements are simulated with the secondary field formulation, and vice versa. To mimic realistic measurements, we add a 3% uncorrelated random Gaussian noise to the real and imaginary parts of the simulated measurements.

- The frequency range is $(10^{-5} - 100)$ Hz, although in most simulations we restrict ourselves to the most sensitive range $(10^{-4} - 1)$ Hz.
- The relative permittivity and permeability are selected to be the same in all materials, and equal to one.
- The receivers are located along the Earth’s surface.
- In 2D problems, the medium strike direction is aligned with the coordinate system. This is a fair modeling assumption, since the MT method is typically employed in regions with prior geological knowledge of the media. Additionally, when looking for hydrocarbons, liquids typically exhibit an underlying 1D layered media structure, which we also consider here in most of our numerical examples.
- The size of the source is (2500×5) km in the x and z spatial variables and infinity in y .
- The forcing terms are $J_y^{imp} = 1$ in the TE mode and $M_y^{imp} = 1$ in the TM mode.
- We assume prior geological knowledge of the media. Thus, we consider known the location of the interfaces between layers, and we focus on determining only the value of the resistivity within each layer.
- Unless explicitly expressed otherwise, we compute the hp -grid with the multi-goal oriented adaptivity.
- The four model problems that we consider are depicted in Figure 6.1. The computational domain consists of air and a layered media for the subsurface formation. The horizontal dimension corresponds to the x spatial variable (with zero at the center), and the vertical to z (with zero on the surface). The physical domain is truncated with a PML and a Dirichlet homogeneous BC is imposed at the PML’s outer part.
- If it is not explicitly expressed, the considered different models for the resistivity distribution of Earth’s subsurface (a conductive and a resistive anomaly) are given in Table 6.1:

	ρ_1	ρ_2	ρ_3	ρ_4
Model 1	80	100	120	10
Model 2	3	2	4	200

Table 6.1: Different models for the formation of the subsurface given by Figure 6.1.

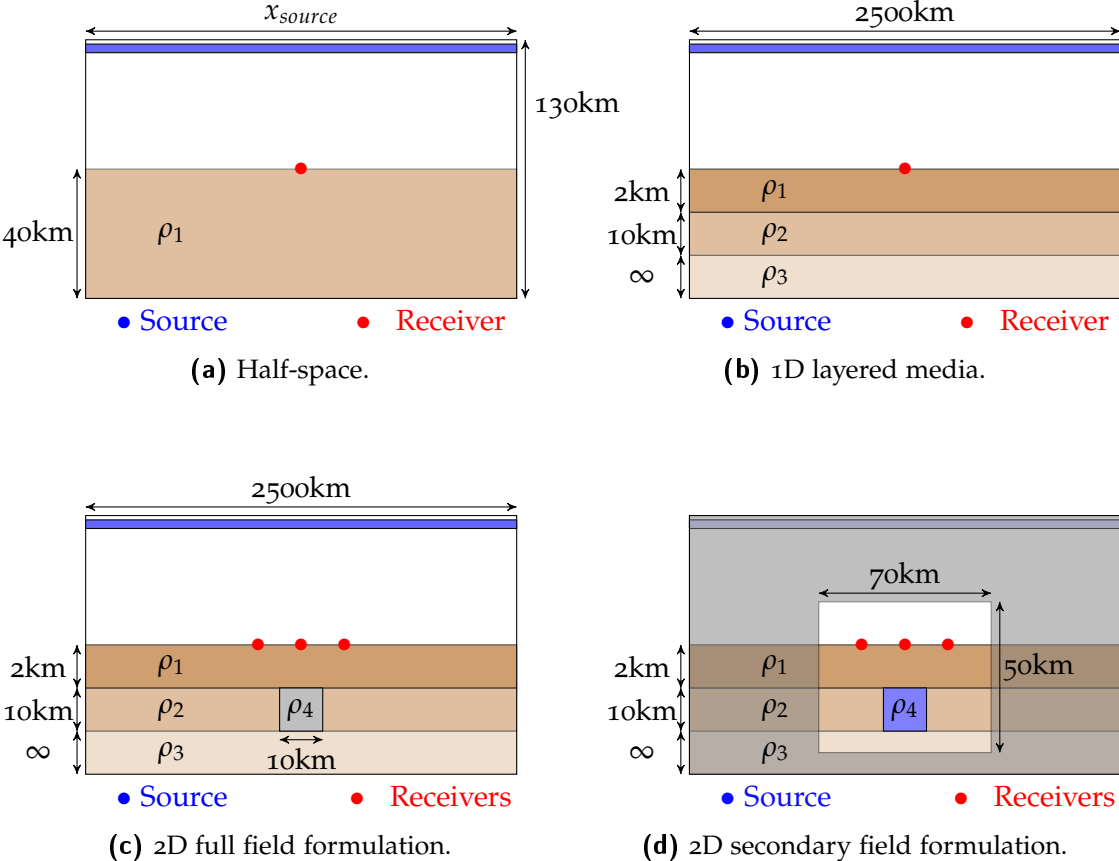


Figure 6.1: Considered Model problems.

6.2 VERIFICATION

We first verify that our forward and inverse solvers produce the intended results.

6.2.1 Forward Problem

We first establish the size of the source in order to efficiently model the nature of the incident plane wave. After that, we verify our forward simulator for the full and secondary field formulations.

Study of the Source

In MT, the source is assumed to be a plane wave traveling towards the Earth's surface. We approximate this plane wave by considering the source as a thin plate where a constant harmonic impressed electric J_y^{imp} or magnetic M_y^{imp} current are embedded. We place the source at 80 km above the surface, that is, where the ionosphere starts. We have numerically observed that the width of the plate does not significantly affect to the solution, as physically expected because we only intend to produce a plane wave starting from the ionosphere, so we set it to be equal to 5 km.

Some undesirable effects, which have a strong impact in the solution, could appear around the lateral edges of the plate. Therefore, the source has to be long enough so the edges are sufficiently far from the region of study. In fact, for lengths smaller or comparable to the height of the computational domain (approx. 100 km), we are unable to completely capture the behavior of the plane wave while it is traveling through.

To determine a valid horizontal extension of the source, we consider a homogeneous half space with an Earth resistivity equal to 10 Ohm-m, as the one depicted in Figure 6.1a. To be sure that we efficiently obtain a plane wave, we measure the solution at $x = 20$ km, that is, sufficiently far from the region of interest. In there, we compute the numerical solution for the impedance for the TE and TM modes. We compare the relative error between these numerical solutions and the corresponding analytical ones for different lengths of the source in Figure 6.2. From these results, we decide to employ a source with lateral extend in x direction equal to 2500 km in all our numerical computations. Since we employ an adaptive method, we maintain the number of unknowns under control. Hence, we prefer to employ a sufficiently large source to achieve the maximum accuracy.

Full Formulation

Our aim here is to guarantee that the hp -FEM in conjunction with the PML provides accurate results. The model problem is illustrated in Figure 6.1b. When the media is only 1D dependent (invariant in x), the solution along the surface is constant (x and y independent), and therefore, it is sufficient to consider only one receiver. We consider a 5 km thick PML, and we define an initial mesh using a geometric scaling in each direction within the PML region, as depicted in Figure 6.3. The hp -adaptive algorithm performs

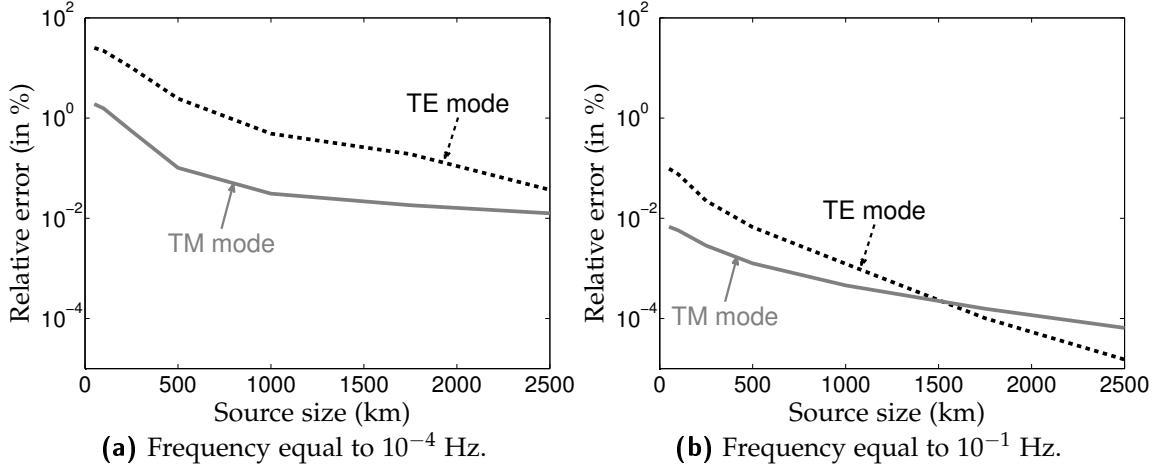


Figure 6.2: Relative error between the numerical and analytical solutions for impedance for different horizontal sizes of the source.

further refinements in that area so numerical results become as accurate as needed. In our simulations, the number of elements into the PML region typically represents approximately 15% of the total amount of elements. We define a decay factor of $\alpha = 10^{-5}$

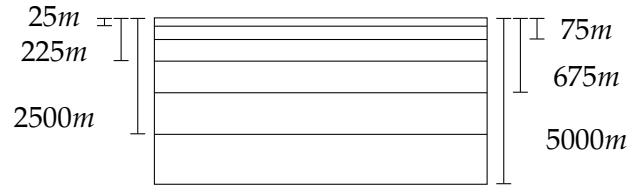


Figure 6.3: FEM mesh in an arbitrary direction within the PML region.

in equation (2.38), ensuring that the wave decays sufficiently fast before arriving to the boundary of the domain, and we analyze the four 1D model problems with known analytical solution, described in Table 6.2. In Figure 6.4 we display the relative error of the

	ρ_1	ρ_2	ρ_3
Model 1	1	1	1
Model 2	1	10	3
Model 3	1	10	10
Model 4	1	100	3

Table 6.2: Different models for the formation of the subsurface given by Figure 6.1b.

apparent resistivity at different frequencies between the numerical *hp*-FEM solution and the exact solution for the TE and TM modes. We obtain relative errors below 1%, a superb accuracy for these type of simulations.

Secondary Field Formulation

We now validate the forward solver for the secondary field formulation. The considered 2D scenario, for the full and secondary field formulations, are illustrated in Figures 6.1c

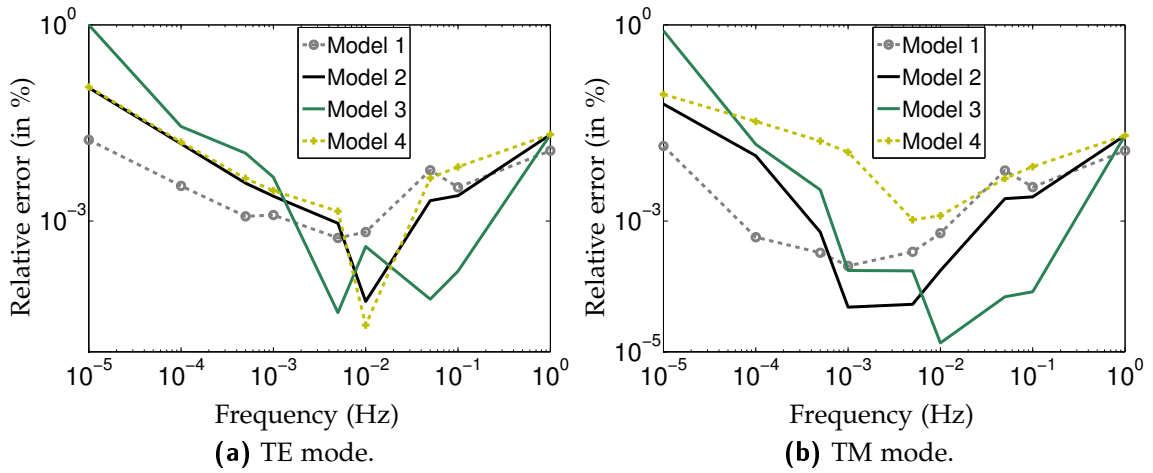


Figure 6.4: Relative error between the apparent resistivity obtained with the exact and numerical solutions for different subsurface formations against frequency for the TE and TM modes.

and 6.1d, respectively. For the former, we still have the same forcing terms J^{imp} and M^{imp} , but for the latter, the forcing terms change due to the mathematical derivations, becoming different from zero only where the 2D inhomogeneities are located. More precisely, these inhomogeneities become sources of the secondary field formulation. The values of the resistivity in the considered model correspond to Model 2 in Table 6.1. Figure 6.5 displays the relative differences of the apparent resistivity between the full field and secondary field solutions for the TE and TM modes in a wide range of frequencies. In there, positions 1 to 4 correspond to measurements obtained at 0, 4, 8 and 20 km from the center of the domain, respectively. Due to the low differences observed, we conclude that both approaches provide analogous results. The results obtained with the full field formulation are accurate (see previous subsection), so the same conclusion is obtained about the ones computed with the secondary field formulation.

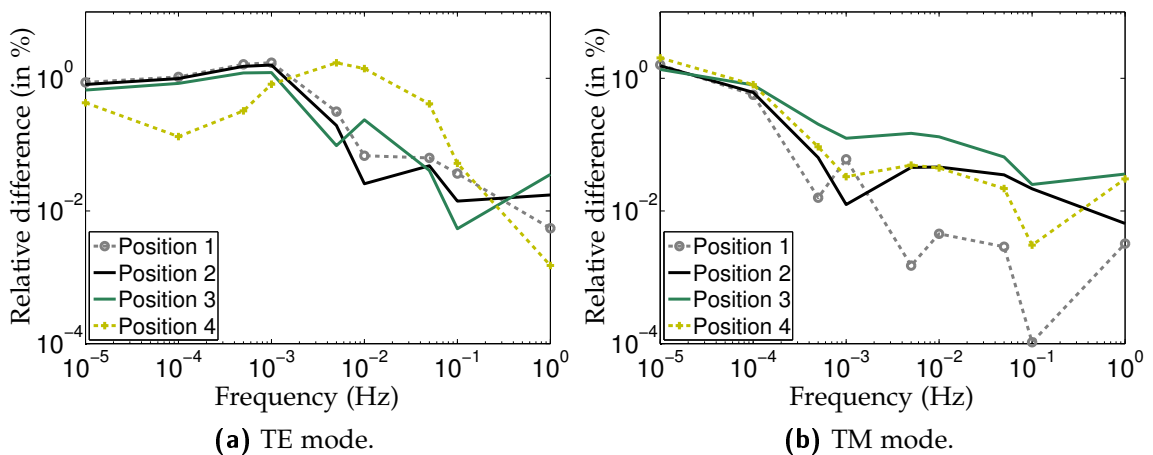


Figure 6.5: Relative errors between the results obtained with the full field formulation vs. those obtained with the secondary field formulation.

6.2.2 Inverse Problem

To test our inverse solver, we employ the model problem depicted in Figure 6.1c. The solution $\hat{\rho}$ and the initial point $\rho^{(0)}$ are:

$$\hat{\rho} = (80, 100, 120, 10), \quad \text{and} \quad \rho^{(0)} = (40, 40, 40, 40). \quad (6.1)$$

We consider no regularization term. Seven receivers are located on the Earth surface at different x -positions, and they record measurements at the following four different frequencies in Hz: $\nu_1 = 10^{-3}$, $\nu_2 = 10^{-2}$, $\nu_3 = 10^{-1}$, and $\nu_4 = 1$. We define the cost functional as

$$C(m) = \sum_{\omega_j}^4 \sum_i^7 \left| \frac{1}{\sqrt{\omega_j}} \left(z_{\omega_j}^i(m) - d_{\omega_j}^i \right) \right|^2. \quad (6.2)$$

In this example, we choose the resistivity as inversion variable and we employ the full field formulation to compute the forward problem. Table 6.3 displays the evolution of the values of the resistivity along the inversion process. Convergence is achieved for both the TE and TM mode in less than 10 iterations.

	TE mode				TM mode				Solution
	It. 2	It. 4	It. 6	It. 8	It. 2	It. 4	It. 6	It. 8	-
ρ_1	88.98	89.60	89.86	84.72	75.97	86.89	83.86	81.48	80
ρ_2	82.61	84.89	91.43	89.89	81.70	93.56	96.34	96.50	100
ρ_3	95.88	102.72	115.86	120.15	83.06	115.35	123.86	124.42	120
ρ_4	13.95	9.77	9.84	9.84	19.18	10.04	9.89	9.68	10

Table 6.3: Values of the resistivities during the inversion process.

6.3 NUMERICAL ANALYSIS

We now perform a numerical analysis of the forward and inverse solvers. In particular, we study the main numerical features of the hp -adaptive algorithm, the advantages and limitations of employing a secondary field formulation, the behavior of the PML, the different convergence results on the IP observed when selecting various inversion variables, and the advantages of performing first a lower dimensional (in our case, 1D) inversion before solving the higher dimensional (in our case, 2D) IP.

6.3.1 Forward Problem

First, we analyze the convergence properties of various types of refinements and we compare different refined grids. Then, we compare the computational demand of solving

the 2D problems when the full and secondary field formulations are employed, and finally we study the behavior of the solution within the PML region.

hp-Adaptivity

In this subsection, we consider both the goal-oriented and multi-goal-oriented adaptive algorithms described in Chapter 3.

CONVERGENCE ANALYSIS:

We consider the full field formulation 2D model problem of Figure 6.1c with a source operating at 0.1 Hz and the resistivity distribution of Model 1 in Table 6.1. Figure 6.6 displays the relative error between the numerical and reference solutions for E_y in the TE mode and H_y in the TM mode against the number of unknowns, i.e., the number of degrees of freedom (dof). The error is reduced by performing three different types of refinements: uniform h -refinements, uniform p -refinements, and multi-goal oriented adaptive hp -refinements. The relative error is evaluated at the center of the domain, which is the region most influenced by the presence of the inhomogeneity in the considered model problem. The high accuracy of the reference solution is guaranteed by computing an overkill solution obtained with some initial uniform h and p refinements plus some specific refinements performed with the multi-goal-oriented adaptive algorithm. Notice that the convergence behavior is not necessarily monotone because we are considering the error in a quantity of interest rather than in a global norm. Thus, it may increase from one iteration to the next even when globally refining the grid. In all cases, we observe the superior performance of the multi-goal oriented hp -adaptive algorithm. The initial slow convergence observed on the hp -adaptive algorithm for the TM mode is attributed to some pre-asymptotic convergence problems within the PML region. In Figures 6.6 and 6.7 we appreciate that the multi-goal oriented hp -adaptive algorithm provides lower errors with less computational requirements. Notice that even if the adaptivity is performed in terms of the EM fields, we can ensure the goodness of the grids for the numerical solution in terms of the impedance, because, up to a constant, it corresponds to the electric field divided by its derivative.

hp-GRIDS:

We now describe the different hp grids obtained after the adaptive process. We consider two different adaptive methods: the goal and multi-goal oriented hp -adaptivity. For the former, the objective is to obtain accurate results at one receiver placed on the center of the domain, while the main goal for the latter is to procure accurate results at seven different receivers placed from -20 to 20 km in the x -direction and along the Earth's surface. We display the grids for the TE and TM modes and we consider the secondary field formulation, which employs smaller computational domains, and therefore the details are more visible. The model problem in consideration is depicted in Figure 6.1d. The

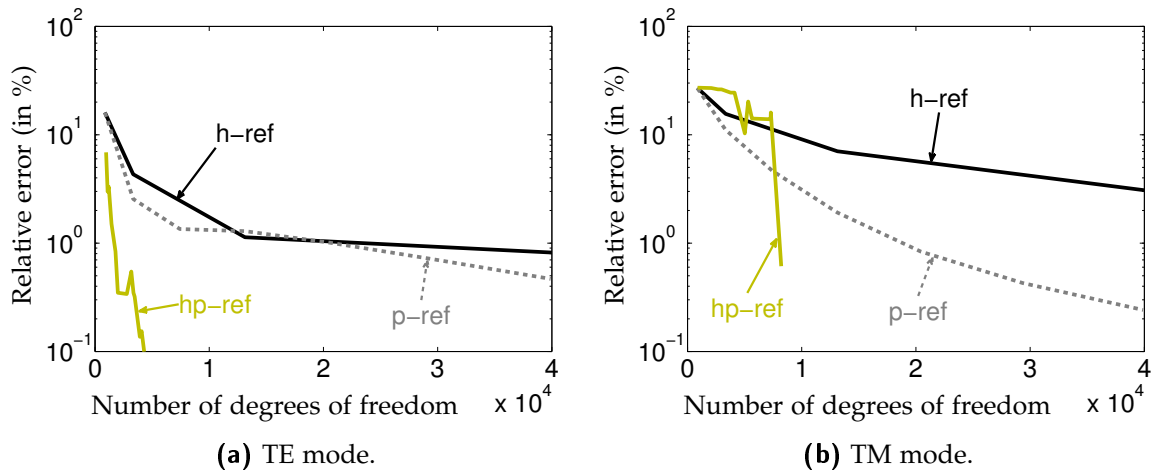


Figure 6.6: Relative error in E_y (TE mode) and H_y (TM mode) vs. the number of dof for three type of refinements: uniform h -refinements, uniform p -refinements and multi-goal oriented self-adaptive hp -refinements.

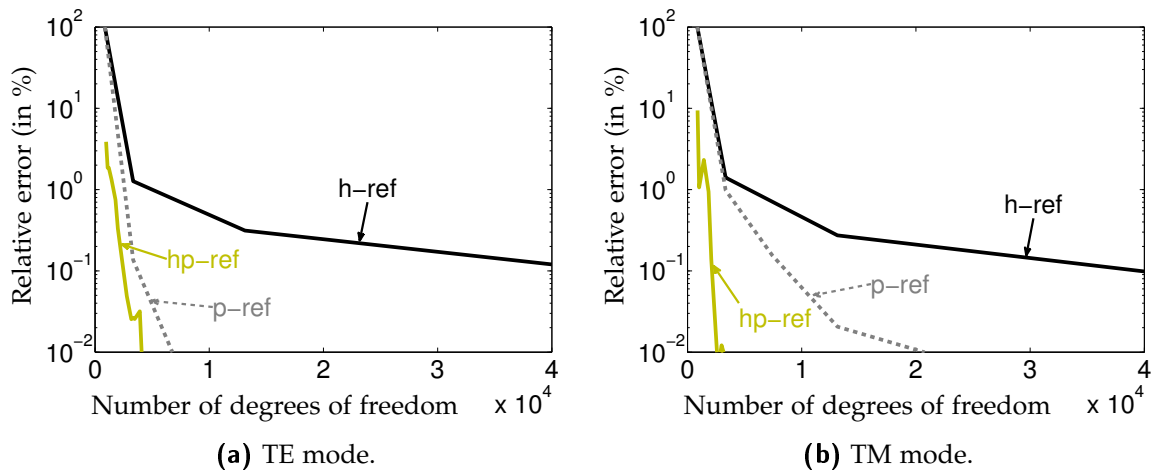


Figure 6.7: Relative error in the impedance vs. the number of dof. for three type of refinements: uniform h -refinements, uniform p -refinements and multi-goal oriented self-adaptive hp -refinements.

subsurface resistivity formation corresponds to $\rho_1 = 80$, $\rho_2 = 100$, $\rho_3 = 120$, $\rho_4 = 10$ Ohm-m and the frequency is equal to 0.1 Hz.

Figures 6.8a and 6.8b (left column) display the final grids when the multi-goal oriented hp -adaptivity is employed, while Figures 6.8c and 6.8d (right column) correspond to the ones that employ the single-goal oriented algorithm. Different colors indicate different polynomial order p , as shown at the bottom of the panels. The multi-goal oriented algorithm produces additional refinements towards the sides of the domain, that is, towards the receivers, whereas the traditional goal-oriented algorithm focuses in the single receiver located at the center, refining more towards this position. This is specially notorious at the air-ground interface. Additionally, we observe that while in the TE mode it is also necessary to correctly refine in the air, for the TM mode the refinements are concentrated in the subsurface.

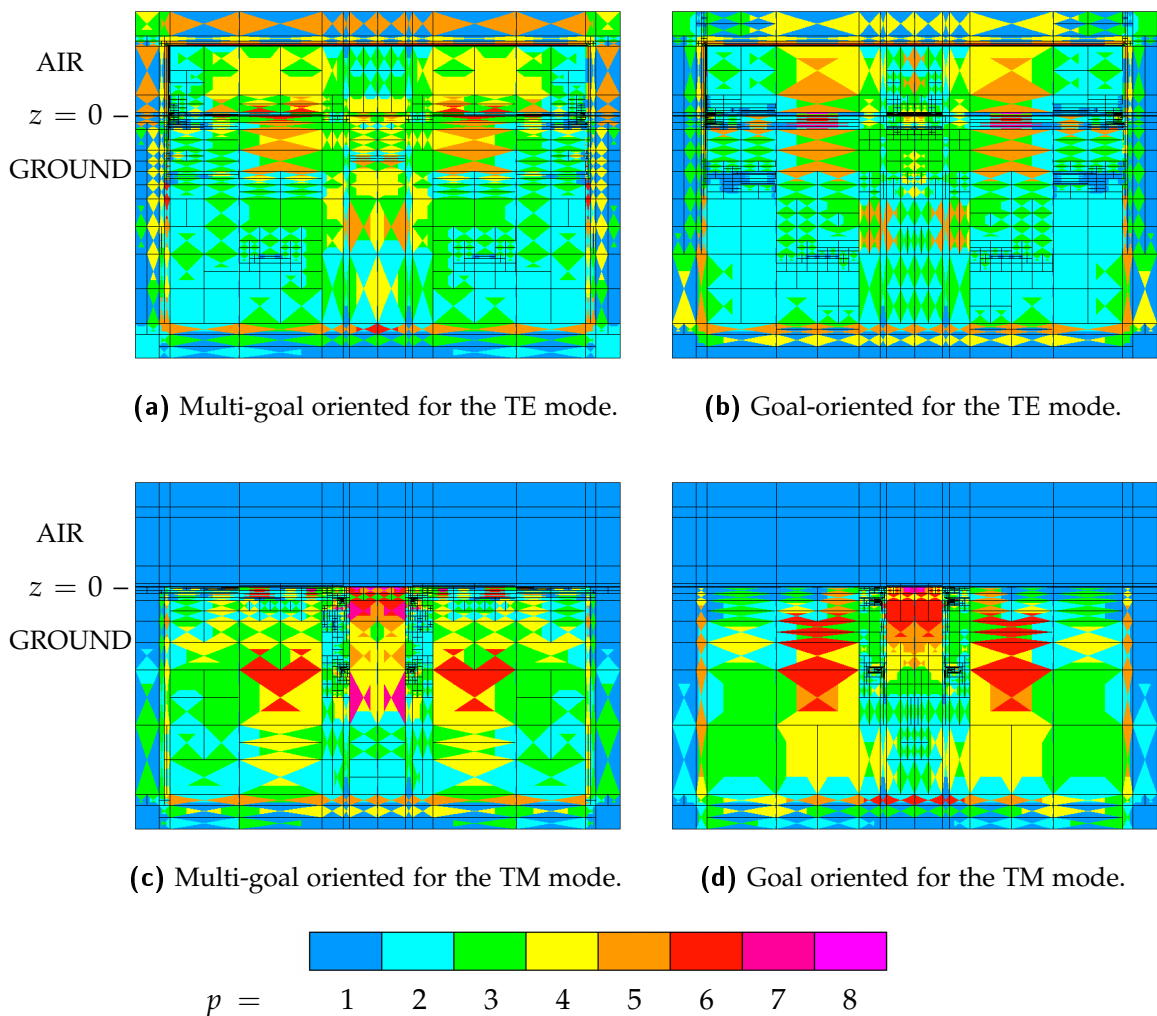
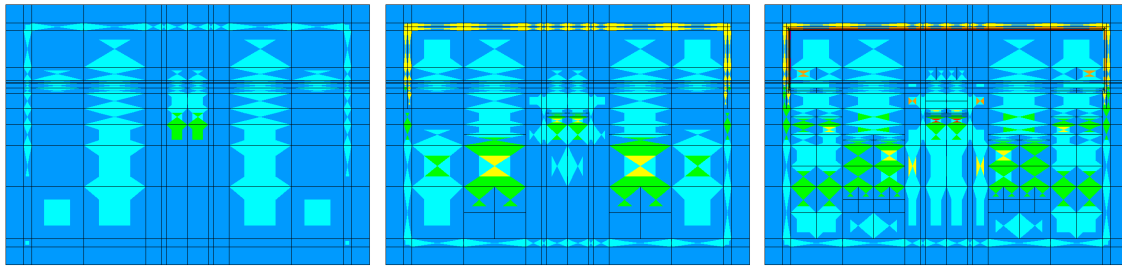


Figure 6.8: Different hp -grids after performing the adaptive algorithm for the TE and TM formulations with a frequency equal to 0.1 Hz.

We employ the same resistivity distribution, formulation (secondary field for the TE mode) and frequency to show in Figure 6.9 the different steps of the multi-goal oriented adaptivity, starting from a uniform $p = 1$ grid, to finish with the refined hp -mesh. This

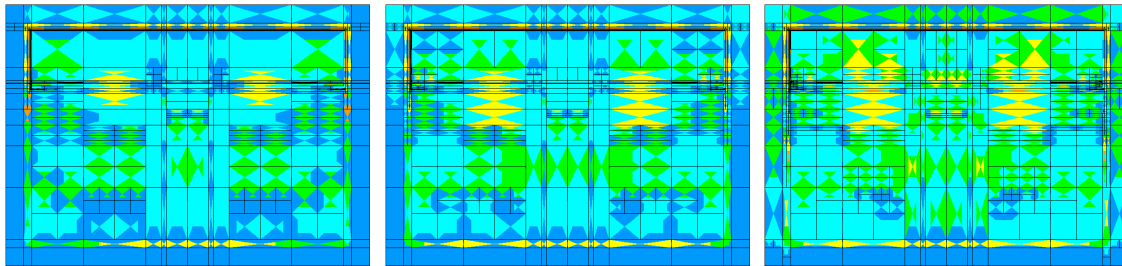
final grid counts with 9765 unknowns and it delivers a relative error in $L(E_y)$ below $1.17 \cdot 10^{-3} \%$.



(a) Iteration 3.

(b) Iteration 6.

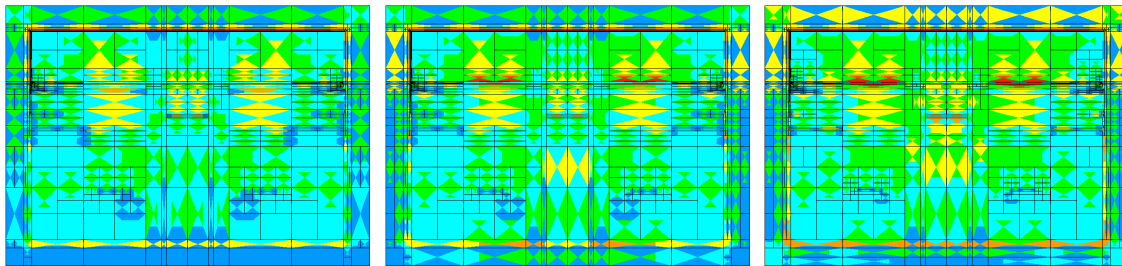
(c) Iteration 9.



(d) Iteration 12.

(e) Iteration 15.

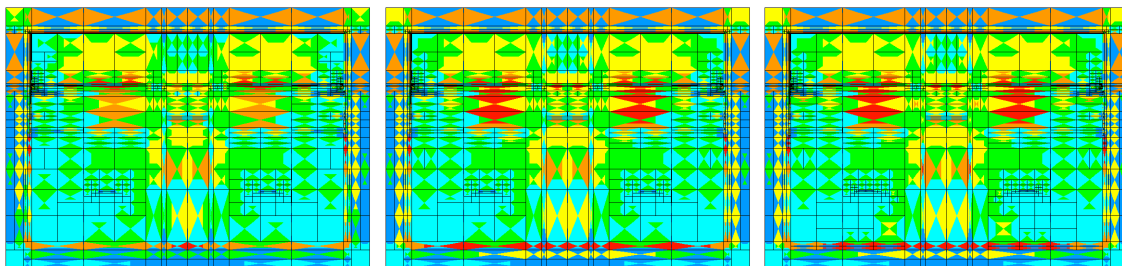
(f) Iteration 18.



(g) Iteration 21.

(h) Iteration 24.

(i) Iteration 27.



(j) Iteration 30.

(k) Iteration 33.

(l) Iteration 36.

Figure 6.9: Different hp -grids during execution of the multi-goal oriented adaptive algorithm for the TE mode when the secondary field formulation is employed at 0.1Hz.

Secondary Field Formulation

We now solve a 2D subsurface formation for the full and secondary field formulation problems, depicted in Figures 6.1c and 6.1d, respectively. The resistivity distribution is given by Model 1 in Table 6.1 and the frequency is equal to 0.1 Hz. Using the full field formulation, we compute an overkill solution with a much finer grid obtained by performing uniform h and p refinements plus some specific refinements performed with the multi-goal-oriented adaptive algorithm. We use it to estimate the relative errors corresponding to the secondary and full field formulations after several h or p uniform refinements. Figure 6.10 displays the results of these computations when the receiver is located at the center of the domain.

In all cases we observe that the secondary field formulation requires less dof than the full field formulation in order to produce a comparable error level, as expected. Additionally, p -uniform refinements provide faster convergence when compared to h -uniform refinements. This difference between the performance of p -refinements versus h -refinements is more notorious in the TE mode than in the TM mode for the considered example.

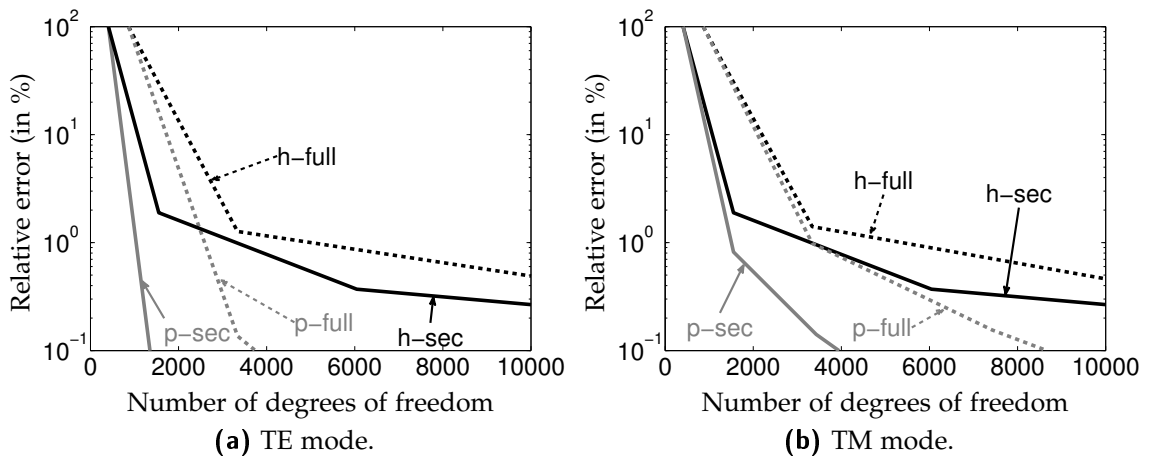


Figure 6.10: Relative error for the apparent resistivity computed with the full and secondary field formulations.

Figure 6.11 displays the logarithm of the absolute value of the solution for the TE and TM modes, that is, $\log(|E_y|)$ and $\log(|H_y|)$, respectively, when the secondary field formulation is employed. As we can see in these solutions, the inhomogeneous subsurface material plays now the role of the source. Moreover, the effect of the inhomogeneity along the Earth's surface is more concentrated in terms of lateral extend for the TM mode, while for the TE mode, such effect is more diffusive along the x -direction, affecting a significantly larger (in terms of lateral extend) area. It is also noticeable the quick decay of the TM mode field as it penetrates on the air, in contrast to what occurs for the TE mode, in which the secondary field travels long distances on the air before it dissipates.

Figure 6.12 displays the logarithm of the absolute value of the solutions of the adjoint problems corresponding to the receiver located at $x = -20$ km for the two modes. Similar

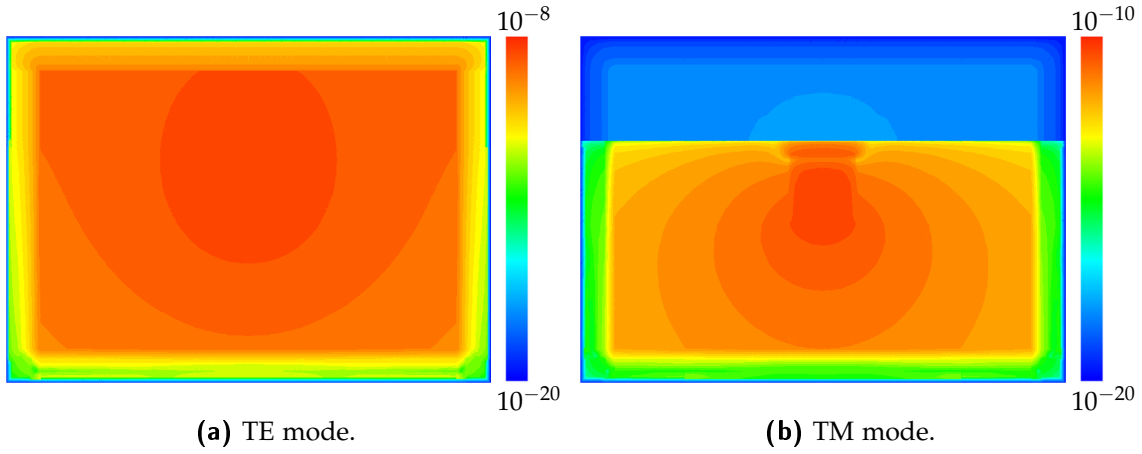


Figure 6.11: $\log(|E_y|)$ for the TE and $\log(|H_y|)$ for the TM mode when the secondary field formulation is employed.

conclusions than from the forward solutions hold. Additionally, we observe that the considered receiver plays the role of the source in both modes.

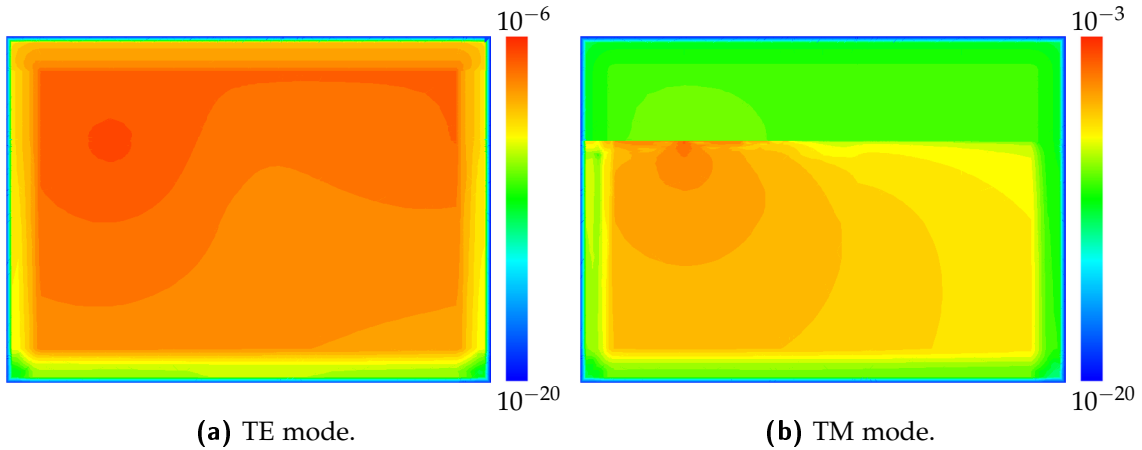


Figure 6.12: Logarithm of the module of the solution of the adjoint problem corresponding to the receiver located at $x = -20$ km for the TE and TM modes, when the secondary field formulation is employed.

PML

To study the behavior of the solution into the PML region, we consider the problem illustrated in Figure 6.1c with a resistivity distribution given by Model 2 and a frequency equal to 10^{-4} Hz. We focus on the TE mode, and we display in Figure 6.13 the logarithm of the module of the y component of the electric field ($\log(|E_y|)$) along all sides of the computational domain. We observe that the PML behaves properly everywhere, with a smooth decay for the solution and without introducing numerical reflections even in the areas with high contrast between material properties. Panels (a) and (b) correspond to the intersection between air and ground. In there, the contrast between resistivities is about sixteen orders of magnitude and even in this extreme scenario, the decay profile seems to be superb.

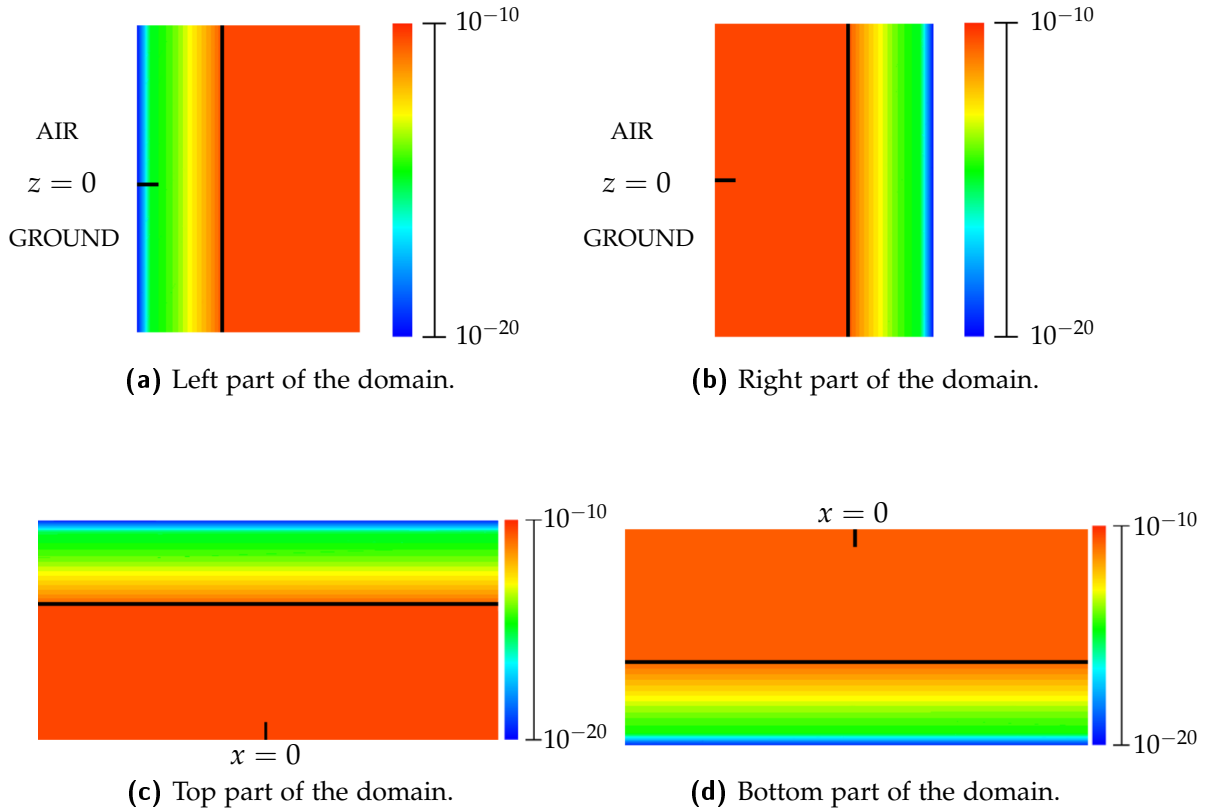


Figure 6.13: $\log(|E_y|)$ corresponding to a 5 km thick PML and $\alpha = 10^{-5}$. The black line indicates the region where the PML starts.

6.3.2 Inverse Problem

First, we analyze the convergence of the IP when different inversion variables are employed. Then, we perform a joint TE+TM inversion. Finally, we compare the traditional approach with the DAM approach to illustrate the gains of considering the 1D solution in the 2D IP. Our aim is to compare different numerical properties of the IPs. To avoid any possible pollution in the forward model, we employ a sufficiently refined same grid in all the numerical forward simulations of this subsection. The model problem is then always the one depicted in Figure 6.1c.

Selection of the Inversion Variables

To consider different optimization unknowns is equivalent to deal with different Taylor expansions in equation (4.9), which directly affect the convergence of the optimization method. In here, we analyze how different unknowns in the MT IP affect the convergence of the optimization method. We will consider three different variables, namely $m = \sigma$, its logarithm $m = \log(\sigma)$, and $m = \rho = 1/\sigma$ (we remark that $m = \log(\sigma)$, and $m = \log(\rho)$ delivers the same results). To do so, we consider the IP defined in Section 3 and we solve (4.5) with no regularization term, namely, with $\lambda = 0$ in (4.2). Given an arbitrary initial distribution $\rho^{(0)}$, we are interested in recovering the original one $\hat{\rho}$. We consider the two described models in Table 6.1, for which starting point is given by:

	$\rho^{(0)}$	$\hat{\rho}$
Model 1	(40, 40, 40, 40)	(80, 100, 120, 10)
Model 2	(25, 25, 25, 25)	(3, 2, 4, 200)

Table 6.4: Initial point and solution for the considered inverse problems.

Seven receivers are located on the surface at different x -positions, and they record measurements at the following four different frequencies in Hz: $\nu_1 = 10^{-3}$, $\nu_2 = 10^{-2}$, $\nu_3 = 10^{-1}$, and $\nu_4 = 1$. Figures 6.14 and 6.15 display the value of the cost functional against the iteration number of the L-BFGS-U optimization method, while Table 6.5

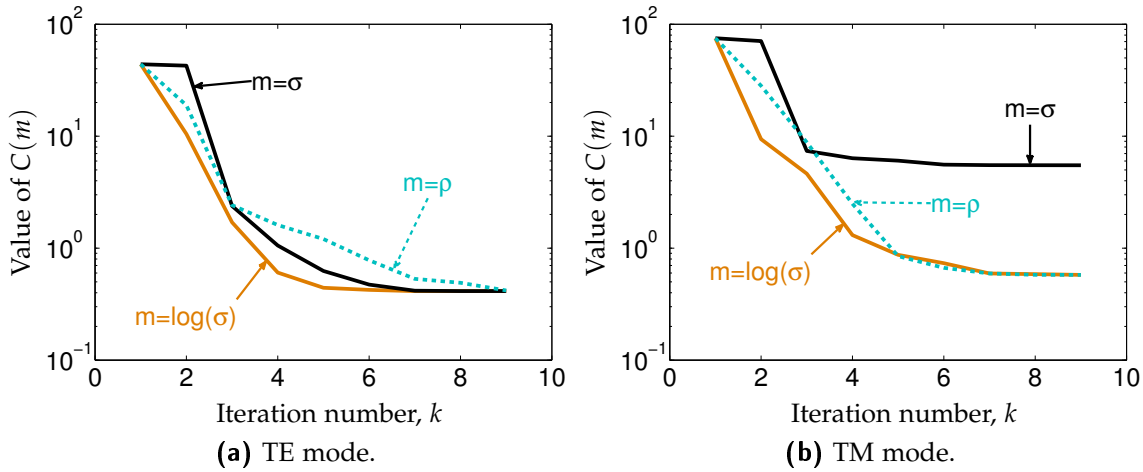


Figure 6.14: Cost functional against the iteration number for Model 1 in Table 6.1.

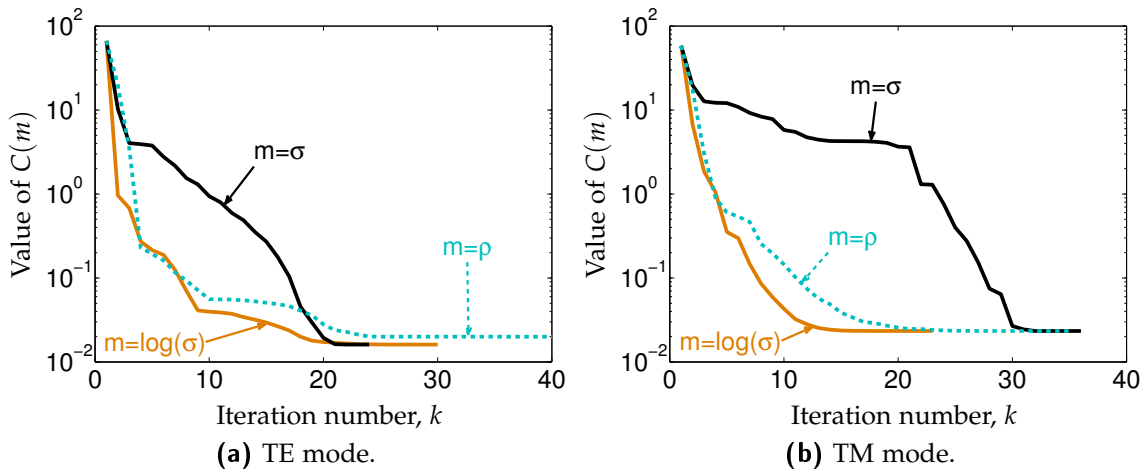


Figure 6.15: Cost functional against the iteration number for Model 2 in Table 6.1.

provides the solution to the IPs at the end of the iterative processes.

Several conclusions comes from these results for the selected examples:

	Model 1		Solution	Model 2		Solution
	TE mode	TM mode	-	TE mode	TM mode	-
$m = \sigma$						
ρ_1	84.30	77.34	80	3.01	2.99	3
ρ_2	87.76	112.09	100	2.02	2.08	2
ρ_3	119.66	118.02	120	4.02	3.74	4
ρ_4	9.93	0.69	10	1000	432.94	200
$m = \rho$	-	-	-	-	-	-
ρ_1	84.72	81.48	80	3.02	2.99	3
ρ_2	89.89	96.50	100	2.02	2.08	2
ρ_3	120.16	124.42	120	4.03	3.74	4
ρ_4	9.94	9.68	10	1000	426.50	200
$m = \log(\sigma)$	-	-	-	-	-	-
ρ_1	83.73	81.25	80	3.02	2.99	3
ρ_2	88.76	96.88	100	2.02	2.08	2
ρ_3	119.81	124.17	120	4.02	3.74	4
ρ_4	9.88	9.68	10	1000	426.07	200

Table 6.5: Values of the resistivities for the solution of the inversion problem.

- The selected inversion unknown strongly affects to the convergence of the method. All inversion unknowns perform similarly for the TE mode, while for the TM mode, when employing the conductivity we are unable to solve the IP. In Model 2, the conductivity is the worst inversion unknown. Since each iteration demands to solve N_ω forward direct problems and $N_\omega \times N_{rec}$ forward adjoint problems, a good selection of the inversion variable becomes important to reduce the computational cost of the inversion. For the considered examples, $m = \log(\sigma)$ seems the best option as an unknown, while $m = \sigma$, is always the worst (except in one case).
- There is not a significant difference between the performance of the TE and TM modes.
- The most resistive layer of Model 2 is not accurately recovered, in part due to the effect of noise. Additionally, we have numerically observed that the value of the cost functional close to the solution does not change significantly when the value of ρ_4 varies between 150 and 1000. This suggest that the cost functional presents a valley, and hence, it is barely sensitive to this parameter.

TE+TM Inversion

We now consider the joint TE+TM inversion. Again, we solve the IP without regularization parameter in order to compare the results with the single mode inversion of the previous section. The cost functional is then given by

$$C(m) = \sum_k \sum_{\omega_j} \sum_i \left| \frac{1}{\sqrt{\omega_j}} \left(z_{\omega_j}^{i,k}(m) - d_{\omega_j}^{i,k} \right) \right|^2. \quad (6.3)$$

where the sum in k is for the two different modes (TE and TM), and where we consider the following four different frequencies in Hz: $\nu_1 = 10^{-3}$, $\nu_2 = 10^{-2}$, $\nu_3 = 10^{-1}$, and $\nu_4 = 1$.

Figure 6.16a shows a comparison between the TE inversion, TM inversion and TE+TM inversion for Model 1 when the unknown for the inversion corresponds to the logarithm of the conductivity. The convergence curve is almost identical in the three cases, and the solution for the TE+TM inversion is $\hat{\rho} = (79.63, 97.21, 122.49, 10.01)$, which is much more accurate than that obtained with any of the two single mode inversion. However, as counterpart, the computational cost of computing each iteration for the TE+TM inversion is doubled.

Figure 6.16b compares the performance of the same three modes when the resistivity is the unknown of the IP for the Model 2 in Table 6.4. While we are unable to accurately solve the IP for the TE mode or the TM mode when considering them independently (see Table 6.5), the IP for the joint TE+TM inversion for Model 2 in Table 6.4 converges to a more accurate solution than the single modes solutions, namely, to $\hat{\rho} = (3.01, 2.02, 4.04, 133.33)$.

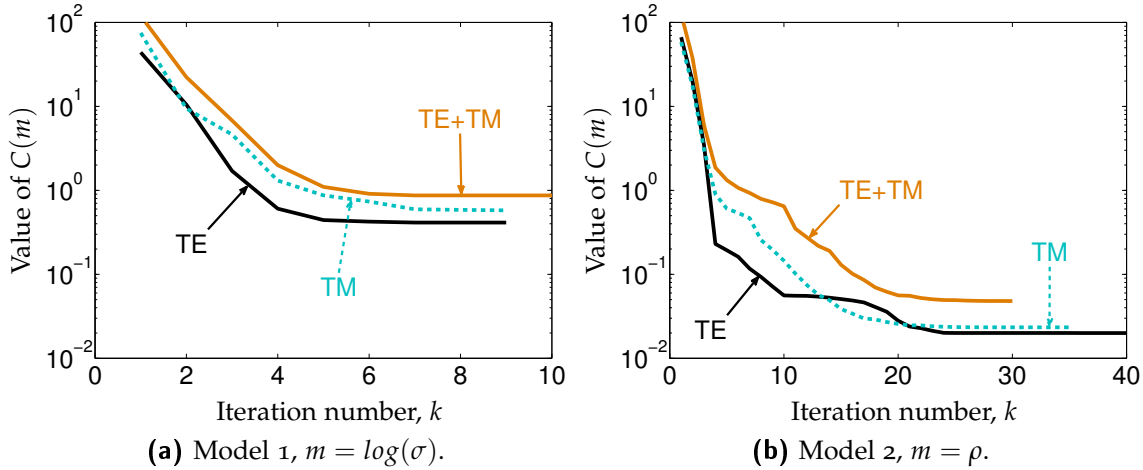


Figure 6.16: Cost functional against the iteration number when different modes are employed in the inversion.

Traditional Approach vs DAM

We now compare the traditional approach (employed in the previous subsection) with the DAM approach. We consider the full field and the model problem depicted in Figure 6.1c. We have seen in the previous subsection that the IP corresponding the Model 1 Table 6.1 converges in few iterations. Thus, we compare the traditional and DAM approaches for Model 2, because requiring more iterations, we expect to have greater savings. The employed four different frequencies in Hz are $\nu_1 = 10^{-3}$, $\nu_2 = 10^{-2}$, $\nu_3 = 10^{-1}$, and $\nu_4 = 1$.

The idea for the DAM approach is the following:

- Given a 2D problem, perform first the inversion for an underlying 1D layered media with 2D measurements as data in the cost functional.
- Use the analytical solution for the direct solver during this 1D inversion. Thus, the computational cost of the 1D inversion is negligible.
- Employ the 1D inverse solution as the initial point for the 2D inversion.

Additionally, the 1D solution can also be used as a regularization parameter in the cost functional. However, our aim here is to only compare the computational performance of the traditional vs. the DAM approach for the inversion, and therefore, we employ exactly the same cost functional in both cases, that is, no regularization parameter is used.

Lets denote by $\rho_{1D}^{(0)} = (\rho_1^{(0)}, \rho_2^{(0)}, \rho_3^{(0)})$ and $\hat{\rho}_{1D} = (\hat{\rho}_1, \hat{\rho}_2, \hat{\rho}_3)$ the initial point and the solution of the 1D IP, and lets denote by $\rho_{trad}^{(0)}$ and $\rho_{DAM}^{(0)}$ the initial points for the 2D IP when the traditional and the DAM approaches are employed, respectively. We consider two different scenarios to compare the traditional and DAM approaches: The first one employs the TE mode and the conductivity as inversion variable, while the second one uses the joint TE+TM inversion and the resistivity as inversion variable. Table 6.6 summarized the information of each of them.

	$\rho_{1D}^{(0)}$	$\hat{\rho}_{1D}$	$\rho_{trad}^{(0)}$	$\rho_{DAM}^{(0)}$
scenario 1	(25, 25, 25)	(3.11, 3.03, 3.07)	(25, 25, 25, 25)	(3.11, 3.03, 3.07, 25)
scenario 2	(25, 25, 25)	(3.06, 4.95, 4.92)	(25, 25, 25, 25)	(3.06, 4.95, 4.92, 25)

Table 6.6: Information of the two scenarios considered to compare the traditional and the DAM approaches for the inversion.

Figure 6.17 displays the value of the cost functional against the iteration number for the two scenarios. The gray solid line corresponds to the traditional problem and the dashed black line to the DAM problem. In addition to observe two orders of magnitude difference at the beginning of the IP, due to the inclusion of physical relevant information contained on the underlying 1D problem, the algorithm employing the DAM approach converges significantly faster. For this particular scenarios, it only requires approximately a 25% of the iterations, which implies huge computational savings.

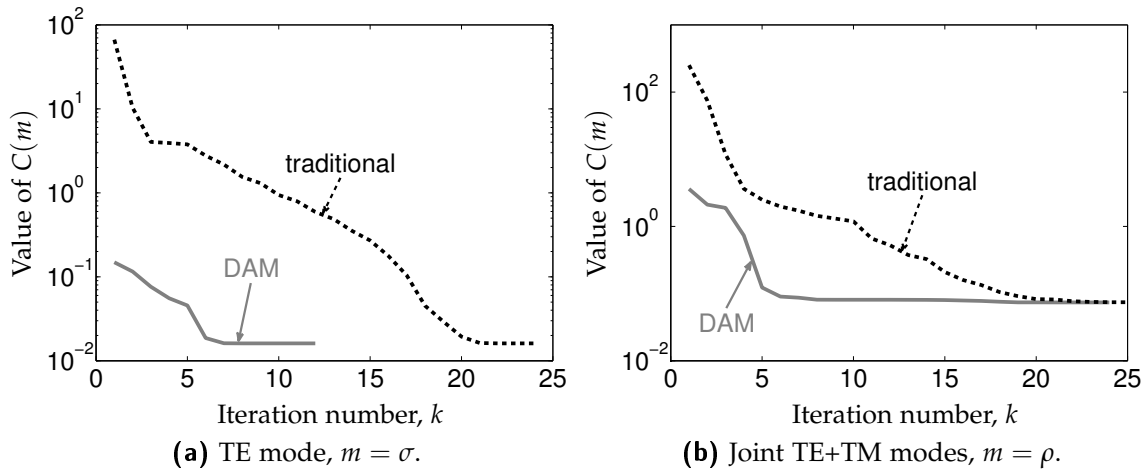


Figure 6.17: Cost functional against the iteration number for the traditional and DAM inverse problems for Model 2 in Table 6.1.

6.4 GEOPHYSICAL RESULTS

In this subsection, we show some interesting results with geophysical significance. Specifically, we first perform a frequency analysis. After that, we study the accuracy of selecting different QoIs for our forward solver. Next, we compare the different information provided by TE and TM measurements, and finally we illustrate the possibility of separating the 1D and 2D effects of the solution on the recorded measurements under the assumption of an underlying 1D layered Earth subsurface.

6.4.1 Frequency Analysis

Our capacity to detect a given target lies on our capability to capture the inhomogeneities in the solution. This fact depends on the considered frequency and the resistivity of the subsurface via the skin depth (see Chapter 1). We consider the model problem depicted in Figure 6.1c, and the subsurface distributions given by Table 6.1. We display in Figure 6.18 the relative difference between the solutions corresponding to the 1D model and the 2D model containing the inhomogeneity. Different conclusions hold from these results: (a) there are some frequencies for which it is impossible to detect the anomaly (namely, above 10 Hz in the first model and 0.1 Hz in the second one), (b) each mode behaves differently in the presence of the 2D inhomogeneity, and (c) the sensitivity of the measurements to the presence of the 2D inhomogeneity depends upon both the frequency and the resistivity distribution.

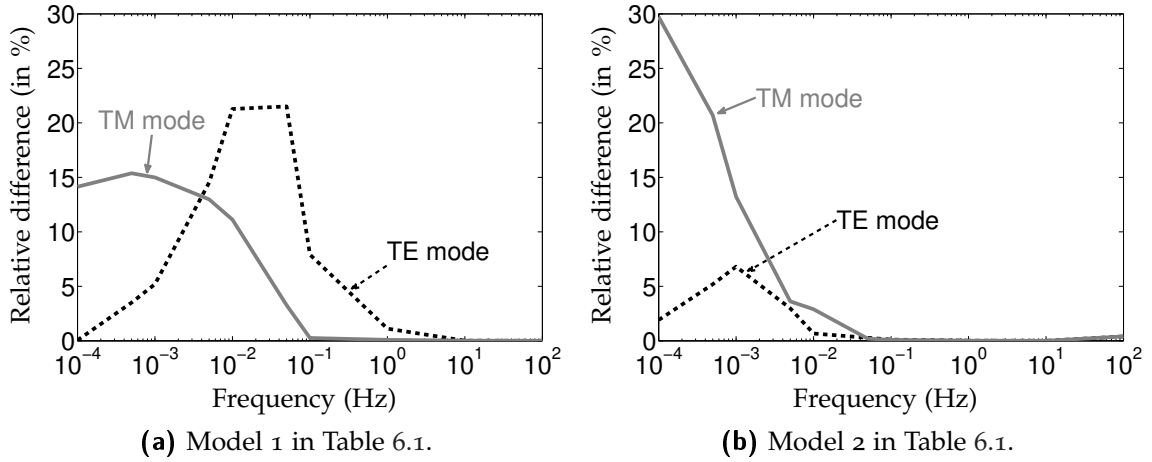


Figure 6.18: Relative difference in the simulated measurements at the center of the domain produced by the presence of a 2D inhomogeneity for different frequencies for the models in Table 6.1.

6.4.2 Study of the Quantity of Interest

In here, we study how the selection of the QoI and presence of the PML affects to the accuracy of our forward direct solver. For simplicity, we display the results for the TE mode, but the same conclusions hold for the TM mode. The physical problem under consideration for the full and secondary field formulations are illustrated in Figures 6.1c and 6.1d, respectively. The values for the resistivity correspond to Model 1 in Table 6.4, and the frequency is equal to $5 \cdot 10^{-2}$ Hz.

We consider the following physical magnitudes: $Q_E^F(\rho)$ and $Q_Z^F(\rho)$, which correspond to the computation of the electric field and impedance when employing the full field formulation, while $Q_E^S(\rho)$ and $Q_Z^S(\rho)$ are the total (primary plus secondary) electric field and impedance, respectively, computed with the secondary field formulation. This impedance is also computed employing the total electric and magnetic fields.

Figure 6.19 displays the relative error between the numerical and reference solutions at the center of the domain (the region more influenced by the presence of the inhomogeneity) against the number of degrees of freedom, for the different quantities defined above. In all of them, the increase in the unknowns comes from performing uniform refinements in h and/or p , while the reference solution always corresponds to an overkill solution computed with the multi-goal-oriented adaptive algorithm. This algorithm employs a linear QoI to perform the adaptivity, and since the impedance is nonlinear, in here we consider for simplicity the y component of the electric field. Since the impedance is defined (up to a constant) as the electric field divided by its derivative, we can ensure the goodness of the reference solutions.

In a first step, we consider an scenario with a PML and we compare the electric field and impedance as QoI for both, full and secondary field formulations. Figure 6.19a describes the relative error for the electric field and the impedance with the full field formulation, while Figure 6.19b employs the secondary field formulation. In both cases, the

impedance provides more accurate results than the electric field itself, especially for the full field formulation, where the discrepancy is by several orders of magnitude. Additionally, comparing the errors given by both formulations, we appreciate that the secondary field formulation provides smaller errors for both physical magnitudes for a reasonable number of unknowns (up to 10^4). This is accentuated for the case of the electric field, which exhibits a large error (up to a 30%) when a coarse mesh is employed. However, the advantage of using the impedance as QoI diminishes for the secondary field formulation, although it still exhibits a smaller error for a reasonable number of unknowns (up to 10^4).

We now compute the same QoI without considering a PML. Being the air a non dissipative media, and since we employ Dirichlet homogeneous BCs for truncation purposes, we expect to have numerical reflections from the boundary and hence inaccurate results. We again compare in Figures 6.19c and 6.19d the electric field and the impedance when employing the full and the secondary field formulations, respectively. The same general conclusions hold for this case, but the results show other interesting features. For the full field formulation, the electric field contains 100% relative error even when the number of unknowns is large, as expected. However, the impedance shows a superb accuracy. These results suggest that it is unnecessary any effort in the truncation of the domain, which in general procure savings in both, computational complexity and implementation tasks. When the secondary field is employed, we obtain acceptable results for the electric field due to the attenuation of the source in a lossy media, as physically expected. However, the relative error does not converge to zero in the case of the electric field, in contrast to the impedance, whose relative error rapidly decreases.

From these results, we conclude that the impedance is not only independent of the source intensity, and more closely related to the formation conductivity, but it also provides dramatically smaller discretization errors, leading to large computational savings. Moreover, the impedance seems to be insensitive to certain artificial sources resulting from the direct truncation of the computational domain in the absence of a PML. As a result, the impedance seems a better choice as QoI in comparison with the electric field.

6.4.3 *TE vs TM Modes.*

We analyze the difference between the TE and TM solutions when a 2D inhomogeneity is embedded in the subsurface. We consider the full field formulation with the computational domain depicted in Figure 6.1c and resistivity distributions given by Table 6.1. Since we focus in the total fields, the results are the same for the secondary field formulation. We compute the relative difference between the numerical solution close to the inhomogeneity and the solution at $x = 100$ km, that is, far from the region where the 2D anomaly affects, and we represent in Figures 6.20 and 6.21 this difference along the Earth's surface at different frequencies: $\nu_1 = 10^{-1}$, $\nu_2 = 10^{-2}$, and $\nu_3 = 10^{-4}$ Hz.

As expected from the theory (see Chapter 2), the TM mode tends to resolve lateral resistivity variations better than the TE mode resistivity ρ_{yx} . Nonetheless, since the geomagnetic transfer function is sensitive to lateral conductivity variations, and the involved

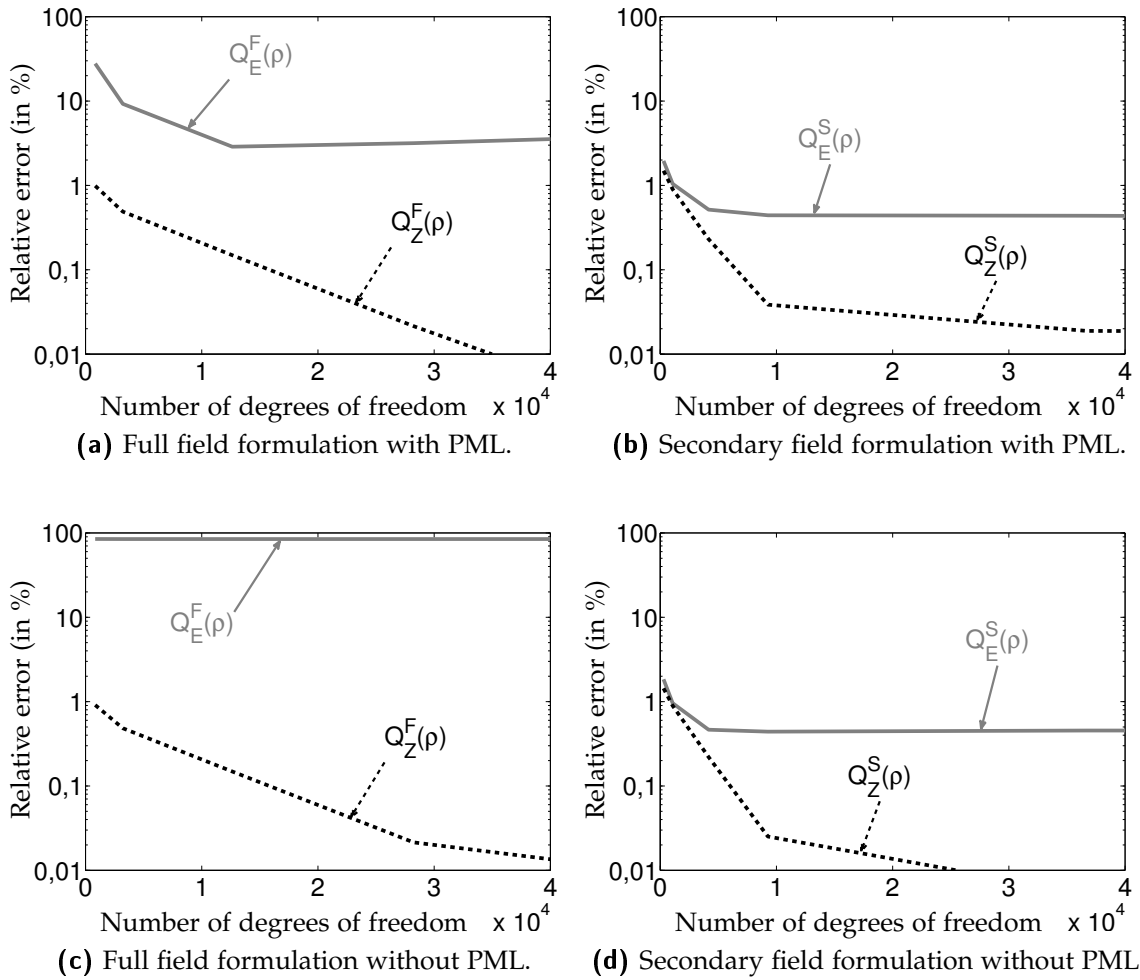


Figure 6.19: Relative error for different QoI: $Q_E^F(\rho)$ and $Q_Z^F(\rho)$ correspond to the total electric field and the impedance computed with the full field formulation, respectively, while $Q_E^S(\rho)$ and $Q_Z^S(\rho)$ are the equivalent quantities computed with the secondary field formulation.

fields are those associated to the TE mode, it is possible to identify lateral variations also from the TE mode. Figure 6.20 and 6.21 confirm that low frequencies (e.g., 10^{-4} Hz) are adequate to detect inhomogeneities when employing the TM mode, but not with the TE mode, as already indicated in Figure 6.18.

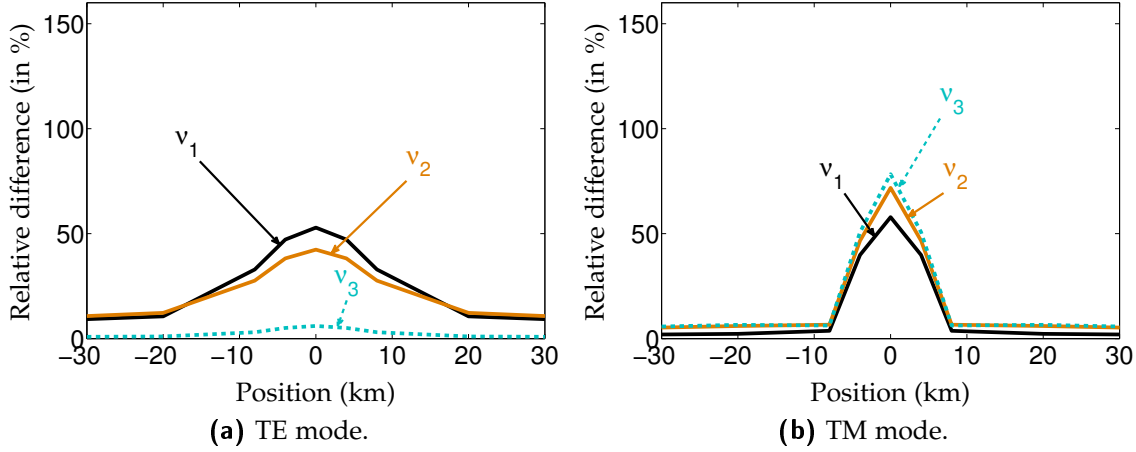


Figure 6.20: Relative difference between the impedance at the center of the domain and at $x = 100$ km at different frequencies for the Model 1 in Table 6.1.

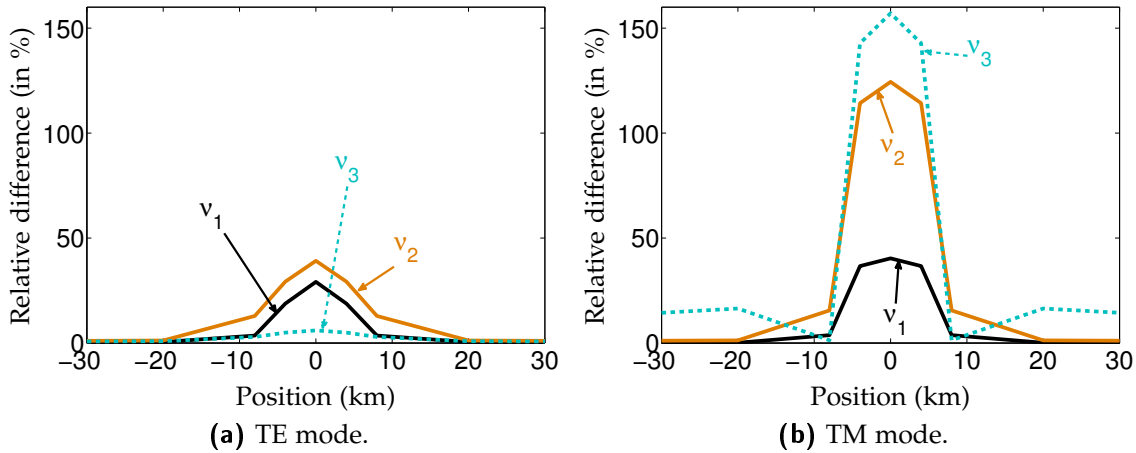


Figure 6.21: Relative difference between the impedance at the center of the domain and at $x = 100$ km at different frequencies for the Model 1 in Table 6.1.

6.4.4 Separation of 1D and 2D Effects

In this subsection, we consider the secondary field formulation with the computational domain depicted in Figure 6.1d and a frequency equal to 10^{-2} Hz, which is an adequate one in order to detect the considered 2D anomaly (see previous subsections). Since we know the analytical solution of the underlying 1D Earth model, we can compare it with our numerical solution.

Figure 6.22 displays the apparent resistivity along the surface for the two different problems described in Table 6.1. In there, the dashed lines correspond to the two underlying 1D layered solutions (“Layered 1” corresponds to $\rho_1 = 80, \rho_2 = 100, \rho_3 = 120$ and “Layered 2” corresponds to $\rho_1 = 80, \rho_2 = 10, \rho_3 = 120$), while the solid lines stand for the numerical solutions. We observe that the presence of the the anomaly affects to the numerical solution. In particular, the closer the inhomogeneity is, the larger is the influence on the numerical solution. Since the underlying 1D solutions (dashed lines) are known, these variations come only from the the 2D nature of the problem.

The TM mode resolves lateral variations more accurately than the TE mode, but it tends to overestimate resistivities close to the boundary when the resistivity is high, and underestimate them for low resistivities [157]. This does not occur with the TE mode, which is more stable for estimation of apparent resistivities. Figure 6.22a illustrates this effect.

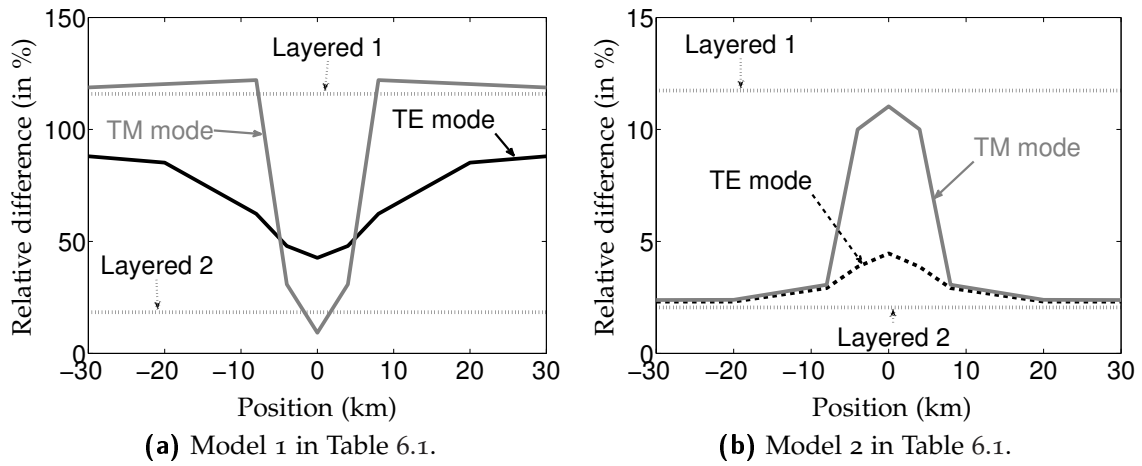


Figure 6.22: Apparent resistivity at different distances for the different subsurface formations.

CONCLUSIONS AND FUTURE WORK

In this dissertation, I have applied for the first time a *hp*-FEM to solve a MT problem in two spatial dimensions (2D). Optimal grids have been constructed using a multi-goal oriented adaptive algorithm. An automatically adjusted PML has been used to truncate the computational domain. I have implemented both the full forward formulation and a secondary field formulation where the primary field is given by the solution of a 1D layered media. Inversion of 2D results have also been obtained using a gradient based L-BFGS-U method when employing the TE mode, the TM mode, and the joint TE+TM modes.

From the mathematical point of view, I have derived 1D, 2D, and 3D variational formulations in terms of both the full and the secondary field formulations. I have also obtained variational formulations in arbitrary systems of coordinates, which enables both to consider PMLs and/or to implement certain dimensionality reduction methods such as the ones proposed in [106]. In addition, I have described an efficient adjoint based method for computation of the Jacobian and Hessian matrices.

Numerical results of this work have indicated that the multi-goal oriented self-adaptive strategy is able to provide accurate solutions at multiple receivers using a single mesh. Moreover, I have observed a fast convergence of the goal-oriented adaptivity in terms of the error vs. the problem size, as expected from the theory [52, 7]. Additionally, the automatically adjusted PML has shown numerically to be an adequate mesh truncation technique capable to deal with material property contrasts of up to 15 orders of magnitude (air-Earth interface). The secondary field formulation has shown to provide more accurate results than the full field formulation while employing only a fraction of the unknowns.

I have also illustrated the benefits of considering the dimensionality of the physical problem as a variable in the inverse problem. In our numerical examples, the Dimensionally Adaptive Inversion reduces the computational cost over 75%.

Extensive numerical experimentation performed over various MT model problems have also enabled us to conclude that:

- (a) In order for the effect of finite source modeling to be negligible, it is better to consider large domains (often, over 200 km in the horizontal direction). However, when employing a secondary field formulation, the forcing term appears only where the 2D inhomogeneities are placed, and even if the original source is assumed to be in-

finitely long, it is unnecessary to model it. This reduces the computational domain drastically.

- (b) I have performed a frequency sensitivity analysis, which indicates that the most crucial frequencies when looking for hydrocarbons at 2km depth are in the frequency range $10^{-4} - 10^{-1}$ Hz.
- (c) Despite the common believe among practitioners that certain variables are always better for the inversion than other variables, our numerical results indicate that the choice of the inversion variable is problem dependent, and any variation on the material properties may impact on the variable that is more adequate for inversion.
- (d) I have observed that TM mode tends to resolve lateral conductivity variations better than the TE mode, as suggested by [87].
- (e) Impedance tensors and apparent resistivities significantly exhibit lower relative errors than the EM fields. The case where I truncate the computational domain with an homogenous Dirichlet boundary conditions provides a prominent example. For such a model, unphysical reflections occurring on the boundary contaminate the EM fields producing relative errors above 100%, while the impedance tensor exhibits relative errors below 2%. From the physical point of view, this implies that impedances are insensitive to certain sources (produced at the domain boundary). After all, impedances tend to be more sensitive to material properties (coefficients of the PDE) than to the source (forcing term).

FUTURE LINES OF RESEARCH:

The first and more natural continuation of this work is to extend these results to 3D MT problems using the *hp*-FEM. Due to the high complexity of such implementation, I will explore the use of a simpler method for the 3D solver, such as a 2D *hp*-FEM combined using tensor product structure with a 1D Fourier type discretization.

Another future research line includes the design and study of goal-oriented adaptive methods using highly nonlinear quantities of interest such as impedances or apparent resistivities.

Finally, another research direction that I propose in this dissertation is the use of a Dimensionally Adaptive Method (DAM) using various dimensions, from the 1D problem, to the 3D one.

APPENDIX

8.1 APPENDIX: UNCOUPLING MAXWELL'S EQUATIONS IN ANISOTROPIC MEDIA

We define $\mathbf{A}(x, y, z) = (A_x(x, y, z), A_y(x, y, z), A_z(x, y, z))$ and

$$\boldsymbol{\lambda} = \begin{pmatrix} \lambda_x & 0 & 0 \\ 0 & \lambda_y & 0 \\ 0 & 0 & \lambda_z \end{pmatrix}. \quad (8.1)$$

Then,

$$\begin{aligned} \boldsymbol{\lambda} \nabla \times \mathbf{A} &= \begin{pmatrix} \lambda_x & 0 & 0 \\ 0 & \lambda_y & 0 \\ 0 & 0 & \lambda_z \end{pmatrix} \cdot \begin{vmatrix} \hat{x} & \hat{y} & \hat{z} \\ \partial_x & \partial_y & \partial_z \\ A_x & A_y & A_z \end{vmatrix} = \\ &= \hat{x} \left[\lambda_x \left(\frac{\partial A_z}{\partial y} - \frac{\partial A_y}{\partial z} \right) \right] \\ &+ \hat{y} \left[\lambda_y \left(\frac{\partial A_x}{\partial z} - \frac{\partial A_z}{\partial x} \right) \right] \\ &+ \hat{z} \left[\lambda_z \left(\frac{\partial A_y}{\partial x} - \frac{\partial A_x}{\partial y} \right) \right]. \end{aligned} \quad (8.2)$$

If we define

$$B = \lambda_x \left(\frac{\partial A_z}{\partial y} - \frac{\partial A_y}{\partial z} \right), \quad C = \lambda_y \left(\frac{\partial A_x}{\partial z} - \frac{\partial A_z}{\partial x} \right), \quad D = \lambda_z \left(\frac{\partial A_y}{\partial x} - \frac{\partial A_x}{\partial y} \right), \quad (8.3)$$

then,

$$\begin{aligned}
\nabla \times \lambda \nabla \times \mathbf{A} &= \begin{vmatrix} \hat{x} & \hat{y} & \hat{z} \\ \partial_x & \partial_y & \partial_z \\ B & C & D \end{vmatrix} = \hat{x} \left[\frac{\partial D}{\partial y} - \frac{\partial C}{\partial z} \right] + \hat{y} \left[\frac{\partial B}{\partial z} - \frac{\partial D}{\partial x} \right] + \hat{z} \left[\frac{\partial C}{\partial x} - \frac{\partial B}{\partial y} \right] = \\
&= \hat{x} \left[\frac{\partial}{\partial y} \left[\lambda_z \left(\frac{\partial A_y}{\partial x} - \frac{\partial A_x}{\partial y} \right) \right] - \frac{\partial}{\partial z} \left[\lambda_y \left(\frac{\partial A_x}{\partial z} - \frac{\partial A_z}{\partial x} \right) \right] \right] \\
&+ \hat{y} \left[\frac{\partial}{\partial z} \left[\lambda_x \left(\frac{\partial A_z}{\partial y} - \frac{\partial A_y}{\partial z} \right) \right] - \frac{\partial}{\partial x} \left[\lambda_z \left(\frac{\partial A_y}{\partial x} - \frac{\partial A_x}{\partial y} \right) \right] \right] \\
&+ \hat{z} \left[\frac{\partial}{\partial x} \left[\lambda_y \left(\frac{\partial A_x}{\partial z} - \frac{\partial A_z}{\partial x} \right) \right] - \frac{\partial}{\partial y} \left[\lambda_x \left(\frac{\partial A_z}{\partial y} - \frac{\partial A_y}{\partial z} \right) \right] \right].
\end{aligned} \tag{8.4}$$

If $\partial/\partial y = 0$, which corresponds to the 2D scenario along strike approach, and $\mathbf{A} = (0, A_y, 0)$, which corresponds to the type of sources that we employ,

$$\nabla \times (\lambda \mathbf{A}) = \left(\frac{-\partial(\lambda_y A_y)}{\partial z}, 0, \frac{\partial(\lambda_y A_y)}{\partial x} \right). \tag{8.5}$$

Comparing (8.4) and (8.5) with (1.20) component by component, we obtain the set of equations for the electric field:

$$\begin{aligned}
\frac{\partial}{\partial z} \left(\mu^{-1} \left(\frac{\partial E_z}{\partial x} - \frac{\partial E_x}{\partial z} \right) \right) - k^2 E_x &= \mu^{-1} \frac{\partial M_y^{imp}}{\partial z}, \\
-\nabla \cdot (\mu^{-1} \nabla E_y) - k^2 E_y &= -j\omega J_y^{imp}, \\
\frac{\partial}{\partial x} \left(\mu^{-1} \left(\frac{\partial E_x}{\partial z} - \frac{\partial E_z}{\partial x} \right) \right) - k_v^2 E_z &= -\mu^{-1} \frac{\partial M_y^{imp}}{\partial x},
\end{aligned} \tag{8.6}$$

where $k_v^2 = \omega^2 \epsilon - j\omega \sigma_v$.

Comparing (8.4) and (8.5) with (1.21) component by component, we obtain the set of equations for the magnetic field field:

$$\begin{aligned}
\frac{\partial}{\partial z} \left(\hat{\sigma}^{-1} \left(\frac{\partial H_z}{\partial x} - \frac{\partial H_x}{\partial z} \right) \right) + j\omega \mu H_x &= -\frac{\partial}{\partial z} \left(\hat{\sigma}^{-1} J_y^{imp} \right), \\
\left[-\frac{\partial}{\partial x} \left(\hat{\sigma}_v^{-1} \frac{\partial H_y}{\partial x} \right) - \frac{\partial}{\partial z} \left(\hat{\sigma}^{-1} \frac{\partial H_y}{\partial z} \right) \right] + j\omega \mu H_y &= -M_y^{imp}, \\
\frac{\partial}{\partial x} \left(\hat{\sigma}^{-1} \left(\frac{\partial H_x}{\partial z} - \frac{\partial H_z}{\partial x} \right) \right) + j\omega \mu H_z &= \frac{\partial}{\partial x} \left(\hat{\sigma}^{-1} J_y^{imp} \right).
\end{aligned} \tag{8.7}$$

The isotropic case is recovered by considering $\sigma_v = \sigma$.

8.2 VARIATIONAL FORMULATION IN THE COMPLEX PLANE

3D CASE.

If we integrate by parts the double curl expression, assuming no boundary terms we have that:

$$\int_{\Omega} (\bar{F})^T \nabla^x \times (\mu^{-1} \nabla^x \times E) = \int_{\Omega} (\nabla^x \times \bar{F})^T \mu^{-1} \nabla^x \times E, \quad (8.8)$$

where the superscript of ∇^x denotes that the derivatives are with respect the real variables $\mathbf{x} = (x, y, z)$. If we consider complex space variables $\zeta = (\zeta_1, \zeta_2, \zeta_3)$, then from the second equation of (2.15), we have that

$$\nabla^{\zeta} \times \bar{F} = \epsilon_{ijk} \frac{\partial \bar{F}_{\zeta_k}}{\partial \zeta_j} \hat{e}_{x_i} \stackrel{\text{eq. (2.14)}}{=} \epsilon_{ijk} \frac{\partial \bar{F}_{\zeta_k}}{\partial \bar{\zeta}_j} \hat{e}_{x_i} = \overline{\epsilon_{ijk} \frac{\partial F_{\zeta_k}}{\partial \zeta_j} \hat{e}_{x_i}} = \overline{\nabla^{\zeta} \times F}, \quad (8.9)$$

and therefore, the term to be employed in the variational formulation is:

$$\langle \nabla^{\bar{\zeta}} \times \tilde{F}, \tilde{\mu}^{-1} \nabla^{\zeta} \times \tilde{E} \rangle_{L^2(\tilde{\Omega})}. \quad (8.10)$$

2D CASE.

If we integrate by parts the divergence expression, assuming no boundary terms, we have that:

$$- \int_{\Omega} \bar{F} \nabla^x \cdot (\mu^{-1} \nabla^x E_y) = \int_{\Omega} \nabla^x \bar{F} \mu^{-1} \nabla^x E_y, \quad (8.11)$$

where the superscript of ∇^x denotes that the derivatives are with respect the real variables $\mathbf{x} = (x, z)$. Considering the complex space variables $\zeta = (\zeta_1, \zeta_2)$, then we have that

$$\nabla^{\zeta} \bar{F} = \frac{\partial \bar{F}}{\partial \zeta_i} \hat{e}_{x_i} \stackrel{\text{eq. (2.14)}}{=} \frac{\partial \bar{F}}{\partial \bar{\zeta}_i} \hat{e}_{x_i} = \overline{\nabla^{\zeta} F}, \quad (8.12)$$

and therefore, the expression to be used in the variational formulation corresponds to:

$$\langle \nabla^{\bar{\zeta}} \tilde{F}, \tilde{\mu}^{-1} \nabla^{\zeta} \tilde{E}_y \rangle_{L^2(\tilde{\Omega})} \quad (8.13)$$

REFERENCES

- [1] J. Alvarez-Aramberri, D. Pardo, and H. Barucq. A secondary field based hp -finite element method for the simulation of magnetotelluric measurements. *In press in Journal of Computational Science*, 2015. 64
- [2] J. Alvarez-Aramberri, D. Pardo, M. Paszynski, N. Collier, L. Dalcin, and V.M. Calo. On round-off error for adaptive finite element methods. *Procedia Computer Science*, 9:1474–1483, 2012. 40
- [3] D.N. Arnold, R.S. Falk, and R. Winther. Multigrid in $H(\text{div})$ and $H(\text{curl})$. *Numer. Math.*, 85(2):197–217, 2000. 69
- [4] D. Avdeev and A. Avdeeva. 3D magnetotelluric inversion using a limited-memory quasi-Newton optimization. *Geophysics*, 74(3):F45–F57, 2009. 54
- [5] I. Babuska, A. Craig, J. Mandel, and J. Pitkaranta. Efficient preconditioning for the p -version finite element method in two dimensions. *SIAM J. Numer. Anal.*, 28(3):624–661, 1991. 69
- [6] I. Babuška and B.Q. Guo. Regularity of the solution of elliptic problems with piecewise analytic data. Part i. Boundary value problems for linear elliptic equation of second order. *SIAM journal on mathematical analysis*, 19(1):172–203, 1988. 39
- [7] I. Babuška and B.Q. Guo. Approximation properties of the h - p version of the finite element method. *Computer Methods in Applied Mechanics and Engineering*, 133(3):319–346, 1996. xxxviii, xliv, 2, 38, 39, 103
- [8] I. Babuška and W.C. Rheinboldt. Adaptive approaches and reliability estimations in finite element analysis. *Computer Methods in Applied Mechanics and Engineering*, 17:519–540, 1979. 43
- [9] Y. Bazilevs, V.M. Calo, J.A. Cottrell, T.J.R. Hughes, A. Reali, and G. Scovazzi. Variational multiscale residual-based turbulence modeling for large eddy simulation of incompressible flows. *Computer Methods in Applied Mechanics and Engineering*, 197(1):173–201, 2007. 40
- [10] R. Becker, C. Johnson, and R. Rannacher. Adaptive error control for multigrid finite element methods. *Computing*, 55(4):271–288, 1995. 43
- [11] R. Becker and R. Rannacher. A feed-back approach to error control in finite element methods: basic analysis and examples. *East-West J. Numer. Math.*, 4(4):237–264, 1996. 43

References

- [12] R. Becker and R. Rannacher. *Weighted a posteriori error control in FE methods*. IWR, 1996. xxxviii, xlv, 2, 43
- [13] R. Bellman and G.M. Wing. *An introduction to invariant imbedding*. New York: John Wiley and Sons, 1975. 38
- [14] O. Benedix and B. Vexler. A posteriori error estimation and adaptivity for elliptic optimal control problems with state constraints. *Computational Optimization and Applications*, 44(1):3–25, 2009. 43
- [15] M.N. Berdichevsky. Principles of magnetotelluric profiling theory. *Applied Geophysics*, 1960. 6
- [16] M.N. Berdichevsky, I.A. Bezruk, and O.M. Chinavera. Magnetotelluric sounding with the use of mathematical filters. *Izv. Akad. Nauk SSSR*, 1973. 79
- [17] J.P. Berenger. A perfectly matched layer for the absorption of electromagnetic waves. *Journal of computational physics*, 114(2):185–200, 1994. xxxix, xlv, 22
- [18] A. Bermúdez, L. Hervella-Nieto, A. Prieto, and R. Rodríguez. Perfectly matched layers for time-harmonic second order elliptic problems. *Archives of Computational Methods in Engineering*, 17(1):77–107, 2010. 22
- [19] D.P. Bertsekas. Projected Newton methods for optimization problems with simple constraints. *SIAM J. CONTR. AND OPTIMIZ.*, 20(2):221–246, 1982. 56, 61
- [20] F.X. Bostick and H.W. Smith. Investigation of large-scale inhomogeneities in the earth by the magnetotelluric method. *Proceedings of the IRE*, 50(11):2339–2346, 1962. 6
- [21] J.H. Bramble. *Multigrid Methods*. Pitman Research Notes in Mathematics Series. 294. Harlow: Longman Scientific & Technical. viii, 1993. 69
- [22] C.R. Brewitt-Taylor and J.T. Weaver. On the finite difference solution of two-dimensional induction problems. *Geophysical Journal of the Royal Astronomical Society*, 47(2):375–396, 1976. 6
- [23] R.H. Byrd, P. Lu, J. Nocedal, and C. Zhu. A limited memory algorithm for bound constrained optimization. *SIAM Journal on Scientific Computing*, 16(5):1190–1208, 1995. 63
- [24] R.H. Byrd, J. Nocedal, and R.B. Schnabel. Representations of quasi-Newton matrices and their use in limited memory methods. *Mathematical Programming*, 63(1):129–156, 1994. xxxix, xlv, 3, 61
- [25] L. Cagniard. Basic theory of the magneto-telluric method of geophysical prospecting. *Geophysics*, 18(3):605–635, 1953. xxxvii, xliii, 1, 6

- [26] M. Cessenat. Mathematical methods in electromagnetism. Linear theory and applications. Series on advances in mathematics for applied sciences, 41, 1996. 20
- [27] A.D. Chave and A.G. Jones. *The magnetotelluric method: Theory and practice*. Cambridge University Press, 2012. xxxvii, xliii, 1, 79
- [28] W.C. Chew. *Waves and fields in inhomogeneous media*, volume 522. IEEE press New York, 1995. 13, 36, 67
- [29] W.C. Chew and W.H. Weedon. A 3D perfectly matched medium from modified Maxwell's equations with stretched coordinates. *Microwave and optical technology letters*, 7(13):599–604, 1994. 19, 22, 23, 29
- [30] J.H. Coggon. Electromagnetic and electrical modeling by the finite element method. *Geophysics*, 36(1):132–155, 1971. 6
- [31] A.R. Conn, N.I.M. Gould, and P.L. Toint. Global convergence of a class of trust region algorithms for optimization with simple bounds. *SIAM journal on numerical analysis*, 25(2):433–460, 1988. 61
- [32] A.R. Conn, N.I.M. Gould, and P.L. Toint. Testing a class of methods for solving minimization problems with simple bounds on the variables. *Mathematics of Computation*, 50(182):399–430, 1988. 56, 61
- [33] S.C. Constable, R.L. Parker, and C.G. Constable. Occam's inversion: A practical algorithm for generating smooth models from electromagnetic sounding data. *Geophysics*, 52(3):289–300, 1987. 53, 54
- [34] C. deGroot Hedlin and S. Constable. Occam's inversion to generate smooth, two-dimensional models from magnetotelluric data. *Geophysics*, 55(12):1613–1624, 1990. 53
- [35] L. Demkowicz. 2D *hp*-adaptive finite element package (2Dhp90) Version 2.0. *Ticam Report*, 2:06, 2002. xxvii, 35, 39, 41
- [36] L. Demkowicz. Fully automatic *hp*-adaptivity for maxwell's equations. *Computer methods in applied mechanics and engineering*, 194(2):605–624, 2005. 48
- [37] L. Demkowicz. *Computing with hp-Adaptive Finite Elements: volume 1. One and Two Dimensional Elliptic and Maxwell problems*. CRC Press, 2006. xxxviii, xlv, 1, 42, 65
- [38] L. Demkowicz and I. Babuska. *p* interpolation error estimates for edge finite elements of variable order in two dimensions. *SIAM journal on numerical analysis*, 41(4):1195–1208, 2003. 48
- [39] L. Demkowicz and A Buffa. H_1 , $H(\text{curl})$ and $H(\text{div})$ -conforming projection-based interpolation in three dimensions: Quasi-optimal *p*-interpolation estimates. *Computer Methods in Applied Mechanics and Engineering*, 194(2):267–296, 2005. 48

- [40] L. Demkowicz and J. Gopalakrishnan. A class of discontinuous Petrov–Galerkin methods. Part I: the transport equation. *Computer Methods in Applied Mechanics and Engineering*, 199(23):1558–1572, 2010. xxxviii, xliv, 1
- [41] L. Demkowicz, J.T. Oden, W. Rachowicz, and O. Hardy. Toward a universal hp adaptive finite element strategy, part 1. Constrained approximation and data structure. *Computer Methods in Applied Mechanics and Engineering*, 77(1):79–112, 1989. 68
- [42] L. Demkowicz, D. Pardo, and W. Rachowicz. 3D hp -adaptive finite element package (3Dhp90). Version 2.0. The Ultimate (?) data structure for three-dimensional, anisotropic hp -refinements. *Ticam Report 02-24*, 2002. xxxviii, xliv, 2, 39, 42
- [43] L. Demkowicz, W. Rachowicz, and Ph. Devloo. A fully automatic hp -adaptivity. *Journal of Scientific Computing*, 17(1-4):117–142, 2002. 39, 48, 49, 68
- [44] A. El maliki, M. Fortin, N. Tardieu, and A. Fortin. Iterative solvers for 3D linear and nonlinear elasticity problems: displacement and mixed formulations. *International Journal for Numerical Methods in Engineering*, 83:1780 – 1802, 2010. 69
- [45] A. Franke, R-U. Börner, and K. Spitzer. Adaptive unstructured grid finite element simulation of two-dimensional magnetotelluric fields for arbitrary surface and seafloor topography. *Geophysical Journal International*, 171(1):71–86, 2007. 6, 35
- [46] R. Ghaedrahmati, A. Moradzadeh, N. Fathianpour, and S.K. Lee. Investigating 2-D MT inversion codes using real field data. *Arabian Journal of Geosciences*, 7(6):2315–2328, 2014. 54
- [47] J.C. Gilbert and C. Lemaréchal. Some numerical experiments with variable-storage quasi-Newton algorithms. *Mathematical programming*, 45(1):407–435, 1989. 61
- [48] A.A. Goldstein. Convex programming in Hilbert space. *Bulletin of the American Mathematical Society*, 70(5):709–710, 1964. 61
- [49] I. Gomez-Revuelto, L.E. Garcia-Castillo, and L.F. Demkowicz. A comparison between PML, infinite elements and an iterative BEM as mesh truncation methods for hp self-adaptive procedures in electromagnetics. *Progress In Electromagnetics Research*, 126, 2012. 22
- [50] I. Gomez-Revuelto, L.E. Garcia-Castillo, S. Llorente-Romano, and D. Pardo. 3D hp -adaptive finite element simulations of bend, step, and magic-T electromagnetic waveguide structures. *Journal of Computational Science*, 5(2):65 – 75, 2014. xxxviii, xliv, 1
- [51] R.W. Groom and R.C. Bailey. Decomposition of magnetotelluric impedance tensors in the presence. *Journal of Geophysical Research*, 94(B2):1913–1925, 1989. 79
- [52] W. Gui and I. Babuska. The h , p and hp versions of the finite element method in 1 dimension. I-III. *Numerische Mathematik*, 49(6):577–683, 1986. xxxviii, xliv, 2, 38, 103

- [53] R.F. Harrington and J.L. Harrington. *Field computation by moment methods*. Oxford University Press, 1996. 9
- [54] R. Hartmann. Multitarget error estimation and adaptivity in aerodynamic flow simulations. *SIAM Journal on Scientific Computing*, 31(1):708–731, 2008. 35
- [55] R. Hartmann and P. Houston. *Goal-oriented a posteriori error estimation for multiple target functionals*. Springer, 2003. 35
- [56] V. Heuveline and R. Rannacher. Duality-based adaptivity in the hp -finite element method. *Journal of Numerical Mathematics jnma*, 11(2):95–113, 2003. 35
- [57] R. Hiptmair. Multigrid method for Maxwell’s equations. *SIAM J. Numer. Anal.*, 36(1):204–225, 1998. 69
- [58] T.J.R. Hughes, J.A. Cottrell, and Y. Bazilevs. Isogeometric analysis: CAD, finite elements, NURBS, exact geometry and mesh refinement. *Computer methods in applied mechanics and engineering*, 194(39):4135–4195, 2005. xxxviii, xlv, 1
- [59] T.J.R. Hughes, A. Reali, and G. Sangalli. Efficient quadrature for nurbs-based isogeometric analysis. *Computer methods in applied mechanics and engineering*, 199(5):301–313, 2010. 40
- [60] R.D. Hyndman and P.M. Shearer. Water in the lower continental crust: modelling magnetotelluric and seismic reflection results. *Geophysical Journal International*, 98(2):343–365, 1989. xxxvii, xliii, 1
- [61] F. Ihlenburg and I. Babuška. Finite element solution of the Helmholtz equation with high wave number Part *i*: the h -version of the FEM. *Computers & Mathematics with Applications*, 30(9):9–37, 1995. 38
- [62] F. Ihlenburg and I. Babuška. Finite element solution of the Helmholtz equation with high wave number Part II: the hp version of the FEM. *SIAM Journal on Numerical Analysis*, 34(1):315–358, 1997. 38
- [63] S. Ji, S. Rondenay, M. Mareschal, and G. Senechal. Obliquity between seismic and electrical anisotropies as a potential indicator of movement sense for ductile shear zones in the upper mantle. *Geology*, 24(11):1033–1036, 1996. 7
- [64] G.R. Jiracek, W.L. Rodi, and L.L. Vanyan. Implications of magnetotelluric modeling for the deep crustal environment in the Rio Grande rift. *Physics of the earth and planetary interiors*, 45(2):179–192, 1987. 53
- [65] S.G. Johnson. Notes on perfectly matched layers (PMLs). *Lecture notes, Massachusetts Institute of Technology, Massachusetts*, 2008. 29
- [66] P. Joly. An elementary introduction to the construction and the analysis of perfectly matched layers for time domain wave propagation. *SeMA Journal*, 57(1):5–48, 2012.

References

- [67] A.G. Jones. Parkinson's pointers' potential perfidy! *Geophysical Journal International*, 87(3):1215–1224, 1986. 11
- [68] A.G. Jones. *Electrical conductivity of the continental lower crust*. Elsevier, 1992. 7
- [69] A.G. Jones, A.D. Chave, G.D. Egbert, D. Auld, and K. Bahr. A comparison of techniques for magnetotelluric response function estimation. 1989. 79
- [70] F.W. Jones and A.T. Price. The perturbations of alternating geomagnetic fields by conductivity anomalies. *Geophysical Journal International*, 20(3):317–334, 1970. 6, 11
- [71] D.L.B. Jupp and K. Vozoff. Stable iterative methods for the inversion of geophysical data. *Geophys. J. R. astr. Soc.*, 42:957–976, 1975. 53
- [72] P.L. Kantek, P.P. Balbi, F.M. Ramos, and H. Fraga de Campos. Electromagnetic induction in three-dimensional structures. In *Inverse Problems in Engineering: Theory and Practice 3rd Int. Conference on Inverse Problems in Engineering*. Port Ludlow, WA, USA, 1999. xxxvii, xliii, 1
- [73] K. Key and C. Weiss. Adaptive finite-element modeling using unstructured grids: the 2D magnetotelluric example. *Geophysics*, 71(6):G291–G299, 2006. xxxix, xlv, 2, 6, 35
- [74] P. Ladevèze. Strict upper error bounds on computed outputs of interest in computational structural mechanics. *Computational Mechanics*, 42(2):271–286, 2008. 43
- [75] J. Ledo. 2-d versus 3-d magnetotelluric data interpretation. *Surveys in Geophysics*, 26(5):511–543, 2005. xl, xlv, 3, 63
- [76] J. Ledo, P. Queralt, A. Martí, and A.G. Jones. Two-dimensional interpretation of three-dimensional magnetotelluric data: an example of limitations and resolution. *Geophysical Journal International*, 150(1):127–139, 2002. 63
- [77] S.K. Lee, H.J. Kim, Y. Song, and C-K. Lee. MT2DInvMatlab—a program in MATLAB and FORTRAN for two-dimensional magnetotelluric inversion. *Computers & Geosciences*, 35(8):1722–1734, 2009. 54
- [78] E.S. Levitin and B.T. Polyak. Constrained minimization methods. *Zhurnal Vychislitel'noi Matematiki i Matematicheskoi Fiziki*, 6(5):787–823, 1966. 56, 61
- [79] D.C. Liu and J. Nocedal. On the limited memory BFGS method for large scale optimization. *Mathematical programming*, 45(1):503–528, 1989. 61
- [80] R.L. Mackie, T.R. Madden, and P.E. Wannamaker. Three-dimensional magnetotelluric modeling using difference equations—Theory and comparisons to integral equation solutions. *Geophysics*, 58(2):215–226, 1993. 6, 35, 53
- [81] R.L. Mackie, J.T. Smith, and T.R. Madden. Three-dimensional electromagnetic modeling using finite difference equations: The magnetotelluric example. *Radio Science*, 29(4):923–935, 1994. 6

- [82] T. Madden and P. Nelson. A defense of Cagniard's magnetotelluric method. *Magnetotelluric methods*, pages 89–102, 1964. 6
- [83] T.M. Madden and R.L. Mackie. Three-dimensional magnetotelluric modelling and inversion. *Proceedings of the IEEE*, 77(2):318–333, 1989. 53
- [84] A. Martí, P. Queralt, A.G. Jones, and J. Ledo. Improving Bahr's invariant parameters using the WAL approach. *Geophysical Journal International*, 163(1):38–41, 2005. 79
- [85] A. Martí, P. Queralt, and J. Ledo. Waldim: A code for the dimensionality analysis of magnetotelluric data using the rotational invariants of the magnetotelluric tensor. *Computers & Geosciences*, 35(12):2295–2303, 2009. xl, xlv, 3, 63
- [86] K.C. Meza-Fajardo and A.S. Papageorgiou. On the stability of a non-convolutional perfectly matched layer for isotropic elastic media. *Soil Dynamics and Earthquake Engineering*, 30(3):68–81, 2010. 29
- [87] M.P. Miensopust. Multidimensional magnetotellurics: A 2D case study and a 3D approach to simultaneously invert for resistivity structure and distortion parameters. *Ph.D. Thesis, Dublin Institute for Advanced Studies*, 2010. 54, 104
- [88] Y. Mitsuhashi and T. Uchida. 3D magnetotelluric modeling using the T- ω finite-element method. *Geophysics*, 69(1):108–119, 2004. 35
- [89] T. Mogi. Three-dimensional modeling of magnetotelluric data using finite element method. *Journal of Applied Geophysics*, 35(2):185–189, 1996. 35
- [90] J.J. Moré and D.J. Thuente. Line search algorithms with guaranteed sufficient decrease. *ACM Transactions on Mathematical Software (TOMS)*, 20(3):286–307, 1994. 56, 63, 77
- [91] J.J. Moré and G. Toraldo. Algorithms for bound constrained quadratic programming problems. *Numerische Mathematik*, 55(4):377–400, 1989. 56, 61
- [92] MUMPS. A multifrontal massively parallel sparse direct solver. <http://graal.ens-lyon.fr/MUMPS/>, 2015. 69
- [93] A.S. Neves. The magnetotelluric method in two dimensional structures. *Ph.D. thesis, Massachusetts Institute of Technology*. 6
- [94] J. Nocedal. Updating quasi-Newton matrices with limited storage. *Mathematics of computation*, 35(151):773–782, 1980. xxxix, xlv, 3, 61
- [95] J. Nocedal and S.J. Wright. *Numerical optimization*. Springer verlag, 1999. 61
- [96] J.T. Oden, L. Demkowicz, W. Rachowicz, and T.A. Westermann. Toward a universal *hp* adaptive finite element strategy, part 2. A posteriori error estimation. *Computer Methods in Applied Mechanics and Engineering*, 77(1):113–180, 1989. 39

- [97] J.T. Oden and Y. Feng. Local and pollution error estimation for finite element approximations of elliptic boundary value problems. *Journal of computational and applied mathematics*, 74(1):245–293, 1996. 38
- [98] J.T. Oden and S. Prudhomme. Goal-oriented error estimation and adaptivity for the finite element method. *Computers & Mathematics with Applications*, 41(5):735–756, 2001. 35, 43
- [99] Y. Ogawa. On two-dimensional modeling of magnetotelluric field data. *Surveys in Geophysics*, 23(2-3):251–273, 2002. 54
- [100] Y. Ogawa and T. Uchida. A two-dimensional magnetotelluric inversion assuming Gaussian static shift. *Geophysical Journal International*, 126(1):69–76, 1996. 54
- [101] X. Ogaya, J. Ledo, P. Queralt, A. Marcuello, and A. Quintà. First geoelectrical image of the subsurface of the hontomín site (Spain) for CO₂ geological storage: A magnetotelluric 2D characterization. *International Journal of Greenhouse Gas Control*, 13:168–179, 2013. xxxvii, xliii, 1, 54
- [102] Weidelt P. Three-dimensional induced polarization and electromagnetic modeling. *Journal of Geophysics*, 41:85–109, 1975. 6
- [103] M. Paraschivoiu and A.T. Patera. A hierarchical duality approach to bounds for the outputs of partial differential equations. *Computer Methods in Applied Mechanics and Engineering*, 158(3):389–407, 1998. 35
- [104] D. Pardo. Integration of *hp*-adaptivity with a two grid solver: applications to electromagnetics. *Ph.D. Thesis, The University of Texas at Austin*, 2004. 43
- [105] D. Pardo. Multigoal-oriented adaptivity for *hp*-finite element methods. *Procedia Computer Science*, 1(1):1953–1961, 2010. xxxviii, xlv, 2, 35, 47
- [106] D. Pardo, V.M. Calo, C. Torres-Verdin, and M.J. Nam. Fourier series expansion in a non-orthogonal system of coordinates for the simulation of 3D-DC borehole resistivity measurements. *Computer Methods in Applied Mechanics and Engineering*, 197(21):1906–1925, 2008. 23, 103
- [107] D. Pardo and L. Demkowicz. Integration of *hp*-adaptivity with a two grid solver for elliptic problems. *Computer Methods in Applied Mechanics and Engineering*, 195:674–710, 2006. 69
- [108] D. Pardo, L. Demkowicz, and J. Gopalakrishnan. Integration of *hp*-adaptivity and a two grid solver for electromagnetic problems. *Computer Methods in Applied Mechanics and Engineering*, 195:2533–2573, 2006. 69
- [109] D. Pardo, L. Demkowicz, C. Torres-Verdín, and M. Paszynski. Two-dimensional high-accuracy simulation of resistivity log ging-while-drilling (lwd) measurements using a self-adaptive goal-oriented *hp* finite element method. *SIAM Journal on Applied Mathematics*, 66(6):2085–2106, 2006. 43

- [110] D. Pardo, L. Demkowicz, C. Torres-Verdin, and M. Paszynski. A self-adaptive goal-oriented *hp*-finite element method with electromagnetic applications. Part II: electrodynamics. *Computer methods in Applied Mechanics and Engineering*, 196(37):3585–3597, 2007. 34, 43, 48, 54
- [111] D. Pardo, L. Demkowicz, C. Torres-Verdín, and L. Tabarovsky. A goal-oriented *hp*-adaptive finite element method with electromagnetic applications. Part I: electrostatics. *International Journal for Numerical Methods in Engineering*, 65(8):1269–1309, 2006. 34, 54
- [112] D. Pardo, M. Paszynski, N. Collier, J. Alvarez, L. Dalcin, and V.M. Calo. A survey on direct solvers for Galerkin methods. *SeMA Journal*, 57(1):107–134, 2012. 69
- [113] D. Pardo, C. Torres-Verdín, M.J. Nam, M. Paszynski, and V.M. Calo. Fourier series expansion in a non-orthogonal system of coordinates for the simulation of 3D alternating current borehole resistivity measurements. *Computer Methods in Applied Mechanics and Engineering*, 197(45):3836–3849, 2008. 23, 24
- [114] W.D. Parkinson. Directions of rapid geomagnetic fluctuations. *Geophysical Journal International*, 2(1):1–14, 1959. 11
- [115] W.D. Parkinson. The influence of continents and oceans on geomagnetic variations. *Geophysical Journal of the Royal Astronomical Society*, 6(4):441–449, 1962. 11
- [116] J. Pedersen and J.F. Hermance. Least squares inversion of one-dimensional magnetotelluric data: an assessment of procedures employed by Brown University. *Surveys in Geophysics*, 8(2):187–231, 1986. 13
- [117] A.T. Price. The theory of magnetotelluric methods when the source field is considered. *Journal of Geophysical Research*, 67(5):1907–1918, 1962. 6
- [118] A.T. Price. The theory of geomagnetic induction. *Physics of the Earth and Planetary Interiors*, 7(3):227–233, 1973. 18
- [119] S. Prudhomme and J.T. Oden. On goal-oriented error estimation for elliptic problems: application to the control of pointwise errors. *Computer Methods in Applied Mechanics and Engineering*, 176(1):313–331, 1999. 35, 43, 57
- [120] W. Rachowicz, D. Pardo, and L. Demkowicz. Fully automatic *hp*-adaptivity in three dimensions. *Computer Methods in Applied Mechanics and Engineering*, 195(37):4816–4842, 2006. 48
- [121] A.P. Raiche. An integral equation approach to three-dimensional modelling. *Geophysical Journal International*, 36(2):363–376, 1974. 6
- [122] R. Rannacher and F-T. Suttmeier. A posteriori error control in finite element methods via duality techniques: Application to perfect plasticity. *Computational mechanics*, 21(2):123–133, 1998. 35

References

- [123] A.M. Rivera-Rios. Multi-order vector finite element modeling of 3D magnetotelluric data including complex geometry and anisotropy. 2014. xxxix, xlv, 2
- [124] W.L. Rodi. Regularization and Backus-Gilbert estimation in nonlinear inverse problems: Application to magnetotellurics and surface waves. 53
- [125] M. Rubinat, J. Ledo, E. Roca, O. Rosell, and P. Queralt. Magnetotelluric characterization of a salt diapir: a case study on Bicornb–Quesa Diapir (Prebetic Zone, SE Spain). *Journal of the Geological Society*, 167(1):145–153, 2010. 5
- [126] Y. Sasaki. Three-dimensional inversion of static-shifted magnetotelluric data. *Earth, planets and space*, 56(2):239–248, 2004. 54
- [127] D. Schillinger, S.J. Hossain, and T.J.R. Hughes. Reduced Bézier element quadrature rules for quadratic and cubic splines in isogeometric analysis. *Computer Methods in Applied Mechanics and Engineering*, 277:1–45, 2014. xxxviii, xlv, 1
- [128] U. Schmucker. Regional induction studies: a review of methods and results. *Physics of the Earth and Planetary Interiors*, 7(3):365–378, 1973. 11
- [129] Ch. Schwab. *p- and hp-finite element methods: Theory and applications in solid and fluid mechanics*. Clarendon Press Oxford, 1998. 38, 39
- [130] F. Simpson and K. Bahr. *Practical magnetotellurics*. Cambridge University Press, 2005. xxvii, xxxvii, xliii, 1, 11, 15, 17
- [131] W. Siripunvaraporn. Three-dimensional magnetotelluric inversion: an introductory guide for developers and users. *Surveys in geophysics*, 33(1):5–27, 2012. 54
- [132] W. Siripunvaraporn and G. Egbert. An efficient data-subspace inversion method for 2D magnetotelluric data. *Geophysics*, 65(3):791–803, 2000. 54
- [133] W. Siripunvaraporn and G. Egbert. Data space conjugate gradient inversion for 2D magnetotelluric data. *Geophysical Journal International*, 170(3):986–994, 2007. 54
- [134] W. Siripunvaraporn, G. Egbert, Y. Lenbury, and M. Uyeshima. Three-dimensional magnetotelluric inversion: data-space method. *Physics of the Earth and Planetary Interiors*, 150(1):3–14, 2005. 6, 54
- [135] J.T. Smith. Conservative modeling of 3-D electromagnetic fields, Part I: properties and error analysis. *Geophysics*, 61(5):1308–1318, 1996. 35
- [136] J.T. Smith. Conservative modeling of 3-D electromagnetic fields, Part II: biconjugate gradient solution and an accelerator. *Geophysics*, 61(5):1319–1324, 1996. 35
- [137] J.T. Smith and J.R. Booker. Magnetotelluric inversion for minimum structure. *Geophysics*, 53:1565–1576, 1988. 53

- [138] J.T. Smith and J.R. Booker. Rapid inversion of two-and three-dimensional magnetotelluric data. *Journal of Geophysical Research: Solid Earth (1978–2012)*, 96(B3):3905–3922, 1991. 53
- [139] P. Šolin and L. Demkowicz. Goal-oriented *hp*-adaptivity for elliptic problems. *Computer Methods in Applied Mechanics and Engineering*, 193(6):449–468, 2004. 43
- [140] P. Solin, L. Dubcova, J. Cervený, and I. Doležel. Adaptive *hp*-FEM with arbitrary-level hanging nodes for Maxwell’s equations. *Adv. Appl. Math. Mech*, 2(4):518–532, 2010. 35
- [141] L. Solymar, D. Walsh, and R.R.A. Syms. *Electrical properties of materials*. Oxford University Press, 2014. 7
- [142] J.E. Spratt, A.G. Jones, V.A. Jackson, L. Collins, and A. Avdeeva. Lithospheric geometry of the Wopmay orogen from a Slave craton to Bear Province magnetotelluric transect. *Journal of Geophysical Research: Solid Earth (1978–2012)*, 114(B1), 2009. 79
- [143] S.P. Srivastava. Method of interpretation of magnetotelluric data when source field is considered. *Journal of Geophysical Research*, 70(4):945–954, 1965. 6
- [144] C.M. Swift Jr. A magnetotelluric investigation of an electrical electrical conductivity anomaly in the southwestern united states. *Ph.D. Thesis, Massachusetts Institute of Technology*. 6
- [145] B.A. Szabo and I. Babuška. *Finite element analysis*. John Wiley & Sons, 1991. 40, 65
- [146] A. Szymczak, A. Paszyńska, M. Paszyński, and D. Pardo. Preventing deadlock during anisotropic 2D mesh adaptation in *hp*-adaptive FEM. *Journal of Computational Science*, 4(3):170–179, 2013. xxxviii, xliv, 1
- [147] A. Tarantola. Inverse problems theory. *Methods for Data Fitting and Model Parameter Estimation*. Elsevier, Southampton, 1987. 53
- [148] F.L. Teixeira and W.C. Chew. PML-FDTD in cylindrical and spherical grids. *Microwave and Guided Wave Letters, IEEE*, 7(9):285–287, 1997. 22
- [149] F.L. Teixeira and W.C. Chew. Analytical derivation of a conformal perfectly matched absorber for electromagnetic waves. *Microwave and Optical technology letters*, 17(4):231–236, 1998. 19, 22, 29
- [150] A.N. Tikhonov. On determining electrical characteristics of the deep layers of the earth’s crust. In *Sov. Math. Dokl*, volume 2, pages 295–297, 1950. xxxvii, xliii, 1, 6
- [151] A.N. Tikhonov and M.N. Berdichevsky. Experience in the use of magnetotelluric methods to study the geological structures of sedimentary basins. *Izv. Earth Phys.*, (2):34–41, 1966. 6

References

- [152] S.C. Ting and G.W. Hohmann. Integral equation modeling of three-dimensional magnetotelluric response. *Geophysics*, 46(2):182–197, 1981. 6
- [153] K.G. van der Zee, E.H. van Brummelen, and R. De Borst. Goal-oriented error estimation for stokes flow interacting with a flexible channel. *International journal for numerical methods in fluids*, 56(8):1551–1557, 2008. 43
- [154] K. Vozoff. The magnetotelluric method in the exploration of sedimentary basins. *Geophysics*, 37(1):98–141, 1972. 5, 17
- [155] K. Vozoff. *The magnetotelluric method*, in Nabighian, M. N. *Electromagnetic methods in applied geophysics*, volume 2. SEG Books, 1988. 5
- [156] K. Vozoff. Magnetotellurics: Principles and practice. *Journal of Earth System Science*, 99(4):441–471, 1990. 5
- [157] K. Vozoff. Electromagnetic methods in applied geophysics. 1991. 17, 102
- [158] J.R. Wait. On the relation between telluric currents and the earth's magnetic field. *Geophysics*, 19(2):281–289, 1954. 6, 13
- [159] P.E. Wannamaker. Advances in three-dimensional magnetotelluric modeling using integral equations. *Geophysics*, 56(11):1716–1728, 1991. 6
- [160] P.E. Wannamaker, G.W. Hohmann, and W.A. SanFilipo. Electromagnetic modeling of three-dimensional bodies in layered earths using integral equations. *Geophysics*, 49(1):60–74, 1984. 6
- [161] P.E. Wannamaker, J.A. Stodt, and L. Rijo. A stable finite element solution for two-dimensional magnetotelluric modelling. *Geophysical Journal International*, 88(1):277–296, 1987. xxxix, xlv, 2, 6
- [162] A.J. Ward and J.B. Pendry. Calculating photonic Green's functions using a nonorthogonal finite-difference time-domain method. *Physical Review B*, 58(11):7252, 1998. 25, 27
- [163] S.H. Ward and G.W. Hohmann. *Electromagnetic theory for geophysical applications*, in Nabighian, M. N. *Electromagnetic methods in applied geophysics*, volume 4. SEG Books, 1988. 10
- [164] J.T. Weaver. *Mathematical methods for geo-electromagnetic induction*, volume 7. Research Studie, 1994. xxxvii, xliii, 1, 10, 36
- [165] J.T. Weaver, A.K. Agarwal, and F.E.M. Lilley. Characterization of the magnetotelluric tensor in terms of its invariants. *Geophysical Journal International*, 141(2):321–336, 2000. xl, xlv, 3, 63
- [166] H. Wiese. Geomagnetische tiefentellurik teil II: die streichrichtung der untergrundstrukturen des elektrischen widerstandes, erschlossen aus geomagnetischen variationen. *Geofisica pura e applicata*, 52(1):83–103, 1962. 11

- [167] R. William and R.L. Mackie. Nonlinear conjugate gradients algorithm for 2D magnetotelluric inversion. *Geophysics*, 66(1):174–187, 2001. 53, 54
- [168] F.T. Wu. The inverse problem of magnetotelluric sounding. *Geophysics*, 33:972–979, 1968. 53
- [169] M.S. Zhdanov and E. Tartaras. Three-dimensional inversion of multitransmitter electromagnetic data based on the localized quasi-linear approximation. *Geophysical Journal International*, 148(3):506–519, 2002. 6
- [170] C. Zhu, R.H. Byrd, P. Lu, and J. Nocedal. Algorithm 778: L-BFGS-B: Fortran subroutines for large-scale bound-constrained optimization. *ACM Transactions on Mathematical Software (TOMS)*, 23(4):550–560, 1997. xxxix, xlv, 3, 61, 62, 74
- [171] J. Zitelli, I. Muga, L. Demkowicz, J. Gopalakrishnan, D. Pardo, and V.M. Calo. A class of discontinuous Petrov–Galerkin methods. part IV: the optimal test norm and time-harmonic wave propagation in 1D. *Journal of Computational Physics*, 230(7):2406–2432, 2011. xxxviii, xlv, 1